

UCSF

UC San Francisco Electronic Theses and Dissertations

Title

Morphology state space dynamics and functional divergence in isogenic populations

Permalink

<https://escholarship.org/uc/item/5cj7d783>

Author

Chang, Amy

Publication Date

2017

Peer reviewed|Thesis/dissertation

Morphology state space dynamics and functional divergence
in isogenic populations

by

Amy Y. Chang

DISSERTATION

Submitted in partial satisfaction of the requirements for the degree of

DOCTOR OF PHILOSOPHY

in

Biophysics

in the

GRADUATE DIVISION

of the

UNIVERSITY OF CALIFORNIA, SAN FRANCISCO

This thesis is dedicated to those who have taught me, guided me, and most importantly, believed in me.
Thank you.

ACKNOWLEDGMENTS

I would like to thank my graduate advisor, Wallace Marshall, for being the best advisor a graduate student could hope for. He has been endlessly kind, supportive, and encouraging through the ups and downs of my PhD and the value of having someone like that on your side throughout graduate school is immeasurable. Thank you.

To members of the Marshall Lab, both past and present – thank you for creating a welcoming environment each and every day. Thank you for being patient with me and training me throughout the years, shaping me into a more thoughtful and inquisitive scientist.

I would like to thank members of my thesis committee, Sophie Dumont and Valerie Weaver for their support, encouragement, and guidance over the years. They encouraged me through the difficult times and never ceased to offer their support of my ambitions, both professionally and personally. Thank you.

I would also like to thank members of my graduate program, particularly Matt Jacobson, Tanja Kortemme, Julia Molla, Rebecca Brown, and Nicole Flowers for seeing me through from matriculation to graduation and for constantly striving to improve the program with both our personal and professional development in mind.

At UCSF, I'd like to thank Barbara Panning and members of the Panning lab, in particular Karen Leung; Davide Ruggero and members of the Ruggero Lab, in particular Morgan Truitt, Mary McMahon, and Adrian Contreras; Adam Olshen and Ritu Roy; Steve Chen, Sarah Elmes, DeLaine Larsen, and Kurt Thorn for sharing your reagents and scientific expertise with me and being generous with your time. None of this work would have been possible without your kindness and generosity.

I'd like to thank my undergraduate mentor, Ahmet Yildiz, who trusted me, encouraged me, and believed in me in the very early days of my scientific career. Without Ahmet, I would not be a scientist today, so for that I can only say thank you.

To one of my best friends in graduate school, Kyle Barlow, thank you for the lunchtime pep talks, the caffeine runs, and the many misadventures. Above all, thank you for being kind, thoughtful, and patient and for showing me how to be a better person. Graduate school would have been a very different experience without you.

To Anita Verma, my long-running roommate, you were the best Craigslist find ever. Thank you for being so damn cool and educating me about all things art history. Thank you for introducing me to The Great British Bake-Off and chachi pants, and for sharing your parathas with me. You made me an infinitely cooler, better, and kinder person and I am so thankful to have shared our time at UCSF together.

To my UCSF classmates and friends, both past and current, thank you for being my colleagues and friends over the years. Whenever anyone asks me what my favorite thing is about UCSF, I always say it's the people, and I couldn't have asked for a better group of people than the one I found here.

To my dog, Bumper, thank you for the emotional support and for the snuggles and kisses when things in graduate school weren't going so well.

Lastly, I'd like to thank my parents and my brother for the kindness and care you have shown me throughout my life, and for the support and encouragement you've given me through the difficult times, both in life and in graduate school. Thank you.

ABSTRACT

The phenotypic behavior of a cell is driven by its molecular microstate, which emerges as a function of its epigenetic, transcriptomic, and proteomic states. Variability in these states can arise due to stochastic processes, leading to extensive microstate and functional variability in genetically clonal populations. It is of fundamental interest in cell biology to understand the number of states a cell can occupy, as well as the laws governing state transitions and the functional correlates of state variability. In this work, we develop an ensemble of molecular biology, computational, and statistical tools to measure and quantify morphological heterogeneity in both fixed and live populations of isogenic wild-type (WT) mouse embryonic fibroblasts (MEFs). We discover that WT MEFs occupy a continuum of states in morphology space, with increased density in specific subspaces and that this increased occupancy is due to a non-uniform energy landscape underlying WT MEF morphology space. Finally, we show that drug induction can induce topological changes to the energy landscape and that these changes correspond directly to functional divergence at the cellular level.

This work produces new insight into the topological and dynamical properties of morphological heterogeneity and provides a body of evidence suggesting that variability in these parameters correlate directly to functional heterogeneity within an isogenic population. Furthermore, this work positions morphological heterogeneity as an important and consequential form of non-genetic heterogeneity, setting the groundwork for future studies of the relationships between microstate, morphological, and functional variability.

TABLE OF CONTENTS

Chapter 1. Introduction	1
Chapter 2. Morphological Heterogeneity in Genetically Clonal Populations	
2a. Fluorescent Labeling and Imaging of Cytomorphological Structures	9
2b. Developing Quantitative Feature Analysis Algorithms	12
2c. Principal Component Analysis for Dimensionality Reduction	15
2d. Results and Interpretation	19
Chapter 3. Developing a Dynamic Map of Morphology Space	
3a. Constructing a Live-Cell Reporter for Cytomorphology	22
3b. Time-Lapse Imaging of Live Cells	30
3c. Dynamics of Cellular Transitions in Morphology Space	31
3d. Boltzmann Statistics and Energy Landscapes	36
3e. Results and Interpretation	39
Chapter 4. Relationships Between Morphological and Functional Heterogeneity	
4a. Heterogeneous Response to Apoptosis Induction	41
4b. Time-Lapse Imaging of Live Cell Response to Camptothecin	42
4c. Changing Dynamics of Morphology Space in Response to Camptothecin	43
4d. Camptothecin Creates Local State Space Attractors	50
4e. Results and Interpretation	56
Chapter 5. Conclusion and Future Directions	58
References	63
Appendix	65

LIST OF TABLES

Table 1. Dominant loadings of the first three Principal Components of fixed WT MEFs	18
Table 2. Plasmids and PCR conditions for Gibson Assembly of 3Reporter lentivirus plasmid	26
Table 3. Primer sequences for PCR amplification of 3Reporter lentivirus plasmid components	27
Table 4. Primer sequences to confirm 3Reporter lentivirus plasmid sequence	27
Table A1. Dominant loadings of the first three Principal Components of live WT MEFs	66
Table A2. Complete loadings of the first three Principal Components of live WT MEFs	67
Table A3. Complete loadings of the first three Principal Components of fixed WT MEFs	71

LIST OF FIGURES

Figure 1. Fibroblasts derived from control and bipolar disorder patients	7
Figure 2. Fluorescent images of fixed WT MEFs	9
Figure 3. Example fluorescence image of a fixed WT MEF	12
Figure 4. Sample segmentation of cytomorphological structures	14
Figure 5. Probability density functions of the first three Principal Components of WT MEFs	19
Figure 6. Scatter plots depicting WT MEF state occupancy in 2-dimensional morphology spaces	20
Figure 7. Scatter plots depicting WT MEF state occupancy in a 3-dimensional morphology space	20
Figure 8. Schematic of 3-Reporter gene-reporter cassette	23
Figure 9. Schematic of Gibson Assembly of 3Reporter lentivirus expression plasmid	27
Figure 10. Example fluorescence image of a live WT MEF	30
Figure 11. Plot of raw WT MEF transition vectors	31
Figure 12. Plot of bin-by-bin average WT MEF transition vectors	32
Figure 13. Colored surface plot of bin-by-bin average WT MEF transition magnitudes	33
Figure 14. Plot of mean morphology space states and transition vectors of single WT MEF cells	34
Figure 15. Probability plots of WT MEF density functions and transition dynamics	36
Figure 16. Plot of the effective energy landscape of WT MEF morphology space	39
Figure 17. Non-uniform apoptotic response in WT MEFs in response to camptothecin induction	42
Figure 18. Example fluorescence images of WT MEFs under camptothecin induction	43
Figure 19. Plots of raw Apoptosis[+]/[-] transition vectors	44
Figure 20. Plots of bin-by-bin average Apoptosis[+]/[-] transition vectors	45
Figure 21. Plots of mean morphology space states and transition vectors of Apoptosis[+]/[-] cells	45
Figure 22. Probability plots of Apoptosis[+]/[-] density functions and transition dynamics	47
Figure 23. Example two-sample Kolmogorov-Smirnov significance test	48
Figure 24. Camptothecin produces significant changes in transition probability plots	49

Figure 25. Camptothecin induction decreases the average transition vector magnitude of WT MEFs	50
Figure 26. Statistic values for Kolmogorov-Smirnov tests of camptothecin-treated cells	51
Figure 27. Plot of the effective energy landscape of camptothecin WT MEF morphology space	52
Figure 28. Plot of the differential between camptothecin and untreated energy landscapes	54
Figure 29. Plot of the differential between Apoptosis[+] and untreated energy landscapes	54
Figure 30. Plot of the differential between Apoptosis[-] and untreated energy landscapes	54
Figure 31. Heat map of apoptosis probability as a function of morphology space state	56
Figure A1. Sequence of 3Reporter Cassette	74
Figure A2. Cell segmentation algorithm	77
Figure A3: Cell morphometry feature extraction algorithm	86
Figure A4: Cell textural feature extraction algorithm	90
Figure A5: Nucleus morphometric feature extraction algorithm	92
Figure A6: Nucleus textural feature extraction algorithm	97
Figure A7: Mitochondria morphometric and textural feature extraction algorithm	99

CHAPTER 1. Introduction

A cell is the most basic unit of living organisms, capable of exhibiting a range of fascinating behaviors and characteristics that, together, one would identify as “life.” The ability to carry out these behaviors is encoded in a cell’s genome, or DNA sequence, which acts as a blueprint for cellular activities. DNA codes for a multitude of functions that we associate with life – for example, the F-ATPase that generates energy to power human metabolism, or the photoreceptors in our eyes that absorb wavelength-specific photons and allow us to see the world around us. It is estimated that there may be more than 1 trillion diverse species in the world (Locey and Lennon, 2016), and it is the difference between their genomes that gives each species its unique structure and behavior, allowing sperm whales to hold their breaths for more than an hour, honeybees to hone in on UV-emitting flowers in their search for nectar, and giant sequoias to grow hundreds of feet tall and withstand forest fires. DNA is, without a doubt, the most important influencer of cellular behavior, so one might be surprised to learn that organisms containing the exact same DNA sequence, base pair for base pair, can be found to exhibit non-uniform behaviors.

The discovery of behavioral variability in genetically clonal populations, termed non-genetic heterogeneity, fundamentally shifted understanding of cell biology from that of a deterministic process where all structure and behavior is dictated by the genome, to one in which biology is a less well-dictated process, in part deterministic and in part stochastic. Stochastic processes are those driven by random and unpredictable events. As example, proteins are the most common and essential functional unit of the cell and for a functional protein to be produced, a gene must be transcribed into mRNA and then translated into a protein. This process requires the complex coordination of hundreds of molecular components, the majority of which are freely floating in the nucleoplasm and cytoplasm and whose interactions are driven by electrostatic interactions at the atomic scale. In this particular case, for a gene to be transcribed, DNA must first be unwound, and the correct transcription factor must bind to the promoter site of the correct gene. Helper molecules must then bind to this site and recruit RNA polymerase, which then must ratchet

along several hundred base pairs of DNA while recruiting the correct complementary nucleotide and forming chemical bonds to produce a complete mRNA transcript. This mRNA must then undergo a number of potential modifications, from removal of introns by a multi-part molecular machine called the spliceosome, to biochemical modifications of the 3' and/or 5' UTRs. The post-transcriptionally modified mRNA must then be bound by nuclear export receptors, shuttled to the nuclear membrane, and transported through a nuclear pore into the cytoplasm. Here the mRNA must be fortuitously bound by a ribosome, which must then progressively ratchet along the mRNA while incorporating the codon-appropriate amino acid at every third base. Once the amino acid polymer is complete, the polypeptide then needs to fold into the correct functional conformation; for a relatively small protein such as thyroid releasing hormone, which composed of 234 amino acids, the possible conformation space can contain up to 3^{466} ($\sim 10^{222}$) possibilities, using the assumption of 3 possible angles for each of the Ψ and Φ angles of a peptide bond (Levinthal, 1969). This sequence of events illustrates just a small subset of the hundreds, if not thousands, of interactions that must occur for a gene to be transcribed and subsequently translated into a protein. Given the complexity of this process and the number of steps driven by random electrostatic interactions, it is not difficult to understand how two cells with identical underlying genomes may come to possess different numbers of the same protein. Multiply this by the number of different proteins within the cell, and one can imagine the vast space of possible protein microstates and how this could feasibly lead to variability in cellular behavior. Furthermore, molecular microstates are composed of more than just proteins, as there can also be variability along other parameters, such as non-coding RNAs or higher-order assembly processes at the organelle and cellular scale. The ability of biological organisms to adopt many different molecular microstates despite an identical underlying genetic code dramatically increases the functional capacity of biological organisms and results in a diversification of possible behaviors.

Though stochasticity is often considered a “messy” process and defies the perception of biology as a perfectly orchestrated collection of moving parts, stochasticity in fact plays an important and vital role in many biological processes. In 1944, Joseph Bigger discovered that genetically clonal populations of *Staphylococcus pyogenes* exhibited non-uniform resistance to antibiotics (Bigger, 1944). Under

penicillin inoculation, about 1% of the cells in a genetically clonal population proved resistant; when this surviving population was expanded, it was found that a second inoculation of penicillin again resulted in a 1% survival rate. If the initial surviving population had undergone mutations that rendered them antibiotic-resistant, one would expect the second re-established population to exhibit a 100% survival rate. These observations led to a hypothesis that these cells were not antibiotic-resistant mutants, but instead phenotypic variants of a genetically clonal population. These cells were termed “persister” cells and recent studies in *Escherichia coli* have shown that though a population may be genetically clonal, the “persister” cells within the population express functionally distinctive characteristics, including suppressed metabolic activity and unique gene expression profiles (Shah et al., 2006). One might surmise that the tradeoff for drug resistance is a delay in growth rate and that the tradeoff for more robust growth is increased sensitivity to antibiotic exposure. In this case, the stochasticity that produces phenotypic variants of a genetically clonal population leads to an evolutionary advantage at the population level, where different cells are primed to excel under different conditions, with one group slow-growing, but able to survive antibiotic exposure, and a second group more evolutionarily “fit” in that cells rapidly divides and produce progeny, but simultaneously experiences increased vulnerability to changes in the external environment.

Another illustration of the important role stochastic processes play in biology can be found in the process of mammalian haematopoietic differentiation. Haematopoietic stem cells in the bone marrow respond to external cues and differentiation factors to give rise to all the major blood types, including erythroids (e.g. red blood cells), lymphocytes (e.g. T-cells, B-cells), and myelocytes (e.g. macrophages). The mechanics of this process can be challenging to overcome, as a pool of genetically clonal cells must give rise to an assortment of cell types, but must also respond heterogeneously to external cues to achieve an incomplete response at the population level such that the stem cell population is not uniformly depleted. To gain a better understanding of how this process works, scientists measured the expression levels of the stem cell transcript Sca-1 across a population of mouse haematopoietic progenitor cells and found that Sca-1 expression levels followed an approximately normal distribution (Chang et al., 2008).

Interestingly, cells varied in their probability of differentiation based on their Sca-1 expression levels. When a population of clonal haematopoietic stem cells were induced with the erythroid-producing differentiation factor erythropoietin, the differentiation potential of cells was found to be inversely correlated with their Sca-1 expression levels, with cells expressing low levels of Sca-1 exhibiting a seven-fold higher differentiation potential than those expressing high levels of Sca-1. In contrast, differentiation into the myeloid lineage in response to granulocyte-macrophage colony-stimulating factor (GM-CSF) was positively correlated with Sca-1 expression levels, with Sca-1- high cells exhibiting a two-fold higher differentiation potential compared to low Sca-1 expressing cells. At first glance, stochastically-driven processes may seem inefficient when compared with deterministically-driven processes; however, depending on the context, stochastic processes may engender several key advantages. First, it allows for many cell types to be produced from a single common precursor pool, eliminating the burdensome task of maintaining separate precursor pools for each possible lineage. Secondly, because this single precursor pool is pluripotent, in theory the ratios of different cell types can be quickly altered in response to the needs of the organism; for example, an acute demand for increased production of erythrocytes may be quickly met through conversion of cells into a pro-erythrocyte lineage, leaving an intact pool of self-replenishing stem cells. This is a potentially easier task than maintaining separate pools, monitoring their stem cell levels, and selectively replenishing specific pools. These experiments convincingly illustrate that stochasticity plays a vital role in many biological processes and can often enable an organism to more rapidly and efficiently respond to changing physiological needs.

Stochasticity is the driving force behind microstate variability in genetically clonal populations and a central interest in biology is to understand the ex-genome functional diversity that microstates engender. This necessitates developing a fuller understanding of what microstates can exist, the rules that govern microstate transitions, and the functional correlates of each microstate. However, given the many hundreds of thousands of molecules in a cell, a comprehensive determination of the molecular microstate is difficult to come by. Genome-wide techniques such as transcriptomics, proteomics, or ChIP-Seq, succeed at capturing various parameters of the molecular microstate, but while powerful, these methods

are inherently cell-destructive and cannot be used to study state transitions or the functional correlates of the molecular microstate. Here we explore whether cytomorphology may serve as a viable intermediate solution. While lacking the precision of genome-wide methods, cytomorphology represents the sum of many hundreds of molecular processes and may thus serve as a coarse-grain indicator of the molecular state of a cell.

Cytomorphology is essentially composed of mesoscale structures built from hundreds of nanometer-scale molecular interactions. As example, mitochondria are complex, multi-layered structures composed of an outer membrane, an inner membrane, an intermembrane space, and a matrix space within the inner membrane. Membranes are composed of a combination of phospholipids and proteins, and diverse proteins are responsible for carrying out a range of important mitochondrial functions – for example, the F-ATPase that converts a proton gradient into chemical energy in the form of ATP, or the numerous caspase proteins that play an integral role in apoptosis, a process of cell-programmed death. At the mesoscale, mitochondria exist as a combination of fragmented mitochondria, which are isolated bean-shaped pieces, and fused mitochondria, which are large, interconnected branching networks. Fragmented and fused mitochondria are known to exhibit different biochemical properties and play different roles within the cell. Mitochondrial fusion is a necessary process for maintaining the physiological health of the cell; by fusing, mitochondria can exchange metabolites, enzymes, and mitochondrial DNA (mtDNA), essentially creating a shared reservoir of accessible materials. This process is so vital that if mitochondrial fusion is chemically inhibited, mitochondria exhibit a loss of membrane potential (Chen et al., 2003) and a decrease in rates of aerobic respiration (Chen et al., 2005).

Beyond mitochondrial morphometry, differences in spatial localization have also been found to correlate with biochemical and functional differences. In a 2002 study of hepatocytes, authors found that, compared to perinuclear mitochondria, peripheral mitochondria were more fragmented, exhibited higher $\Delta\psi$ (membrane potential), and had higher uptake rates of positively-charged molecules (Collins et al., 2002). Spatial localization has also proven consequential in terms of the establishment of interorganelle contacts. Sites of mitochondria-ER contact have been found at the site of fission events (Friedman et al.,

2011), suggesting that mitochondrial fission events can be directly influenced by mitochondrial contacts with other organelles, who themselves may be subject to specific subcellular localization constraints.

At the cellular level, changes in mitochondrial morphology have been linked to dramatic changes in cellular function. In *S. cerevisiae*, mitochondrial morphology has been shown to correlate with the respiratory state of the cell, where actively respiring cells largely form interconnected networks of mitochondria, while mitochondria in non-respiring, fermentative cells primarily exist in a more fragmented form (Aung-Htut et al., 2013). In mammalian cells, sets of proteins have been identified as key players in the fusion and fission processes. In several studies, authors found that, upon upregulation of fusion proteins or downregulation of fission proteins, mitochondria preferentially formed hyperfused networks, with the resultant cells exhibiting decreased sensitivity to apoptotic induction. In the inverse case, authors found that upregulation of fission proteins or downregulation of fusion proteins resulted in mitochondrial hyperfragmentation, producing cells with increased apoptotic sensitivity (Alirol and Martinou, 2006). The ensemble of these observations highlight the integral role that mitochondrial fusion and fission events play in the functional behavior of a cell.

Further highlighting the relationship between mitochondrial morphology and cellular function, many disease states have been associated with aberrant mitochondrial morphologies. These include neurological disorders such as Alzheimer's (Wang et al., 2009; Trimmer et al., 2000), Parkinson's (Wiemerslage et al., 2016; Trimmer et al., 2000) and mood disorders (Cataldo et al., 2010). An example of the observed changes is found in (Fig. 1), which illustrates mitochondrial organization in a healthy control patient (left) compared to that of a patient diagnosed with bipolar disorder (BD), where the mitochondria have become more densely clustered and perinuclearly organized.

Here we have presented an in-depth examination of mitochondria, from its molecular constituents to the biochemical and functional properties of its different morphological states. Using this example we provide supporting evidence for the hypothesis that organelle morphology may serve as a mesoscale indicator of the cellular microstate and, consequently, the functional state of a cell. In theory, these principles may be widely applicable to many additional organelles beyond mitochondria (e.g. the nucleus,

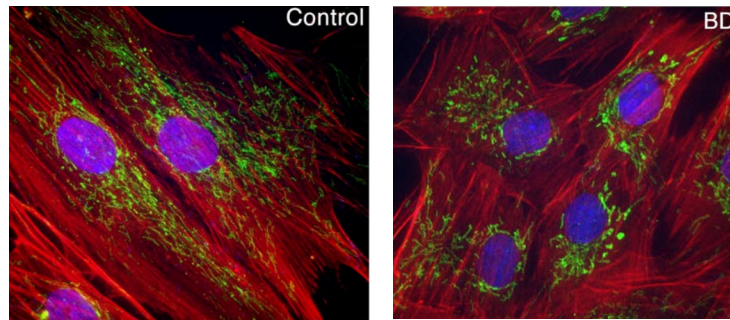


Figure 1. Fibroblasts derived from control and bipolar disorder patients. The actin cytoskeleton appears in red, the cell nucleus appears in blue, and the mitochondria appear in green. Mitochondria shape, organization, and spatial localization are altered in the bipolar disorder (right) versus control (left) patient. (Source: Cataldo et al., 2010)

endoplasmic reticulum, Golgi complex, etc.). Given the strong possibility of organelle morphology serving as an indicator of cellular state and function, we endeavoured to develop tools for quantifying organelle morphology and characterizing morphological heterogeneity within a cellular population. In particular, we investigate morphological heterogeneity against an isogenic background; if identified and proven to have functional correlates, this would constitute a new form of non-genetic heterogeneity and fundamentally advance our understanding of cell biology.

CHAPTER 2. Morphological Heterogeneity in Genetically Clonal Populations

One of the most challenging aspects of studying the functional correlates of cytomorphology arises from the fact that the majority of known cytomorphological changes originate from changes at the genome level. This makes it difficult to untangle the consequences of cytomorphological changes from those produced by genome-driven molecular changes. As example, Huntington's Disease (HD) is a disease characterized by gradual loss of motor coordination and difficulties with cognition and mood regulation (Walker, 2007). HD is caused by a mutation in the Huntingtin (Htt) gene and has been associated with changes in both mitochondrial morphology and biochemical function at the cellular scale (Tabrizi et al., 1999; Wang et al., 2009). However, Htt has not been directly implicated in mitochondrial dynamics and may very likely contribute to HD progression through additional pathways, making it difficult to untangle the functional effects of morphological changes from parallel molecular changes produced by the Htt mutant.

Because of these limitations, a useful context in which to study cytomorphological variability is in isogenic populations, where all cells share a genetically identical background. This allows one to ensure that any variability in cytomorphology or cellular function is not driven by genetically-driven molecular changes, but instead arises from non-genetic heterogeneity. Many of the most commonly used laboratory cell lines appear largely morphologically uniform; however, wild-type (WT) mouse embryonic fibroblasts (MEFs) exhibit high degrees of native morphological heterogeneity (Fig. 2). This observation, coupled with the fact that MEFs are a commonly used laboratory cell line with a diverse set of molecular and genetic tools available, render MEFs an ideal model system for our study. MEFs are mesenchyme-derived primary cells that play important roles in the formation and support of the extracellular matrix. The fact that morphological heterogeneity is observed against a WT background allows us to study this heterogeneity in as "native" a state as possible, given the constraints of working in an *in vitro* tissue culture setting. This allows us to better understand native morphological heterogeneity and its relationship to cellular function and offers the possibility of illuminating the workings of biological systems in their

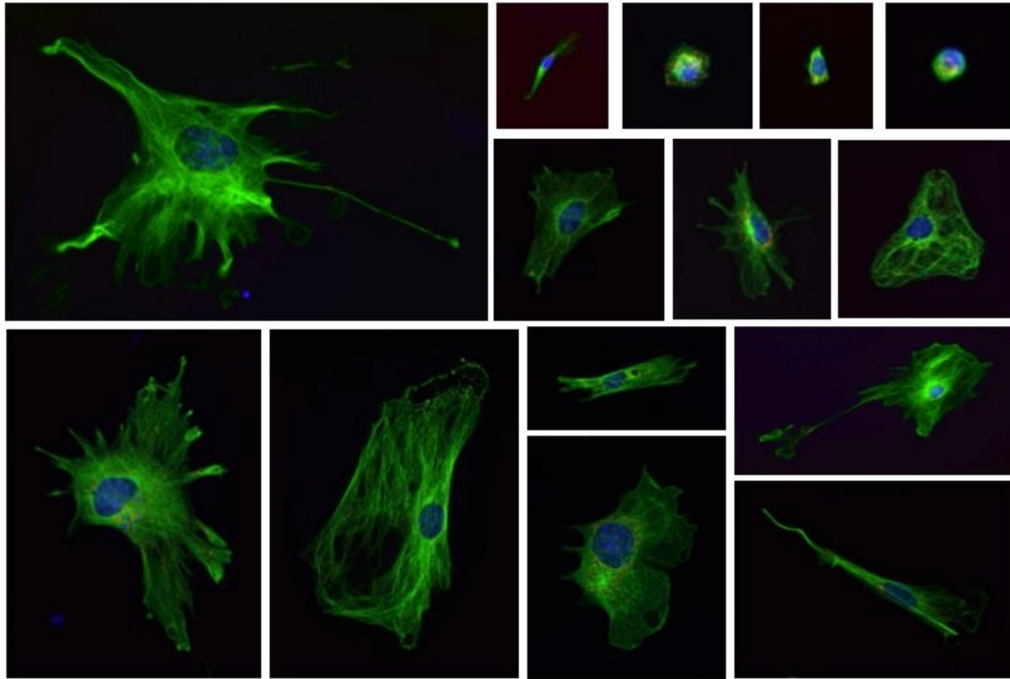


Figure 2. Fluorescent images of fixed WT MEFs. The microtubule cytoskeleton appears in green and the cell nucleus appears in blue. Images taken at 40x magnification. Images are rescaled in a consistent manner such that cell sizes are directly comparable.

most native form, absent any laboratory-induced genetic modifications.

Our approach for studying morphological heterogeneity and its functional correlates begins with developing tools to label and visualize cytomorphological structures. We then must quantify morphological features of these structures and develop ways to interpret these feature measurements in a meaningful and statistically rigorous manner. We discuss the development of these techniques in the following sections.

2a. Fluorescent Labeling and Imaging of Cytomorphological Structures

WT MEFs were harvested from 13.5 days post-fertilization embryos of C57BL/6 mice (Jackson Laboratory, 000664), with embryo torsos isolated and diced with a sterile razor blade, then plated into 10cm cell culture dishes under full cell culture media (Dulbecco's Modified Eagle Serum w/ 4.5 g/L glucose (DME H-21) + 10% fetal bovine serum (FBS) + 1x penicillin/streptomycin (P/S)). Cells were incubated at 37°C, 5% CO₂ for 24h. Non-adherent cells were aspirated and adherent cells, representing

the MEF population, were trypsinized (0.25% trypsin w/EDTA) and stored in 10% DMSO in FBS at -80°C until ready for use.

We chose the microtubule cytoskeleton, the nucleus, and the mitochondria as our cytomorphological structures of interest. These structures were chosen based on numerous examples of changes in these structures occurring concomitantly with changes in cellular function. Cytoskeletal changes are a hallmark of cancer and have been linked to changes in cellular adhesion and growth rates (Chen et al., 2014; Vilariño et al., 2006). Nuclear morphology has similarly been linked to variability in cellular function, as aberrations to nuclear morphology are a hallmark of cancer and used widely as diagnostic markers for dysplasia and carcinoma. Nuclear morphology has also been observed to change as a function of aging, with nuclei transitioning from a smooth, bean-shaped structure to a rippled, multi-lobed structure. This effect is particularly noticeable in disorders of premature aging, such as progeria (Scaffidi et al., 2005). Changes in mitochondrial morphology have been associated with changes at both the biochemical level and the pathophysiological level; mitochondrial changes have been observed in parallel with changes to the electrochemical membrane potential, ATP production (Iannetti et al., 2015), and apoptotic sensitivity (Alirol and Martinou, 2006; Suen et al., 2008), as well as many neurodegenerative disorders including Alzheimer's, Parkinson's, and Huntington's Disease (Tabrizi et al., 1999; Wang et al., 2009).

To visualize and quantify these morphological structures, we began by biochemically labeling these structures with fluorescent antibodies and dyes. Passage 1 (P1) WT MEFs were plated into 384-well tissue culture plates (Greiner, #781091) at a density of 50 cells/well under full cell culture media (DME H-21 + 10% FBS + 1x P/S). Cells were incubated at 37°C, 5% CO₂ for 24h and chemically fixed and labeled according to the following protocol:

- 1) Fix cells by incubating under 4% paraformaldehyde (Electron Microscopy Sciences, #15710) in phosphate-buffered saline (PBS) for 15 minutes at room temp.
- 2) Wash 1x with PBS.
- 3) Permeabilize cells by incubating under 0.1% Triton X-100 in PBS for 15 minutes at room

- temp.
- 4) Wash 1x with PBS.
 - 5) Block cells with 3% BSA+ 5% normal goat serum (Jackson ImmunoResearch Labs, #005-000-121) + 0.1% Triton X-100 in PBS (“MEF Blocking Buffer”) for 10 minutes at room temp.
 - 6) Incubate cells in 400x dilution mouse mAb mtHsp70 (1.08 mg/mL, ThermoFisher, MA3-028) in “MEF Blocking Buffer” for 1 hour at room temp.
 - 7) Wash 1x with PBS.
 - 8) Incubate cells in 1000x dilution goat anti-mouse IgG AlexaFluor488 (2 mg/mL, Life Technologies, A11029) in “MEF Blocking Buffer” for 1 hour at room temp.
 - 9) Wash 1x with PBS.
 - 10) Incubate cells in 600x dilution rabbit pAb α -tubulin (0.2 mg/mL, abcam, ab18251) in “MEF Blocking Buffer” for 1 hour at room temp.
 - 11) Wash 1x with PBS.
 - 12) Incubate cells in 1000x dilution goat anti-rabbit IgG AlexaFluor647 (2 mg/mL, Life Technologies, A21245) in “MEF Blocking Buffer” for 1 hour at room temp.
 - 13) Wash 1x with PBS.
 - 14) Incubate cells in 1 μ g/mL DAPI (Invitrogen, D1306) in 0.1% Triton X-100 in PBS for 10 minutes at room temp.
 - 15) Wash 3x with PBS. Store cells at 4°C under PBS, protected from light, for up to 3 days.

Following fluorescent labeling, cells were imaged at 40x magnification on the InCell 2000, an automated high-content imaging platform. A sample cell image is shown in (Fig. 3). At 40x magnification, it took 49 fields of view (FOVs) to scan each well of a 384-well plate. Each FOV was imaged in three fluorescent channels: Cy5 to illuminate AlexaFluor647-labeled α -tubulin (microtubule cytoskeleton), DAPI to illuminate DAPI-labeled DNA (nucleus), and FITC to illuminate AlexaFluor488-labeled mtHsp70 (mitochondria). Channels were then overlaid and a composite image of the well compiled by concatenating the 49 FOVs into a 7x7 array for each well.

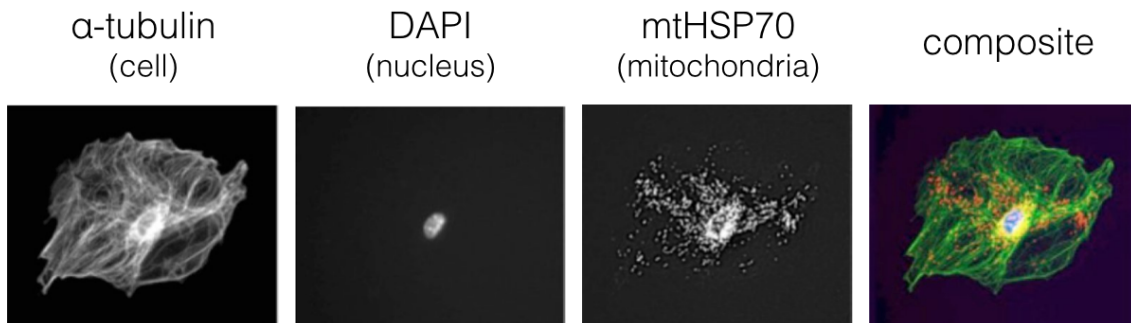


Figure 3. Example fluorescence image of a fixed WT MEF. A single cell labeled for α -tubulin (cell), DAPI (nucleus), and mitochondrial heat shock protein 70 (mitochondria). Each structure was labeled with a different, spectrally separate, fluorophore and a composite image is shown on the right, with the microtubule cytoskeleton of the cell depicted in green, the nucleus depicted in blue, and the mitochondria depicted in red. Image taken at 40x magnification.

2b. Developing Quantitative Feature Analysis Algorithms

After imaging each well, we computationally segmented each cell to digitally isolate objects for further analysis. To accomplish this, we wrote custom segmentation algorithms based on a series of dilation, filling, erosion, and smoothing steps (Appendix, pg. 77-85) and segmented objects on the microtubule cytoskeleton channel (Cy5). Cells were presented to the user and manually accepted or rejected based on a few criteria: i) cells had to be single, isolated cells that were not in contact with other cells or the edge of the well, and ii) cells could not be in active M phase, as discerned from a user-based assessment of cytomorphology.

Once cells were segmented, they were further processed to extract cytoskeletal, nuclear, and mitochondrial features using custom feature extraction algorithms written in MATLAB. The microtubule cytoskeleton and nucleus are single, continuous objects and were analyzed for similar feature sets. These features include basic morphometric measurements such as area, perimeter, and ellipticity, as well as more complex features such as the area of a convex hull surrounding the object or the percent change to an object's area or perimeter upon application of varying degrees of smoothing to the object outline (Appendix, pg. 86-89, 92-96). A second set of feature algorithms focused on textural and spatial intensity features. These included explicit textural features such as contrast and homogeneity, as well as custom spatial distribution features that analyzed intensity distributions within different regions of the object (Appendix, pg. 90-91, 97-98). These measurements provided information about the spatial distribution

and organization of elements within the cell, allowing us to ask, for example, if α -tubulin was more densely concentrated towards the center or periphery of the cell, and if α -tubulin was evenly distributed throughout the cytoplasm or clustered into discrete subspaces.

Unlike the cell and nucleus, mitochondria are not single objects and require a multi-object feature analysis approach. Mitochondria consist of a collection of interconnected networks of tubules (fused mitochondria) and an array of isolated, bean-shaped mitochondria (fragmented mitochondria). To properly segment mitochondria, we developed a second set of custom segmentation algorithms. These similarly employed a series of dilation, filling, erosion, and smoothing steps (Appendix, pg. 99-105), relying on the user for manual endpoint acceptance or rejection. Mitochondrial features were analyzed using a second set of custom features extraction algorithms written in MATLAB, this time customized specifically for the multi-object properties of mitochondria. As with the cell and nucleus, these consisted of measurements of size, shape, and texture features, but now with the possibility of including mean, maximum, minimum, and standard deviation measurements given the multi-object nature of the structure. For morphometric measurements, we quantified basic features such as the number of mitochondria, sum and mean area, and sum and mean perimeter, as well as more complex features such as the ratio of fused to fragmented mitochondria or the mean number of nodes per mitochondrial network (Appendix, pg. 99-105). For textural measurements, we again measured explicit textural features such as contrast and homogeneity in order to assess the textural distribution of mitochondria within the cell. We also developed features to measure spatial intensity distributions within specific subspaces of the cell (Appendix, pg. 99-105). For example, we sliced the cell into four concentric rings of increasing radii and took measurements such as the percentage of total mitochondria contained within each ring, or the variance of mitochondrial area within each ring. This allowed us to probe aspects of mitochondrial subcellular localization, such as whether mitochondria preferentially occupy perinuclear or peripheral subspaces, or if variability in mitochondria morphology varied as a function of subcellular localization.

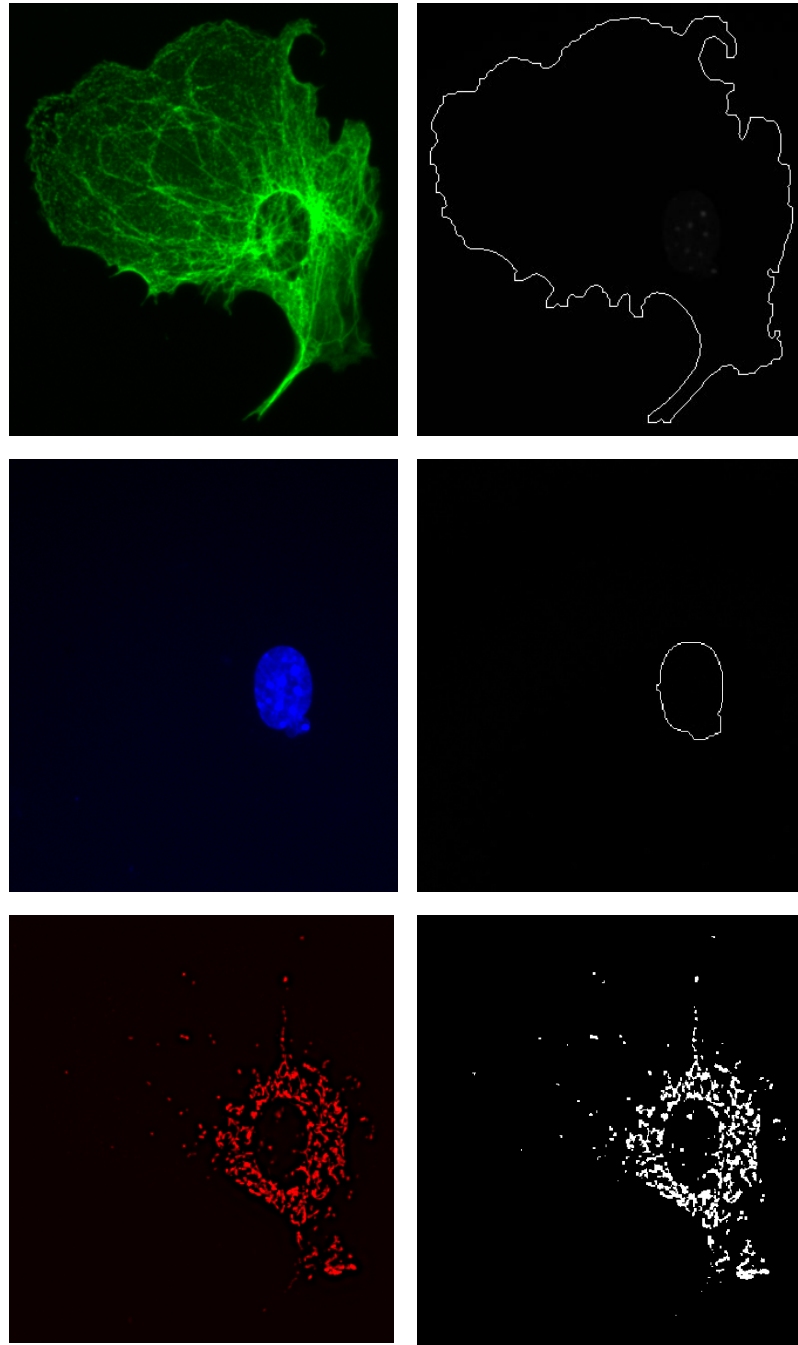


Figure 4. Sample segmentation of cytomorphological structures. An example cell labeled for α -tubulin (cell), DAPI (nucleus), and mitochondrial heat shock protein 70 (mitochondria) segmented for each structure using custom image segmentation algorithms written in MATLAB. The original image (left, colored) and segmented outline/mask (right, white) are shown for an example cell labeled for the microtubule cytoskeleton (top, green), nucleus (middle, blue), and mitochondria (bottom, red). Image taken at 40x magnification.

2c. Principal Component Analysis for Dimensionality Reduction

Extracting a high-dimensional feature set is powerful in that it provides an expansive set of feature information about each cell. However, a challenge in working with high-dimensional datasets is in parsing which variables are informative and which are either redundant or information-poor. Several statistical tools exist for dimensionality reduction. In our case, we chose to employ a technique called Principal Component Analysis (PCA), based on the following reasons:

- i) PCA works on the principle of identifying features that contribute maximal variance to the population. Since our primary interest is in identifying morphological heterogeneity, identifying high-variance features is a reasonable way to identify this heterogeneity. Variance is, of course, not the only measure of heterogeneity and there exist other dimensionality-reduction techniques (e.g. hierarchical clustering, t-SNE) to identify heterogeneity; however, in this case the relatively simple method of PCA proved sufficient for identifying underlying morphological heterogeneity in a population of WT MEFs.
- ii) The final output of PCA is a set of linear combinations of the original features, weighted by their variance. This is useful because by producing an output phrased in terms of the original input morphological features, the results remain interpretable from a biological standpoint. This is in contrast to many machine learning classifiers (e.g. neural nets, random forests), which may succeed in classifying cells, but often occludes information concerning the classification process, rendering it difficult to parse the contribution of each feature.
- iii) The results of PCA can be graphically represented in Cartesian coordinates, providing a useful and intuitive way to visualize morphology space as well as morphological transitions within this space. This visualization is also amenable to visualization of probability densities and energy landscapes within morphology space, a process we touch upon further in Chapter 3.
- iv) The output of PCA is a set of linear combinations, so distance between Principal Component (PC) coordinates scale linearly and can be meaningfully compared.

Principal Component Analysis: Theory

Mathematically, PCA works by taking an M-variable feature set over N samples and organizing the data into an MxN matrix, X. The goals of PCA are two-fold: a) to identify sets of orthogonal linear combinations of features that contribute the most overall variance to the population, and b) to reduce redundant features, i.e. features whose values correlate strongly with each other. To achieve this, we undertake the following set of linear algebra operations:

1) Compute the covariance matrix of MxN, producing an MxM size matrix of covariance values, where n is the number of samples.

$$S_X = \text{cov}(X) = \frac{1}{n-1} XX^T \quad (\text{Eq. 1})$$

Since we are interested in *minimizing* the amount of redundancy, or covariance, our goal in this case is to make all off-diagonal values equal to 0. In other words, we want to diagonalize the matrix.

2) We identify an operation, P, that can be applied to X such that Y=PX. The covariance of Y is then:

$$S_Y = \text{cov}(Y) = \frac{1}{n-1} (PX)(PX)^T \quad (\text{Eq. 2})$$

$$S_Y = \frac{1}{n-1} (PXX^T P^T) \quad (\text{Eq. 3})$$

$$S_Y = \frac{1}{n-1} PAP^T \quad \text{where } A = XX^T \quad (\text{Eq. 4})$$

3) A is a symmetric matrix equal to XX^T and can be diagonalized by the matrix E, a matrix of the eigenvectors of A, where each column is a different eigenvector.

$$S_Y = \frac{1}{n-1} PEDE^T P^T \quad (\text{Eq. 5})$$

4) If we choose $E = P^T$, then

$$S_Y = \frac{1}{n-1} PP^T DE^T E \quad (\text{Eq. 6})$$

$$S_Y = \frac{1}{n-1} D \quad (\text{Eq. 7})$$

This series of operations effectively diagonalizes S_Y . By calculating the eigenvectors of the symmetric matrix A, where $A = XX^T$, we can diagonalize S_Y and minimize the covariance, one of the primary aims of PCA. By selecting the eigenvectors with the largest eigenvalues, we are able to identify the most

dominant, or “important” PCs that contribute the most “stretch” to the basis. These can be used to calculate a % explained, the percent of total population variance captured by that particular PC.

Principal Component Analysis: Application

Since PCA works by identifying features contributing maximal variance to the population, it is important that features be normalized to have the same mean and range. Feature value ranges will naturally vary depending on the feature being measured; a measurement such as cell area may vary from 10-1000 pixels, whereas a measurement like eccentricity is confined to the values 0.0 – 1.0. To avoid biasing our PCA analysis towards these larger-magnitude features, we normalized the mean and range of all features. This is accomplished by calculating the μ (mean) and σ (std) of each feature and calculating the associated z-score of each measurement.

$$z = \frac{x - \mu_x}{\sigma} \quad (\text{Eq. 8})$$

Once the z-scores have been calculated for all measurements, we can proceed to PCA. In our case, this computation is as follows, where $z_{(i,j)}$ = the z-value for the i^{th} feature of the j^{th} cell.

$$Z = \begin{bmatrix} z_{(1,1)} & z_{(1,2)} & \dots & z_{(1,903)} & z_{(1,904)} & z_{(2,1)} & z_{(2,2)} & \dots & z_{(204,1)} & z_{(205,1)} \\ z_{(2,1)} & z_{(2,2)} & \dots & z_{(2,903)} & z_{(2,904)} & z_{(1,2)} & z_{(2,2)} & \dots & z_{(204,2)} & z_{(205,2)} \\ \dots & \dots \\ z_{(204,1)} & z_{(204,2)} & \dots & z_{(204,903)} & z_{(204,904)} & z_{(1,903)} & z_{(2,903)} & \dots & z_{(204,903)} & z_{(205,903)} \\ z_{(205,1)} & z_{(205,2)} & \dots & z_{(205,903)} & z_{(205,904)} & z_{(1,904)} & z_{(2,904)} & \dots & z_{(204,904)} & z_{(205,904)} \end{bmatrix}$$

$$S_Z = \text{cov}(Z) = \frac{1}{904-1} ZZ^T \quad (\text{Eq. 9})$$

We can eliminate the fraction in front of ZZ^T , since this is essentially a weighting factor and we are only interested in the eigenvectors and relative weighting of each eigenvector relative to the others, values that are not influenced by this weighting factor. We then calculate the eigenvectors of ZZ^T and associated eigenvalues. The values for the three eigenvectors with the largest eigenvalues, representing Principal Components (PC) 1, 2, and 3, are listed in (Table 1), while histograms of the values of PC1, PC2, and PC3 are shown in (Fig. 5).

Principal Component 1; variance explained = 29.6%

Feature Name	Feature Type	Loading
CellEquivDiameterArea	Cell morphometry	0.1185
NucEquivDiameterArea	Nucleus morphometry	0.1173
NucMeanCentroidDist	Nucleus morphometry	0.1166
CellMeanCentroidDist	Cell morphometry	0.1151
NucMinorAxisLength	Nucleus morphometry	0.1145
NucConvexPerimeter	Nucleus morphometry	0.1143
NucHighSmoothPerimeter	Nucleus morphometry	0.1140
CellConvexPerimeter	Cell morphometry	0.1133
CellHighSmoothPerimeter	Cell morphometry	0.1132
NucLowSmoothPerimeter	Nucleus morphometry	0.1130

Principal Component 2; variance explained = 10.6%

Feature Name	Feature Type	Loading
CellCVDisc3	Cell texture	-0.1558
CellCVDisc4	Cell texture	-0.1528
CellCVDisc2	Cell texture	-0.1526
CellCVDisc1	Cell texture	-0.1397
CellFracTotalDisc1	Cell texture	-0.1393
CellCVCentroidDist	Cell texture	-0.1318
CellHighSmoothOrig... ...PerimeterChangeRel	Cell morphometry	0.1223
CellHighSmoothOrig... ...PerimeterRatio	Cell morphometry	0.1223
CellCircularity	Cell morphometry	0.1216
CellSolidity	Cell morphometry	0.1191

Principal Component 3; variance explained = 6.7%

Feature Name	Feature Type	Loading
MitoCVDisc2	Mitochondria texture	0.1725
MitoCVDisc3	Mitochondria texture	0.1716
MitoCVDisc4	Mitochondria texture	0.1698
CellCVCorrelation	Cell texture	0.1573
CellCVCentroidDist	Cell morphometry	0.1546
CellCircularity	Cell morphometry	-0.1464
MitoVarCorrelation	Mitochondria texture	0.1436
CellVarCorrelation	Cell texture	0.1433
MitoCVCorrelation	Mitochondria texture	0.1358
CellVarHomogeneity	Cell texture	0.1344

Table 1. Dominant loadings of the first three Principal Components of fixed WT MEFs. The top 10 loadings of the first three principal components of a 205-feature set analysis of WT MEF morphology. Principal Component 1 captures 29.6% of total variance and is dominated by cell and nucleus morphometric features. Principal Component 2 captures 10.6% of total variance and is dominated by cell morphometric and textural features. Principal Component 3 captures 6.7% of total variance and is dominated by mitochondrial textural and cell morphometric features.

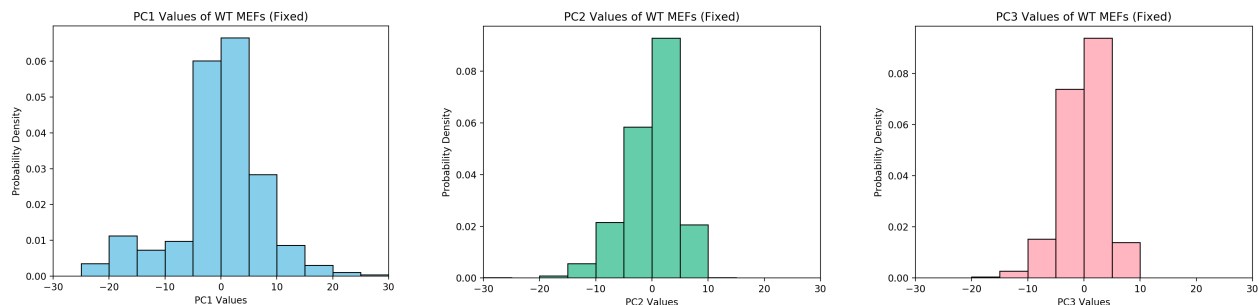


Figure 5. Probability density functions of the first three Principal Components of WT MEFs. Plots of the probability density functions of PC1, PC2, and PC3 show the extent of variance along these three dimensions. PC1 is the most variable dimension but is still characterized by a single dominant peak centered at 0 and does not show evidence of bimodality or more complicated types of heterogeneity. PC2 and PC3 are similarly characterized by single dominant peaks centered at 0, but explore a more constrained range of values relative to PC1.

2d. Results and Interpretation

By identifying the eigenvectors with the largest corresponding eigenvalues, we can identify the linear combination of features that most successfully captures overall population variance. The top 3 PCs and their top 10 loadings are listed in (Table 1). A complete list of loadings of the top three PCs can be found in (Appendix, Table A2). From these loadings, it becomes clear that the dominant contributors to morphological heterogeneity are cell morphometry and textural features, nuclear morphometry features, and mitochondrial textural features.

By plotting Principal Components 1, 2, and 3 against each other (Fig. 6, Fig. 7), we were able to visualize the morphology space of WT MEFs, observing several interesting characteristics. First, these plots confirmed the existence of morphological heterogeneity in WT MEFs and proved that our feature analysis algorithms could successfully capture facets of this heterogeneity. Furthermore, our approach allowed us to visualize the topology of WT MEF morphology space and discover that cells do not cluster into discrete subspaces, suggesting that WT MEF morphologies are more aptly described as a continuum rather than a set of discrete states. This means that instead of occupying or cycling through a discrete set of morphological states, cells in a population of WT MEFs can instead occupy many hundreds of different morphological states at any given point in time.

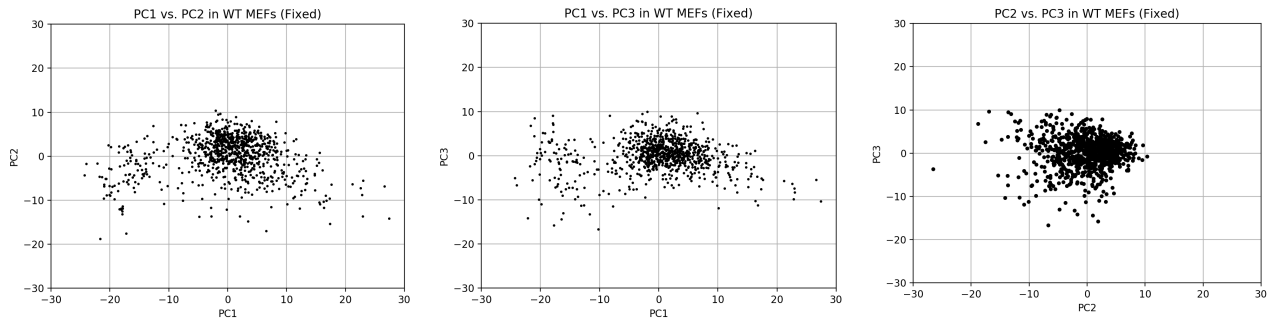


Figure 6. Scatter plots depicting WT MEF state occupancy in 2-dimensional morphology spaces. Morphology space distribution of fixed WT MEFs in three different 2-dimensional spaces defined by permutations of PC1, PC2, and PC3. Cell states appear heterogeneously distributed in the space defined by PC1 vs. PC2, with a dense cloud of cells near (0, 0) and less dense occupancy towards the periphery of this space. Cell states appear similarly heterogeneous in the space defined by PC1 vs. PC3, with a dense cloud near (0, 0) and more sparse occupancy towards the periphery. Cells display more constrained morphological heterogeneity in the space defined by PC2 vs. PC3, with a single dense cloud near (0, 0) and a few scattered cells extending towards the periphery. This observation is in agreement with the principles of Principal Component Analysis, where higher PCs capture a larger fraction of the total variance.

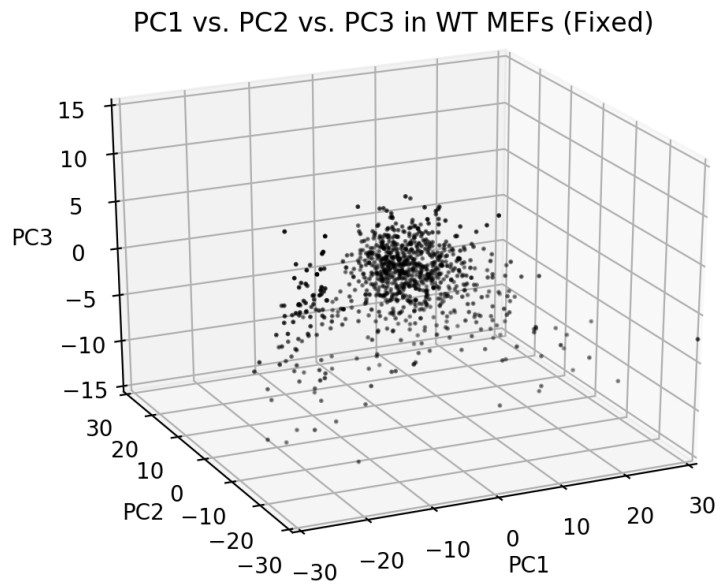


Figure 7. Scatter plots depicting WT MEF state occupancy in a 3-dimensional morphology space. Morphology space distribution of fixed WT MEFs in a 3-dimensional morphology space defined by PC1 vs. PC2 vs. PC3. This plots allows us to visualize the heterogeneity of WT MEF morphology space. There is a single dense cloud of cells near (0, 0, 0) in morphology space and a significant cloud of more sparsely distributed cells extending in all directions along PC1, PC2, and PC3. The full range of PC1 and PC2 [-30, 30] appears to be occupied, whereas cells appear to predominantly occupy the lower half of PC3 [-30, 0]. This plot confirms that the coupling of our 205-feature morphology analysis algorithms with Principal Component Analysis can capture aspects of the observed morphological heterogeneity of WT MEFs.

These observations lead to many interesting questions about the dynamics as well as functional consequences of morphological heterogeneity. In terms of dynamics, one could ask whether morphology state is a static or dynamic property. If dynamic, what are the rules that govern morphological transitions? Do cells traverse morphology space in a deterministic manner (e.g. state A always leads to state B, which always leads to state C, etc.), or are transitions probabilistically driven (e.g. state A has an x% chance of leading to state B and a y% chance of leading to state C.) Are the probabilities of transition uniform in all regions of morphology space, or are transition dynamics variable across state space? By developing a clearer understanding of the dynamics of morphology space, we hope to gain insight into the driving principles behind morphological heterogeneity as well as contribute more generally to our understanding of the dynamical properties of cells.

Along with an improved understanding of the dynamics of morphology space, we hope to address questions regarding the functional relevance of a cell's morphological state. There are many known instances of morphological changes arising concomitantly with functional changes, both in basic science and clinical settings. The observed morphological heterogeneity thus necessarily leads to questions of whether this morphological state might correlate with functional behavior and, if so, if morphology can be used as a coarse-grain indicator of the functional state of a cell.

CHAPTER 3. Developing a Dynamic Map of Morphology Space

Our first step in developing a dynamic map of morphology space was to develop molecular biology tools to enable tracking of morphology in live cells. Once accomplished, we imaged cells over a multi-day time course and plotted their trajectories in morphology space as a function of time. This approach allowed us to gain insight into the dynamics underlying the observed morphological heterogeneity of WT MEFs. Furthermore, we were able to adapt statistical mechanical concepts to morphology space and develop a theoretical map of the energy landscape underpinning this space, creating, to our knowledge, the first known energy landscape of cellular morphology space.

3a. Constructing a Live-Cell Reporter for Cytomorphology

Our first step in mapping out the dynamics of morphology space focused on developing molecular biology tools to visualize and track cytomorphology in live WT MEFs. We decided to approach this challenge by engineering a lentivirus construct. Lentivirus-mediated delivery of fluorescent reporters was ideal for several reasons: a) common transfection approaches such as liposomal transfection or electroporation tend to produce low transfection efficiency in primary cell lines such as WT MEFs; in contrast, lentivirus produce much higher transduction efficiencies; b) since the time course was expected to run over several days, we wanted a way to integrate the expression system into the endogenous WT MEF genome to ensure robust expression over the entire time course, rather than risk transient expression expiring over the course of the experiment. Selection of a stable cell line over several weeks was not a viable option, given that WT MEFs are a primary cell line and experience increased senescence potential with each passage.

The general approach for engineering our lentivirus, which we call the 3-Reporter lentivirus, centered on cloning fluorescent reporters of our three structures of interest into the lentivirus expression vector pPWPXL (Addgene #12257). Our three gene-reporter constructs were: mIFP-H2B (monomeric infrared fluorescent protein attached to Histone 2B) to target the nucleus, tdTomato-mito-7 (tandem dimer Tomato attached to a mitochondria localization sequence) to target the mitochondria, and EGFP-tubulin

(enhanced green fluorescent protein attached to α -tubulin) to target the microtubule cytoskeleton. The three reporters were separated by two copies of the self-cleaving peptide P2A (Kim et al., 2011). The target 3Reporter gene cassette is depicted in (Fig. 8). This approach greatly simplified construction of the lentivirus plasmid in that it allowed us to express all three gene-reporter constructs under the same EF1 α promoter. Furthermore, this strategy ensured expression of the three gene-reporter constructs in stoichiometrically consistent ratios, allowing us to more reasonably compare fluorescence intensities across channels. Full sequence data for the “3-Reporter” insert can be found in (Appendix, Fig. A1).

1) Fluorescent reporter plasmids were acquired from the Nikon Imaging Center (NIC) at UCSF, originally provided by Michael Davidson (FSU) as part of the Davidson Collection. The plasmids acquired were: EGFP-tubulin-6 (EGFP-tagged α -tubulin, fluorescent in the GFP channel), mIFP-H2B-6 (mIFP-tagged histone 2B, fluorescent in the Cy5 channel), and tdTomato-mito-7 (tdTomato-tagged mitochondria localization sequencing, fluorescent in the RFP channel). We transformed plasmids into DH5 α competent cells (ThermoFisher, #18265017) and grew colonies on appropriate antibiotic selection lysogeny broth (LB) agar plates. Surviving colonies were then cultured in a solution of LB + antibiotic to OD₆₀₀ ~ 3.0. Plasmids were purified and isolated the plasmids using a QIAprep Spin Miniprep Kit (Qiagen, #27105) and sent to a third-party sequencing service (Elim Biopharmaceuticals, Inc.) for



Figure 8. Schematic of 3-Reporter gene-reporter cassette. Fluorescent reporters targeted to our three structures of interest are transcribed as a single transcript under an EF1 α promoter. The nucleus-targeting monomeric infrared fluorescent protein attached to histone 2B is found at the beginning of the transcript, followed by the self-cleaving peptide P2A. This is followed by the mitochondria-targeting tdTomato attached to a mitochondria localization sequence (tdTomato-mito-7), followed by another copy of the self-cleaving peptide P2A. The transcript terminates with the microtubule cytoskeleton-targeting enhanced green fluorescent protein attached to α -tubulin (EGFP-tubulin-6). Once transcribed and translated, the P2A sequences will self-cleave, producing three separate fluorescent reporters in a stoichiometric 1:1:1 ratio targeting our three structures of interest.

sequence confirmation. We then separately transfected each plasmid into cultures of 293T cells, using the FuGENE 6 Transfection Reagent (Promega, E2691) and accompanying protocol. FuGENE 6 and DNA were mixed at a ratio of 6 μ L FuGENE : 1 μ g DNA. At 72h post-transfection, cells were examined under an epifluorescence microscope to confirm fluorescence and proper cytostructural localization of our gene-reporter products.

2) The three fluorescent reporters were stitched together and copies of the self-cleaving P2A inserted in between reporters to create one comprehensive 3-Reporter cassette. The self-cleaving P2A peptide allows for the entire insert to be transcribed and translated as a single unit, ensuring that each gene-reporter trio is produced in a stoichiometrically consistent ratio. Since some of the feature measurements rely on pixel intensity measurements, this approach allows us to reasonably compare fluorescence intensities across different channels in a consistent manner. Once completed, this cassette was inserted into the pWPXL backbone. Cloning of the cassette was accomplished using a Gibson Assembly approach and cassette insertion accomplished using restriction enzyme cloning. All primers were purchased from Integrated DNA Technologies (IDT) and primer sequences are listed in (Table 3). The strategies for cassette assembly and insertion were as follows:

- i) pWPXL homology was added to the 5' end of mIFP-H2B-6 using the F-H2B_KOZAK primer; this primer preserves the BamHI restriction site and introduces a Kozak sequence to maximize expression efficiency.
- ii) The full P2A sequence (66 base pairs, Kim et al., 2011) was added to the 3' end of mIFP-H2B-6 using the R-mIFP_EXTENSION primer to form the intermediate "mIFP-H2B-6-P2A."
- iii) The tdTomato-mito-7 construct was separated into tdTomato1 and tdTomato2 modules. It was necessary to split the construct and polymerase chain reaction (PCR) amplify the two modules separately because the tandem tdTomato modules are homologous, resulting in random primer attachment to both modules if PCR amplified as a single module. P2A homology was added to the 5' end of tdTomato1 using the F-MITO primer. Tandem linker homology was maintained at the 3' end of tdTomato1 using the R-tdTomatoLinker primer. Tandem linker homology was

maintained at the 5' end of tdTomato2 using the F-tdTomatoLinker primer. P2A-EGFP-tubulin-6 homology was added to the 3' end of tdTomato2 using the R-MITO primer.

iv) The P2A sequence (66 base pairs, Kim et al., 2011) was added to the 5' end of EGFP-tubulin-6 using the F-EGFP_EXTENSION primer to form the intermediate “P2A-EGFP-tubulin-6.”

v) pWPXL homology was added to the 3' end of EGFP-tubulin-6 using the R-TUBULIN primer.

3) Primers were designed to introduce 16-42 base pair homology between fragments such that they would be compatible with Gibson Assembly (GA). Fragments were PCR amplified using Phusion High-Fidelity DNA Polymerase (NEB, M0530L), following a standard PCR protocol. Amplification conditions are listed in (Table 2). Fragments were stitched together using a Gibson Assembly Kit (NEB E2611S) and accompanying protocol. PCR and Gibson Assembly steps were accomplished in the following order:

i) PCR amplify mIFP-H2B-6 using the primers F-H2B-KOZAK and R-mIFP_EXTENSION to obtain “mIFP-H2B-6-P2A,” with 5' pWPXL homology and a 3' P2A sequence.

ii) PCR amplify tdTomato2-mito-7 using the primers F-MITO and R-tdTomatoLinker to obtain “tdTomato1,” the first tdTomato module, with 5' homology to P2A and 3' homology to the tandem linker.

iii) PCR amplify tdTomato2-mito-7 using the primers F-tdTomatoLinker and R-MITO to obtain “tdTomato2,” the second tdTomato module, with 5' homology to the tandem linker and 3' homology to P2A.

iv) PCR amplify EGFP-tubulin-6 using the primers F-EGFP_EXTENSION and R-TUBULIN to obtain “P2A-EGFP-tubulin-6,” with a 5' P2A sequence and 3' pWPXL homology.

v) Gibson Assembly of mIFP-H2B-6-P2A and tdTomato1 to produce “mIFP-H2B-6-P2A-tdTomato1,” with 5' pWPXL homology and 3' tandem linker homology.

vi) Gibson Assembly of tdTomato2 and P2A-EGFP-tubulin-6 to produce “tdTomato2-P2A-EGFP-tubulin-6,” with 5' tandem linker homology and 3' pWPXL homology.

- vii) PCR amplification of “mIFP-H2B-6-P2A-tdTomato1” using the primers F-H2B_KOZAK and R-tdTomatoLinker.
- viii) PCR amplification of “tdTomato2-P2A-EGFP-tubulin-6” using the primers F-tdTomatoLinker and R-TUBULIN.
- ix) Full Gibson Assembly of “mIFP-H2B-6-P2A-tdTomato1” and “tdTomato2-P2A-EGFP-tubulin-6” to produce the full 3-Reporter cassette.
- 4) The 3-Reporter cassette was cloned into the pWPXL backbone following a standard restriction enzyme cloning protocol.
- 5) The restriction digest product was transformed into NEB Competent DH5 α cells (NEB C2987) and plated onto carbenicillin-selection LB agar plates.
- 6) A standard Colony PCR protocol was used to screen for hits, using primers F-MITO (Table 3) and GA4400-R (Table 4) to amplify an expected ~2100 base pair segment.
- 7) Colony PCR hits were sent for full-coverage sequencing using the primers listed in (Table 4).

Gibson Assembly fragment	Input plasmid(s)	F-primer / R-primer	Annealing Temp. (Cycles 1-3) / (Cycles 4-30)	Expected band size (bp)	Elongation time (min)
mIFP-H2B-6-P2A	mIFP-H2B-6	F-H2B_KOZAK / R-mIFP_EXTENSION	55-65°C / 62-72°C (gradient)	~1400	2.0
tdTomato1	tdTomato-mito-7	F-MITO / R-tdTomatoLinker	55-65°C / 62-72°C (gradient)	~750	1.0
tdTomato2	tdTomato-mito-7	F-tdTomatoLinker / R-MITO	62-72°C / 62-72°C gradient	~750	1.0
P2A-EGFP-tubulin-6	EGFP-tubulin-6	F-EGFP_EXTENSION / R-TUBULIN	55-65°C / 62-72°C gradient	~2100	2.0
mIFP-H2B-6-P2A-tdTomato1	mIFP-H2B-6-P2A + tdTomato1	F-H2B_KOZAK / R-tdTomatoLinker	55-65°C / 62-72°C gradient	~2000	2.5
tdTomato2-P2A-EGFP-tubulin-6	tdTomato2 + P2A-EGFP-tubulin-6	F-tdTomatoLinker / R-TUBULIN	55-65°C / 62-72°C gradient	~2800	3.0

Table 2. Plasmids and PCR conditions for Gibson Assembly of 3Reporter lentivirus plasmid. Sequences of primers used to engineer 3Reporter lentivirus construct. Our three desired gene-reporter sequences were PCR amplified with custom primers to create areas of homology. PCR products were then joined using a succession of Gibson Assembly steps.

Primer Name	Sequence
F-H2B KOZAK	5'-agcctcgagggttaactacgggatccgggtaccgccaccatgcca-3'
R-mIFP_EXTENSION	3'-tcgaaacgtgtcagagtcaggtttccttcgcctcgatgattgaagtcg... ...gacgacttcgtcgaacctcgcacctcctctggacctgga-5'
F-MITO	5'-tggaggagaaccctggacctccgtcctgacgccgc-3'
R-tdTomatoLinker	3'-gccgtggcggaggaggctcctgtgttgaccgg-5'
F-tdTomatoLinker	5'-cggcaccgcctcctccgaggacaacaacatggcc-3'
R-MITO	3'-gcggtggtggacaaggacatcctgacctcctcgcacctgcttccttc... ...gcctcgatgattgaagtcggacgac-5'
F-EGFP_EXTENSION	5'-ggaagcggagctactaactcagcctgctgaagcaggctggagac... ...gtggaggagaaccctggacctgtgagcaaggcggaggac-3'
R-TUBULIN	3'-ctcccactcctctctcctctatgattcggccctgatcagtatactattagtggag-5'

Table 3. Primer sequences for PCR amplification of 3Reporter lentivirus plasmid components. Sequences of primers used to engineer 3Reporter lentivirus construct. Our three desired gene-reporter sequences were PCR amplified with custom primers to create areas of homology. Different homology regions are highlighted in different colors. grey = pWPXL vector homology; cyan = mIFP-H2B-6 homology; magenta = P2A homology; red = tdTomato-mito-7 homology; yellow = tdTomato tandem linker homology; green = EGFP-tubulin-6 homology.

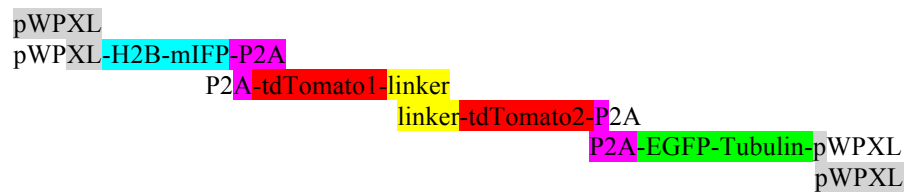


Figure 9. Schematic of Gibson Assembly of 3Reporter lentivirus expression plasmid.

The gene-reporter PCR products created are depicted in the above graphical representation and areas of homology are colored to show homologous regions for Gibson Assembly. Different homology regions are highlighted in different colors. grey = pWPXL vector homology; cyan = mIFP-H2B-6 homology; magenta = P2A homology; red = tdTomato-mito-7 homology; yellow = tdTomato tandem linker homology; green = EGFP-tubulin-6 homology.

Primer name	Sequence
pWPXL-F	5'-TTT TCC GAT CAC GAG ACT AGC CTC-3'
GA3800-R	5'-TTA GTA CCC TCG GAC ACG GC-3'
GA5600-R	5'-TTA GCC AGA AAC GCG TGG C-3'
GA6100-R	5'-CAC GAC GAC GTT CGG ACA GAA TTT-3'
GAv6_5000-R	5'-GAC CTC CTC GCC CTT GCT CAC CAT-3'
GAv6_5900-R	5'-CTT GGC GGT CTG GGT GCC CTC GTA-3'
GA4400-R	5'-GGC GGA TCT TGA AGT TCA CCT TGA-3'
GAv6_6500-R	5'-GGT GAA CAG CTC CTC GCC CTT GCT-3'
GA6700-R	5'-GTC ATC TCC TCC CCC AAT GGT C-3'
GA7350-R	5'-GGG AAG TGG ATG CGG GGG TA-3'
pWPXL-R	5'-GCA GCG TAT CCA CAT AGC GTA AAA GG-3'

Table 4. Primer sequences to confirm 3Reporter lentivirus plasmid sequence. Sequences of the comprehensive set of primers used to confirm successful production of the desired 3Reporter lentivirus plasmid. This (set) of primers covers the entire sequence from the 5' insert site of the original pWPXL plasmid, through mIFP-H2B, tdTomato-mito, and EGFP-tubulin, through to the 3' insert site the pWPXL plasmid. Primers were designed to produce PCR products with ~200 base pair overlap to ensure full sequencing coverage.

8) Sequencing hits were cultured in LB broth + carbenicillin and grown to $OD_{600} \sim 3.0$. Plasmids were transfected into 293T cells using the FuGENE 6 Transfection Reagent (Promega, E2691) and accompanying protocol. FuGENE 6 and DNA were mixed at a ratio of 6 μ L FuGENE : 1 μ g DNA. At 72h post-transfection, cells were examined under an epifluorescence microscope to ascertain fluorescence and proper cytostructural localization of gene-reporter products. The plasmid producing the brightest fluorescence was identified, aliquoted and stored at -20°C until ready for use. This plasmid was termed the 3-Reporter lentivirus expression plasmid.

9) 3-Reporter lentivirus was produced using the following 293T lentivirus production protocol:

i) Culture 293T cells in 10cm tissue culture plates in 10mL antibiotic-free cell culture media (DME H-21 + 10% FBS) at 37°C , 5% CO_2 . Culture cells for at least 12 hours until $\sim 70\text{-}80\%$ confluency is reached.

ii) For each 10cm plate, in a polypropylene tube, mix:

5.79 μ g 3-Reporter lentivirus expression plasmid

4.34 μ g psPAX2 lentivirus packaging plasmid (Addgene, #12260)

1.45 μ g pMD2.G lentivirus enveloped plasmid (Addgene, #12259)

(x) μ L serum-free OPTI-MEM (Gibco, 31985-070)

to 115.8 μ L total volume

iii) To prepare the FuGENE 6 master mix, carefully combine the following (for each 10 cm dish):

34.7 μ L FuGENE 6 Transfection Reagent (Promega, E2691)

428.5 μ L serum-free OPTI-MEM (Gibco, #31985-070)

463.2 μ L total volume

Add FuGENE 6 directly to the OPTI-MEM without touching the sides of the tube. Mix by flicking or gentle pipetting and incubate mixture for 5 minutes at room temp.

iv) Add the plasmid mixture from step (2) to the FuGENE 6 master mix from step (3) and incubate mixture for 20-30 minutes at room temp.

v) Add the FuGENE 6 + plasmid mixture from step (4) directly to the 10cm dish of 293T cells.

Swirl the plate to mix and incubate cells at 37°C, 5% CO₂, overnight for 12-15 hours.

vi) After 12-15 hours, remove the transfection media and replace with full cell culture media

(DME H-21 + 10% FBS + 1x pen/strep). Incubate at 37°C, 5% CO₂ for 24 hours.

vii) After 24 hours, harvest the media (1st harvest) into a polypropylene tube and store at 4°C.

This media contains active lentivirus. Replace media with fresh full cell culture media (DME

H-21 + 10% FBS + 1x pen/strep). Incubate at 37°C, 5% CO₂ for 24 hours.

viii) After 24 hours, harvest the media again (2nd harvest) and pool with the media from the 1st

harvest. Proceed to step (ix) to concentrate the lentivirus, or store at 4°C for up to 2 days before concentrating.

ix) Filter media through a 0.45µm PVDF membrane filter (Millipore, SLHVM33RS) to remove

cell debris. Concentrate lentivirus using Lenti-X Concentrator (Clontech, PT4421-2) and the

accompanying protocol, resuspending the lentivirus in DME H-21 + 10% FBS.

x) Store lentivirus in single-use aliquots at -80°C until ready for use. Avoid freeze-thaw cycles.

10) The 3-Reporter lentivirus was titered to determine the optimal lentivirus titer for live cell experiments. Passage 1 (P1) WT MEFs were seeded into 96-well tissue culture plates (Greiner #655090) at a density of 5000 cells/well in antibiotic-free cell culture media (DME H-21 + 10% FBS). Lentivirus was titered at 10, 20, 40, 60, 80, and 100µL virus in 200µL total volume antibiotic-free cell culture media and cells observed 72 hours post-transduction. The lentivirus titer that produced the highest transduction efficiency without producing phenotypically noticeable signs of cell death or stress was identified and chosen as the optimal lentivirus titer. Note: Polybrene is a commonly used reagent to augment transduction efficiency. However, when we tested polybrene addition at 8ug/uL, we observed no discernible increase in transduction efficiency, so elected not to use polybrene in subsequent lentivirus transductions.

11) To prepare cells for live-cell imaging, Passage 1 (P1) WT MEFs were seeded into 96-well tissue culture plates (Greiner #655090) at a density of 5000 cells/well in antibiotic-free cell culture media

(DME H-21 + 10% FBS). After 24 hours, the appropriate titer of 3-Reporter lentivirus and antibiotic-free cell culture media were added to a final volume 200 μ L/well. At 24 hours post-transduction, cells were trypsinized and seeded into a new 96-well cell culture plate (Greiner #655090) at a density of 500 cells/well in 200 μ L full cell culture media (DME H-21 + 10% FBS + 1x pen/strep). After an additional 24 hours (48 hours post-transduction), media was replaced with 200 μ L full cell culture media containing 100 μ M biliverdin hydrochloride (BV; Sigma, #30891). BV is a cofactor required for mIFP fluorescence (Yu et al., 2015). Cells were incubated under 100 μ M BV media at 37°C, 5% CO₂ for 24 hours. Immediately prior to imaging (72h post-transduction), BV media was removed (BV is autofluorescent in nature), cells washed 3x with PBS, and re-incubated under full cell culture media.

3b. Time-Lapse Imaging in Live Cells

Cells were imaged at the UCSF Nikon Imaging Center (NIC) on a high-speed confocal microscope fitted with a Plan Apo λ 40x objective (NA 0.95) equipped with 405, 488, 561, and 640 nm laser lines and 450/50m (DAPI), 525/50m (FITC), 600/50m (Cy3), and 700/75m (Cy5) filters. A stage-top temperature and CO₂ control chamber was set to 37°C and 0.3 l/min to mimic tissue culture conditions. Cells were imaged at 2h intervals over a 60h time course in the brightfield (BF), GFP (EGFP-tubulin), RFP (tdTomato-mito-7), and Cy5 (mIFP-H2B) channels at 100ms, 300ms, 300ms, and 300ms exposure, respectively (Fig. 10).

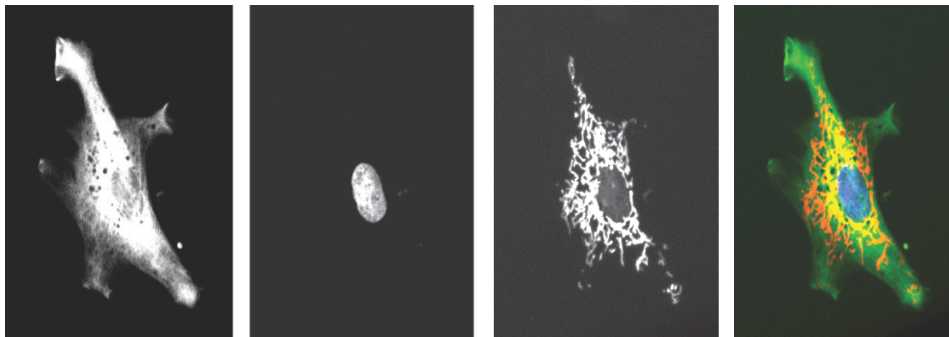


Figure 10. Example fluorescence image of a live WT MEF. A single cell expressing EGFP-tubulin (microtubule cytoskeleton), mIFP-H2B (nucleus), and tdTomato-mito-7 (mitochondria). A composite image is shown on the far right, with the microtubule cytoskeleton depicted in green, the nucleus depicted in blue, and the mitochondria depicted in red. Image taken with 40x magnification on a spinning disk confocal microscope.

3c. Dynamics of Cellular Transitions in Morphology Space

After imaging, we used our earlier developed suite of custom image analysis algorithms to extract 205 morphometric and textural features from each time frame, analyzing up to 30 time frames per cell. The exact number of time frames analyzed per cell varied depending on several factors (e.g. segmentation difficulties, cells moving out of the FOV, etc.) To visualize and quantify morphological changes, we plotted transition vectors within morphology space, with each vector origin defined at $(PC1_{(t)}, PC2_{(t)})$ and vector terminus defined at $(PC1_{(t+2h)}, PC2_{(t+2h)})$. In subsequent experiments, morphology data was recorded at 2h intervals, but due to microscope autofocus issues, data was only viable for analysis at every other time point (4h intervals). To facilitate a meaningful comparison between different datasets, we plotted the dataset at 4h intervals, such that vector origins are defined at $(PC1_{(t)}, PC2_{(t)})$ and vector termini defined at $(PC1_{(t+4h)}, PC2_{(t+4h)})$. A map of the raw transition vectors is presented in (Fig. 11).

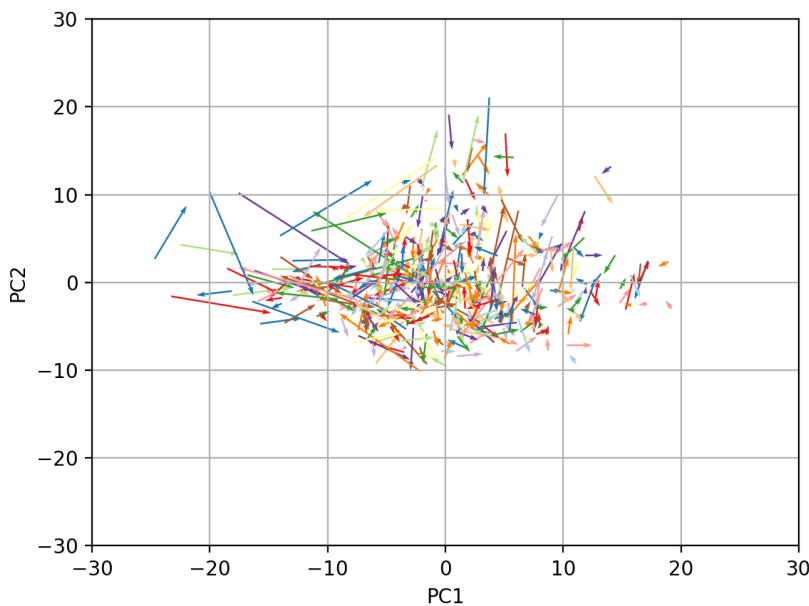


Figure 11. Plot of raw WT MEF transition vectors. Changes in morphology are depicted as transition vectors in the morphology space defined by PC1 vs. PC2. Transition vectors were calculated at 4h time intervals such that the origin of each vector is found at $(PC1_{(t)}, PC2_{(t)})$ and the terminus of each vector found at $(PC1_{(t+4h)}, PC2_{(t+4h)})$. Transition vectors have been scaled down by a factor of 1.5 to facilitate visualization of vectors.

This initial raw vector map appeared over-crowded, rendering it difficult to assess the dynamic properties of morphology space. To distill this transition map, we binned the morphology space defined by PC1 vs. PC2 into a 60x60 bin array, with each x-axis bin representing a single unit along PC1, and each y-axis bin representing a single unit along PC2. We then averaged the magnitude and direction of vectors originating from each bin (e.g. if there were three raw vectors originating from a single bin, we calculated their average vector) and plotted these vectors on a bin-by-bin basis, as depicted in (Fig. 12). This plot revealed underlying non-uniformities in the dynamics of morphology space. Notably, transition vectors originating in the central (0, 0) region of morphology space were, on average, of smaller magnitude than those originating at the periphery. This suggests that, over the same time interval, the degree of morphological change exhibited by a cell varies as a function of the starting morphological state of the cell.

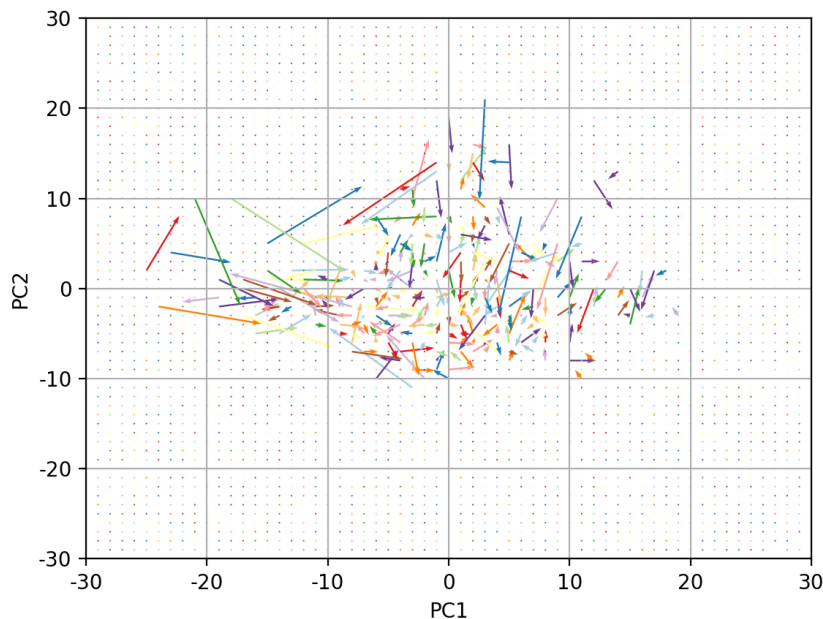


Figure 12. Plot of bin-by-bin average WT MEF transition vectors. Transition vectors are averaged on a bin-by-bin basis in the morphology space defined by PC1 vs. PC2, binned into a 60x60 bin array. Transition vectors were calculated at 4h time intervals such that the origin of each vector is found at $(PC1_{(t)}, PC2_{(t)})$ and the terminus of each vector found at $(PC1_{(t+4h)}, PC2_{(t+4h)})$. The transition vector map is characterized by smaller-magnitude transitions towards the center (0, 0) of PC space, whereas transitions towards the periphery tend to be of larger magnitude. Transition vectors have been scaled down by a factor of 1.5 to facilitate visualization of vectors.

This observation was further supported by a 2-dimensional colored surface plot (Fig. 13) of the average magnitude of vectors originating from each bin. In this plot, the average magnitude is represented by a ROYGBIV color bar, with red indicating a large average magnitude and violet indicating a small average magnitude. This plot revealed that transitions originating from the central (0, 0) region of morphology space tended to be of smaller magnitude (blue, light blue) compared to those originating from more peripheral bins of morphology space (orange, red). These results suggest that the degree of morphological change within a given time interval varies as a function of the starting morphological state of a cell, with cells near (0, 0) in morphology space undergoing, on average, less dramatic morphological changes (as measured in PC1 and PC2 units) over the same time interval when compared to cells occupying more peripheral states of morphology space. These observations present strong evidence of non-uniformity in the transition dynamics of WT MEF morphology space.

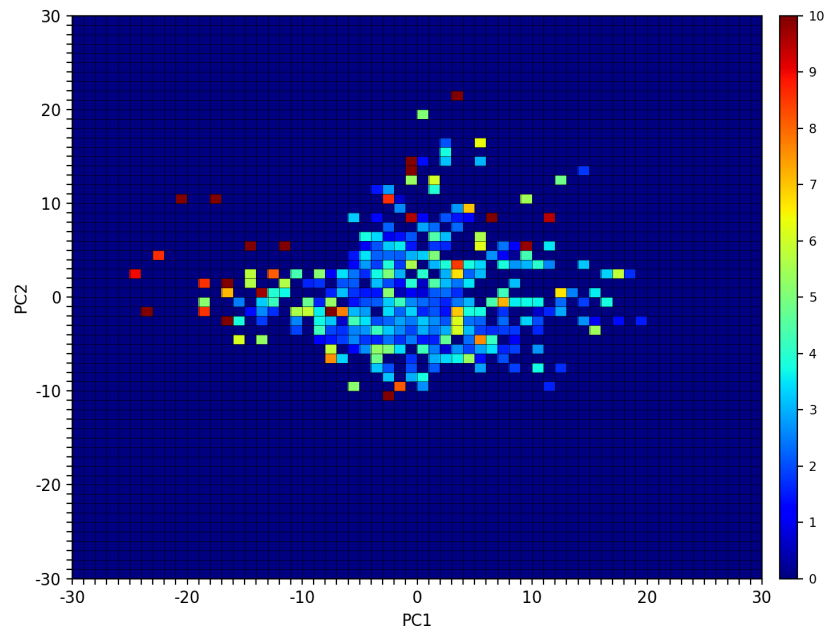


Figure 13. Colored surface plot of bin-by-bin average WT MEF transition magnitudes. The average magnitude of transition vectors are plotted as a colored surface plot on a bin-by-bin basis in the morphology space defined by PC1 vs. PC2, binned into a 60x60 bin array. Transition vectors were calculated at 4h time intervals such that the origin of each vector is found at $(PC1_{(t)}, PC2_{(t)})$ and the terminus of each vector found at $(PC1_{(t+4h)}, PC2_{(t+4h)})$. This colored surface plot reveals that, on average, WT MEFs occupying morphological states closer to the center (0, 0) of PC space exhibit smaller morphological changes when compared to those occupying more peripheral states of morphology space. This reveals that WT MEF morphology space is dynamically non-uniform and that the extent of morphological change is influenced by the existing morphological state.

The transition vector maps are notably absent of closed flux loops, suggesting that morphological transitions cannot be described as a deterministic process. In other words, the next morphological state of a cell cannot be readily predicted from its current state. In theory, the lack of population-scale deterministic dynamics does not necessarily imply a purely stochastic process, as subsets of cell may still exhibit distinctive patterns in subspace (e.g. subsets of cells may be constrained to subspaces of morphology space, or display more or less morphological heterogeneity over a given time interval). To better understand the extent of intercellular heterogeneity in both state space occupancy and transition dynamics, we calculated the mean (PC1, PC2) coordinate as well as transition vector for each cell across all time frames and plotted these into morphology space (Fig. 14). This plot revealed that WT MEFs display intercellular heterogeneity in the average magnitude, magnitude variance, and directionality of their morphology space transitions.

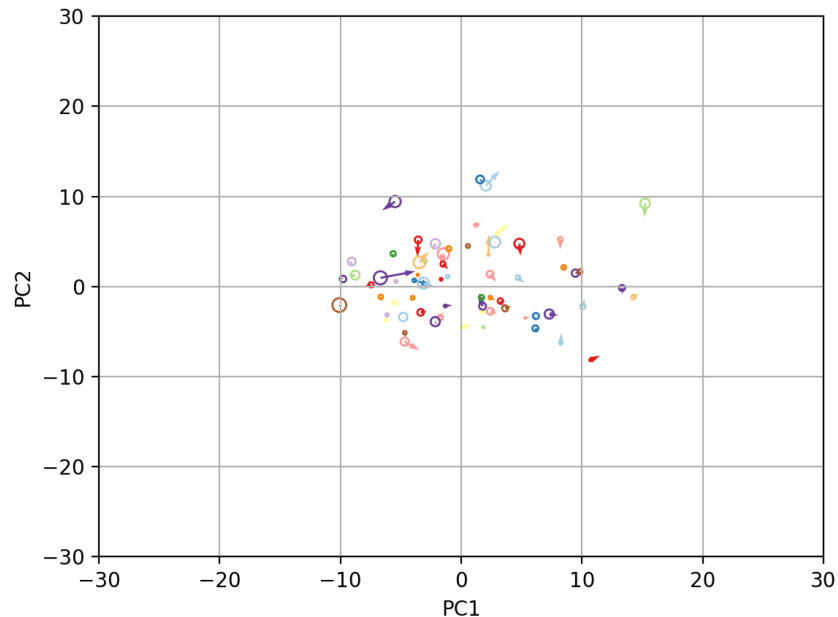


Figure 14. Plot of mean morphology space states and transition vectors of single WT MEF cells. Plot of the average coordinate and average transition vector on a single-cell basis. Each vector represents a different cell, tracked over a 60h time course. The average (PC1, PC2) coordinate of each cell is found at the origin of each vector. The radius of the circle at the origin of each vector is defined as 2x the variance of the positional variance of that cell. Smaller radii circle indicate more localized movement of the cell in morphology space, while larger radii circle indicate more extensive movement of that cell in morphology space. Transition vectors were calculated at 4h time intervals such that the origin of each vector is found at $(PC1_{(t)}, PC2_{(t)})$ and the terminus of each vector found at $(PC1_{(t+4h)}, PC2_{(t+4h)})$. This map of the average transition vectors reveals significant intercellular variability in morphology space occupancy and transition dynamics. Transition vectors have been scaled down by a factor of 1.5 to facilitate visualization of vectors.

To develop a more spatially nuanced understanding of the space state organization of transition dynamics, we binned WT MEF morphology space into a 10x10 bin array and plotted the probability density function (pdf; Fig. 15, far left) of WT MEFs on a bin-by-bin basis. This revealed a peak in the probability density function near the central (0, 0) region of PC space. This result is in agreement with earlier observations (Fig. 12, Fig. 13) of transitions originating from this central region being, on average, of smaller magnitude than those originating along the periphery. These smaller magnitude transitions are predictive of and in agreement with the observed increase in probability density in this region.

After establishing the probability density function of WT MEF morphology space, we developed a series of probability plots to probe the dynamics underlying this probability density function. We began by plotting the probabilities of entering (p_{enter} ; Fig. 15, near left) and exiting (p_{exit} ; Fig. 15, center) each bin. An entry event is defined as a transition vector terminating within a specific bin, while an exit event is defined as a transition vector originating within a specific bin. The probabilities were calculated by summing the total number of entry/exit events across the 60h time course and calculating the probability of entry/exit events occurring within each specific bin. For example, if there were N total tallied transitions, if n_x of these transitions originated in bin_x , the calculated p_{exit} of bin_x would be n_x/N , while if n_y of these transitions terminated in bin_y , then the calculated p_{enter} of bin_y would be n_y/N .

The combination of p_{enter} and p_{exit} plots revealed a higher-than-average probability of entering bins in the central (0, 0) region relative to peripheral bins, further underlining the non-uniform nature of transition dynamics in WT MEF morphology space. Though there were higher-than-average probabilities of entering these central bins, these were accompanied by concomitant higher-than-average probabilities of exit. These results suggest an interpretation of these central bins as an energetically favorable subspace acting as a local state space attractor and producing increased probability density in this region. In more biological terms, these results indicate that WT MEFs exhibit biases towards specific morphologies, but that transitions into these morphologies are not irreversible, as evidenced by the observed higher-than-average exit probabilities.

To test this hypothesis, we plotted the probability of staying within the same bin between adjacent time points (p_{stay} ; Fig. 15, near right). This plot revealed dramatically increased probabilities of staying within these central bins relative to peripheral bins, supporting our interpretation of an energetically favorable subspace in this central region. To test the lifetime of this state space bias, we plotted the probability, over a 60h time course, that the bin currently occupied would be the same bin in which the cell concluded its time course (p_{end} ; Fig. 15, far right). This calculation represents a rough measure of long-term occupancy and revealed a mildly higher-than-average p_{end} within the central region; however this increase in probability was minimal in comparison with that observed in the plot of p_{stay} . These results suggest that, while there is a bias towards occupancy of this central region due to the existence of a local state space attractor, entry into these states is reversible and does not impose long-term occupancy.

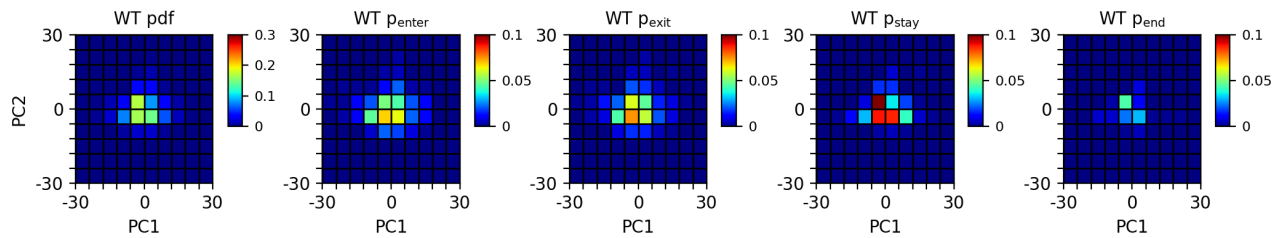


Figure 15. Probability plots of WT MEF density functions and transition dynamics. Colored surface plots to visualize various aspects of WT MEF transition dynamics. A plot of the probability density function (pdf, far left) shows non-uniform occupancy of WT MEF morphology space, with a higher density of cells in the central (0, 0) region of morphology space. A plot of the probability of entering a bin (p_{enter} , near left) reveals a higher probability of entering these central states, while a plot of the probability of exiting a bin (p_{exit} , center) reveals a corresponding higher probability of exiting these central states, suggesting that entry into this space is energetically favorable, but not irreversible. This interpretation is further supported by a plot of the probability of staying in the same bin between time points (p_{stay} , near right), which shows a short-term preference for continued occupancy of these central states, while a plot of the probability of being in the same bin as that occupied at the end of the time course (p_{end} , far right) reveals a mild long-term occupancy, again supporting the interpretation of an energetically favorable subspace in morphology space that acts as a local attractor but does not impose long-term occupancy.

3d. Boltzmann Statistics and Energy Landscapes

While transition vector maps and probability plots provided several important insights into the dynamics of WT MEF morphology space, our observations up to this point had been primarily qualitative in nature. To develop a more quantitatively rigorous understanding of WT MEF morphology space, we turned to statistical mechanical theory. We developed an adaptation of the Boltzmann distribution (Eq. 10), which describes the probability density function of a system as a function of the temperature and

energy states of that system, and applied this to our two-dimensional Principal Component-based morphology space. We then used this adaptation to map out the underlying energy landscape of WT MEF morphology space.

$$\frac{\bar{n}_s}{N} = \frac{e^{-\beta\xi_s}}{\sum_r e^{-\beta\xi_r}} = \frac{e^{-\beta\xi_s}}{Z} \quad (\text{Eq. 10})$$

The equation for the Boltzmann distribution is as stated in (Eq. 10), where \bar{n}_s is the average number of particles found in a state s with energy level, ξ_s , N is the total number of particles in the system, r is the total number of energy states of the system, and $\beta = 1 / k_B T$, where k_B is the Boltzmann constant ($k_B = 1.381 \cdot 10^{-23} \text{ m}^2 \text{ kg s}^{-2} \text{ K}^{-1}$) and T is the temperature of the system. Z represents the partition function, or the sum of $e^{-\beta\xi_s}$ over all possible energy states, which is equal to 1.

In our case, we were able to use our experimental data to calculate values for several of the above variables. The value \bar{n}_s/N , is simply the probability density at each bin, while T is the “temperature” of WT MEF morphology space. To calculate an effective temperature for WT MEF morphology space, we abstracted transition vectors to represent particle velocity vectors and used the equipartition theorem to derive temperature from the average velocity of a particle in a two-dimensional plane, where each available dimension of movement contributes $\frac{1}{2}k_B T$ kinetic energy to the system. Given a two-dimensional plane, the total kinetic energy of the system is equal to $k_B T$. We then derived the following:

$$\frac{1}{2} m \bar{v}^2 = k_b T \quad (\text{Eq. 11})$$

$$T = \frac{m \bar{v}^2}{2k_b} \quad (\text{Eq. 12})$$

Using this approach, we calculated the average transition vector magnitude and ensuing effective temperature, T_{WT} , of WT MEF morphology space.

A complication arose when we tried to solve for ξ_s in the Boltzmann distribution in that we lacked *a priori* information about the energy states ($\xi_1, \xi_2, \xi_3, \xi_4, \dots, \xi_s$) of the system, information that is needed to calculate the partition function, Z , in the denominator. However, since we have information about the occupancy density of each state, we can mathematically manipulate (Eq. 10) to eliminate the partition

function from this equation. If we consider a system with 5 possible energy states, ξ_1 , ξ_2 , ξ_3 , ξ_4 , and ξ_5 , we can write the following equation:

$$\frac{\bar{n}_1 + \bar{n}_2 + \bar{n}_3 + \bar{n}_4 + \bar{n}_5}{N} = \frac{e^{-\beta\xi_1}}{\sum_r e^{-\beta\xi_r}} + \frac{e^{-\beta\xi_2}}{\sum_r e^{-\beta\xi_r}} + \frac{e^{-\beta\xi_3}}{\sum_r e^{-\beta\xi_r}} + \frac{e^{-\beta\xi_4}}{\sum_r e^{-\beta\xi_r}} + \frac{e^{-\beta\xi_5}}{\sum_r e^{-\beta\xi_r}} \quad (\text{Eq. 13})$$

We know that the sum of the probability density function must equal 1 and that each term on the right-hand side of the equation is equal to the corresponding \bar{n}_s/N term on the left-hand side of the equation. Since there is a uniform denominator on the right-hand side, the denominator here essentially acts as a weighting factor. We can thus eliminate it, despite the fact that we cannot directly calculate its value. A simplification of (Eq.10) produces:

$$\frac{\bar{n}_1 + \bar{n}_2 + \bar{n}_3 + \bar{n}_4 + \bar{n}_5}{N} = e^{-\beta\xi_1} + e^{-\beta\xi_2} + e^{-\beta\xi_3} + e^{-\beta\xi_4} + e^{-\beta\xi_5} \quad (\text{Eq. 14})$$

where $\bar{n}_1/N = e^{-\beta\xi_1}$, $\bar{n}_2/N = e^{-\beta\xi_2}$, $\bar{n}_3/N = e^{-\beta\xi_3}$, etc. This allows us to write the generalized form of this equation as:

$$\frac{\bar{n}_s}{N} = e^{-\beta\xi_s} \quad (\text{Eq. 15})$$

From our dataset we can directly calculate values for \bar{n}_s/N , as well as β , leaving us with a single unknown: the energy level, ξ_s . We solve for ξ_s by rearranging (Eq. 15) to give:

$$\xi_s = \frac{\ln(\frac{\bar{n}_s}{N})}{-\beta} \quad (\text{Eq. 16})$$

We use a Boltzmann constant of $k_b = 1.381 \cdot 10^{-23} \text{ m}^2 \text{ kg s}^{-2} \text{ K}^{-1}$ and calculated values of the effective WT temperature, T_{WT} , and probability density function, to calculate the effective energy landscape of WT MEF morphology space. A surface plot of the energy landscape (Fig. 16) revealed a single global minimum near the central (0, 0) region of morphology space, in agreement with the observations of increased population density in this subspace as well as transitions originating from this subspace being of smaller-than-average magnitude. This adaptation of the Boltzmann distribution provides a quantitative framework for calculating the energy landscapes underlying morphology space, allowing us to meaningfully compare morphology space dynamics under different perturbations, as we discuss in Chapter 4.

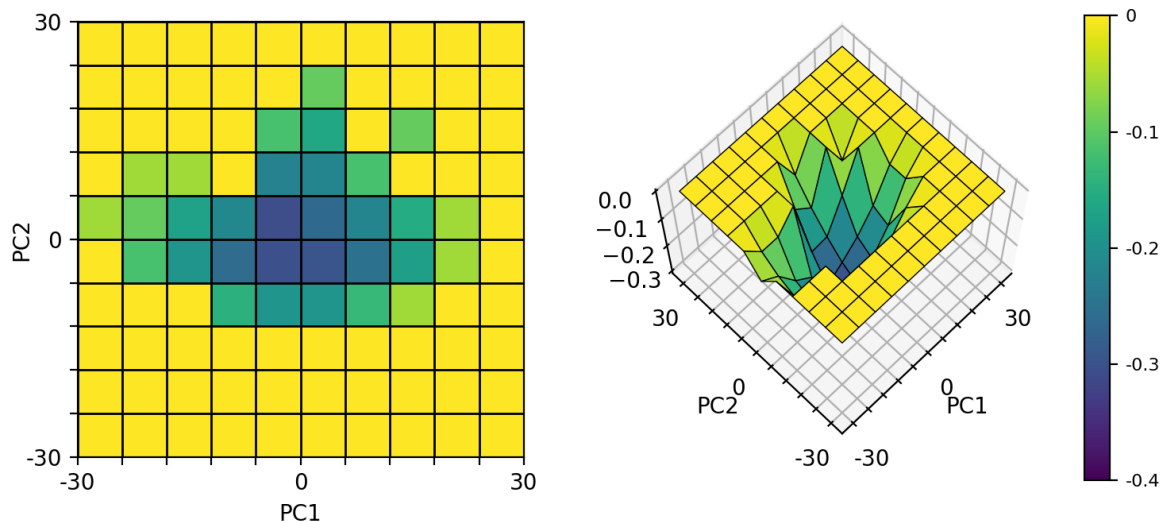


Figure 16. Plot of the effective energy landscape of WT MEF morphology space. Colored surface plot of the calculated effective energy landscape of WT MEF morphology space. The landscape was calculated using the Boltzmann distribution by abstracting transition vectors as velocity vectors and calculating an effective temperature. A plot of the effective energy landscape reveals a single global minimum at the center (0, 0) of PC space, in agreement with earlier observations of increased population density at these locations as well as smaller-magnitude transition vectors. This energy landscape effectively explains the non-uniform occupancy and transition dynamics of WT MEF morphology space. All energy values were shifted down by $0.4 \cdot 10^{-19}$ (plotted energy = calculated energy - $0.4 \cdot 10^{-19}$) to facilitate visualization of the energy landscape.

3e. Results and Interpretation

Our live cell experiments revealed several interesting characteristics of WT MEF morphology space. First, plots of the transition vectors of WT MEFs within morphology space are not characterized by closed flux loops, indicating that morphological transitions cannot be described as a deterministic process. Instead, they are likely, at least in part, driven by stochastic processes. Secondly, the magnitude of morphological transition varies as a function of space state, where transition vectors originating in the central region near (0, 0) of tend to be of smaller-than-average magnitude, while those originating from more peripheral states tend to be of larger-than-average magnitude. These results suggest that morphology space is energetically non-uniform, an interpretation supported by observations of smaller-than-average magnitude transition vectors as well as increased probability density in this cell region.

Through an adaptation of the Boltzmann distribution, we were able to use live cell morphology data to map out the energy landscape underlying WT MEF morphology space, discovering that it is characterized by a single global minimum in the central (0, 0) region of PC space. Through a series of probability plots, we determined that entry into this space is energetically favorable, but not irreversible.

Further analysis of the time scales of occupancy reveal a bias towards short-term occupancy of these central bins, but that this bias does not extend into long-term occupancy. The ensemble of these results lead us to a model of WT MEF morphology space characterized by a single global minimum that acts as a state space attractor, entry into which is reversible and does not entail long-term commitment.

CHAPTER 4. Relationships Between Morphological and Functional Heterogeneity

In this chapter we look to expand our understanding of morphological heterogeneity by exploring the relationship between morphological and functional heterogeneity. There have been many studies over the years indicating that isogenic populations can exhibit functional heterogeneity. These include variability in drug survival rates (Bigger, 1944), DNA competency (Maamar et al., 2007), and differentiation potential (Chang et al., 2008). In these examples, the observed functional variability was shown to correlate with variability in gene expression, driven by the stochastic nature of the cellular transcription process. Here we investigate morphological heterogeneity as a potential sister mode of non-genetic heterogeneity and discover that morphological heterogeneity exhibits correlative links to functional heterogeneity. These findings contribute to our understanding of the myriad ways in which ex-genome factors can influence cellular state and behavior.

4a. Heterogeneous Response to Apoptosis Induction

To investigate the relationship between morphological and functional heterogeneity, we screened a panel of five apoptosis inducers (Apoptosis Inducer Kit, abcam ab102480) for conditions inducing a non-uniform apoptotic response in WT MEFs. We decided to assay apoptotic response as opposed to other functional outputs due to several favorable factors, including ease of induction, a diverse array of available induction agents, and the existence of a visually identifiable endpoint. The drug panel, consisting of actinomycin D, camptothecin, cycloheximide, dexamethasone, and etoposide, was screened across a range of concentrations for conditions producing non-uniform apoptosis in WT MEFs. We identified 2 μ M camptothecin as a promising candidate (Fig. 17) due to it producing a noticeable, but incomplete apoptotic response across the population. We decided to further study this phenomenon at the single-cell level and investigate the possibility of a correlation between morphological heterogeneity and heterogeneity in apoptotic response.

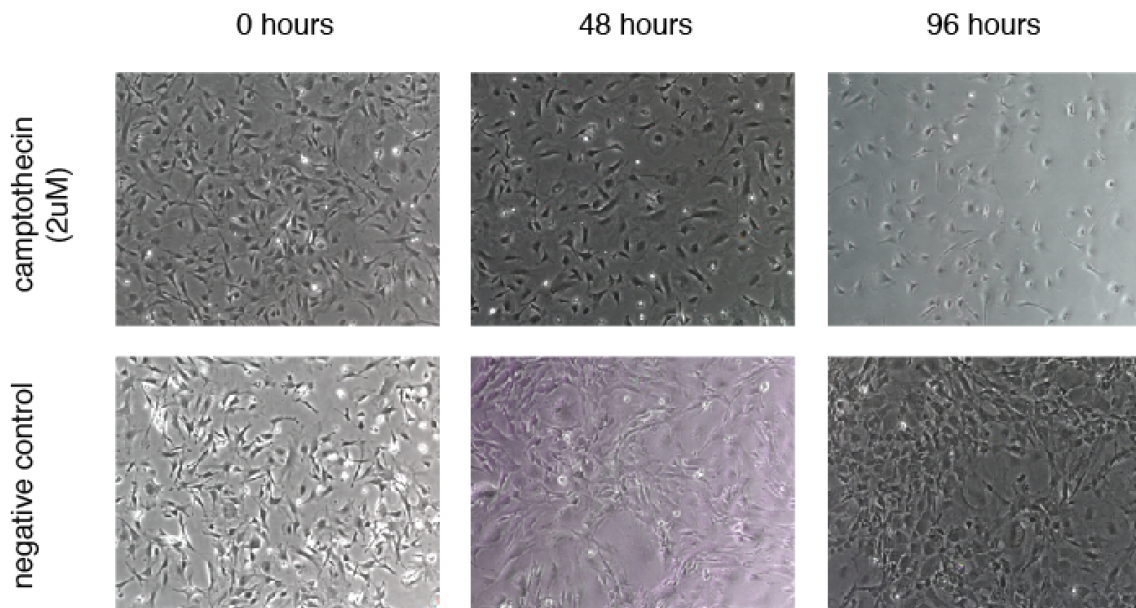


Figure 17. Non-uniform apoptotic response in WT MEFs in response to camptothecin induction. Phase microscopy images taken of WT MEFs under 2 μ M camptothecin induction. Images taken at 0h (left panels), 48h (center panels), and 96h (right panels) post-induction. Cells were incubated under either 2 μ M camptothecin cell culture media (top panels), or in a negative control 0 μ M camptothecin cell culture media (bottom panels). Fractional depletion of cells can be seen in response to 2 μ M camptothecin, with increasing population sparsity but a lack of global/complete/total apoptosis. Over the same time course, negative control cells are observed to exhibit increasing density and expand to high confluence. Images taken at 4x magnification.

4b. Time-Lapse Imaging of Live Cell Response to Camptothecin

To investigate the morphological behavior of WT MEFs under camptothecin induction, we followed a series of experimental steps similar to those initially developed for the WT MEF live cell tracking experiments. We began by preparing cells for live cell imaging following Step 11 (Chapter 3, pg. 29-30) of the previously established protocol. We then imaged cells at the UCSF Nikon Imaging Center (NIC) on a high-speed confocal microscope fitted with a Plan Apo λ 40x objective (NA 0.95) equipped with 405, 488, 561, and 640 nm laser lines and 450/50m (DAPI), 525/50m (FITC), 600/50m (Cy3), and 700/75m (Cy5) filters. A stage-top temperature and CO₂ control chamber was set to 37°C and 0.3 l/min to mimic tissue culture conditions. Cells were imaged at 2h intervals over a 64h time course in the brightfield (BF), GFP (EGFP-tubulin), RFP (tdTomato-mito-7), and Cy5 (mIFP-H2B) channels at 100ms, 300ms, 300ms, and 300ms exposure, respectively (FIG). To induce apoptosis, we added the appropriate volume and concentration of camptothecin at the second time interval (4h into the experiment) to bring the total well volume to 200 μ L and the final camptothecin concentration to 2 μ M.

4c. Changing Dynamics of Morphology Space in Response to Camptothecin

We visually examined the series of time lapse images and identified a total of 33 cells that were suitable for further analysis. In these cells, the fluorescence signal was bright enough to permit segmentation and feature analysis; cells eliminated from analysis were eliminated for having weak fluorescence signal, being in contact with other cells and/or the well edge, and/or having frames compromised by floating debris. Over the course of a 64h time lapse, we identified 17 of 33 (52%) cells that underwent apoptosis, while 16 of 33 (48%) cells showed no visible signs of apoptosis (Fig. 18).

Cells that either did or did not undergo apoptosis over the course of the 64h time lapse time were classified as either Apoptosis[+] or Apoptosis[-] cells, respectively. Operating under the hypothesis that morphological heterogeneity might engender functional heterogeneity, we plotted the two classes of cells into WT MEF morphology space and examined their dynamics in morphology space. To better understand the dynamical behavior of each class of cells, we plotted three transition vector maps for each class; these vector maps were analogous to those first developed to analyze the dynamics of untreated WT MEFs (Chapter 3, pg. 31-34). In combination, these maps present a strong case for a relationship between dynamical and state space variability and functionally divergent behavior at the cellular level.

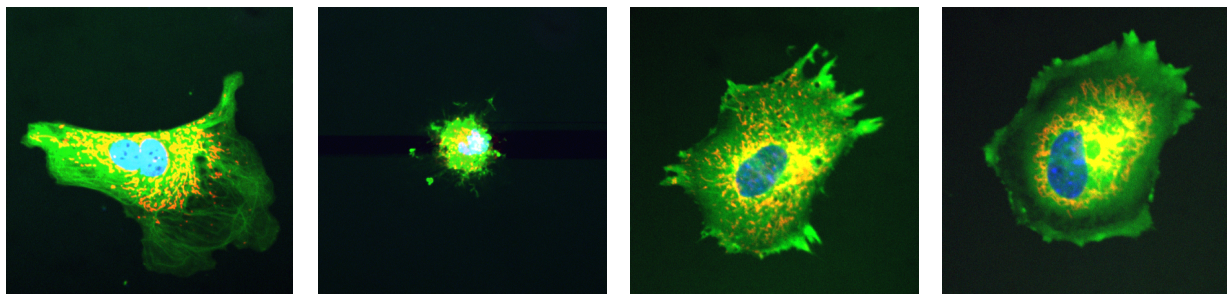


Figure 18. Example fluorescence images of WT MEFs under camptothecin induction. The images above are live-cell images of WT MEFs transduced with the 3-Reporter lentivirus; EGFP- α -tubulin is shown in green (microtubule cytoskeleton), mIFP-H2B is shown in blue (nucleus), and tdTomato-mito-7 is shown in red (mitochondria). The two panels on the left are images of a cell that we identified as having undergone apoptosis (Apoptosis[+]); the far left panel is the first frame of a 64h time course, while the near left panel is the last frame. The characteristic blebbing and implosion of apoptotic cells can be observed. The two panels on the right are images of a cell that we identified as not having undergone apoptosis (Apoptosis[-]); the near right panel is the first frame of a 64h time course, while the far right panel is the last frame. Images taken at 40x magnification on a spinning disk confocal microscope.

To better understand potential variability in the dynamics of Apoptosis[+] and Apoptosis[-] cells in morphology space, we plotted raw transition vector plots for each class of cells, with vector origins defined at $(PC1_{(t)}, PC2_{(t)})$ and vector termini defined at $(PC1_{(t+4h)}, PC2_{(t+4h)})$. In these plots, Apoptosis[+] cells exhibited increased population density in the central (0, 0) region of morphology space and a distinct directional bias towards the upper left (-30, 30) corner of morphology space. Meanwhile, Apoptosis[-] cells similarly exhibited increased population density in this central region (0, 0) of PC space, but their transition vectors appeared, on average, to be of smaller magnitude than those of Apoptosis[+] cells. Furthermore, there was no indication of a directional bias towards the upper left (-30, 30) corner of PC space. Instead, we observed several large-magnitude transition vectors in the far right (30, 0) region of PC space, suggesting a directional bias towards this region. In contrast, Apoptosis[+] cells exhibit no occupancy in this region.

To distill the raw transition vector map into a more interpretable vector map, we binned morphology space into a 60x60 bin array and plotted the average transition vector on a bin-by-bin basis (Fig. 20). We observed again that the two classes of cells exhibited directional biases towards different regions of morphology space, with Apoptosis[+] cells biased towards the upper left (-30, 30) corner of PC space, and Apoptosis[-] cells biased towards the far right (30, 0) region of PC space.

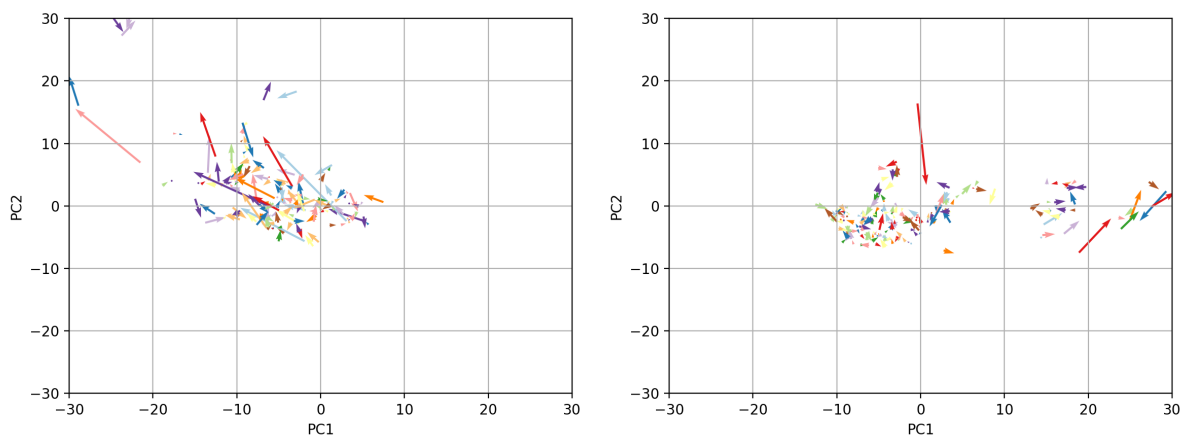


Figure 19. Plots of raw Apoptosis[+]/[-] transition vectors. Changes in morphology are depicted as transition vectors in the morphology space defined by PC1 vs. PC2, with Apoptosis[+] transition vectors plotted on the left, and Apoptosis[-] transition vectors plotted on the right. Transition vectors were calculated at 4h time intervals such that the origin of each vector is found at $(PC1_{(t)}, PC2_{(t)})$ and the terminus of each vector found at $(PC1_{(t+4h)}, PC2_{(t+4h)})$. Transition vectors have been scaled down by a factor of 1.5 to facilitate visualization of vectors.

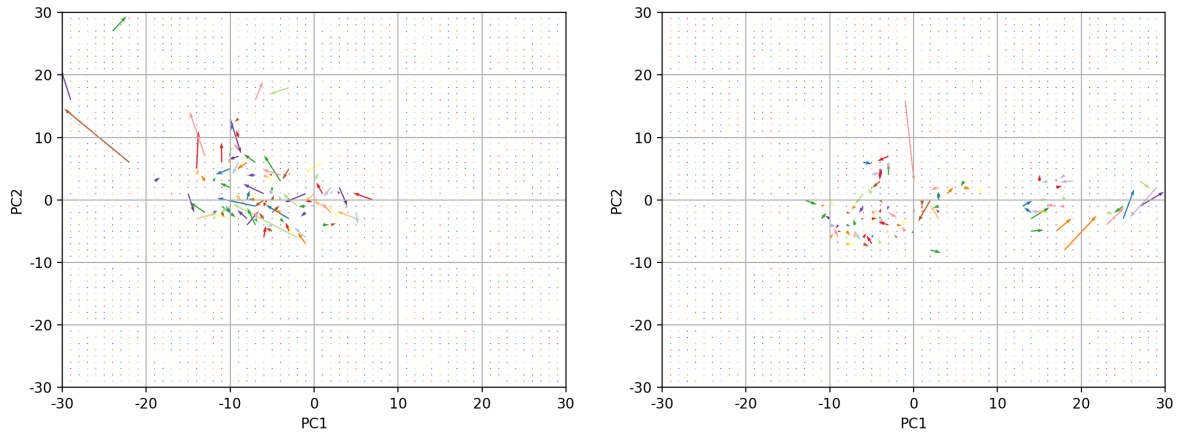


Figure 20. Plots of bin-by-bin average Apoptosis[+]/[-] transition vectors. Transition vectors are averaged on a bin-by-bin basis in the morphology space defined by PC1 vs. PC2, binned into a 60x60 bin array, with Apoptosis[+] transition vectors plotted on the left, and Apoptosis[-] transition vectors plotted on the right. Transition vectors were calculated at 4h time intervals such that the origin of each vector is found at $(PC1_{(t)}, PC2_{(t)})$ and the terminus of each vector found at $(PC1_{(t+4h)}, PC2_{(t+4h)})$. Apoptosis[+] cells exhibit larger-than-average transition vectors along with a directional bias towards the upper left $(-30, 30)$ region of morphology space. In contrast, Apoptosis[-] cells exhibit smaller-than-average transition vectors, along with a directional bias towards the far right $(30, 0)$ region of morphology space. Transition vectors have been scaled down by a factor of 1.5 to facilitate visualization of vectors.

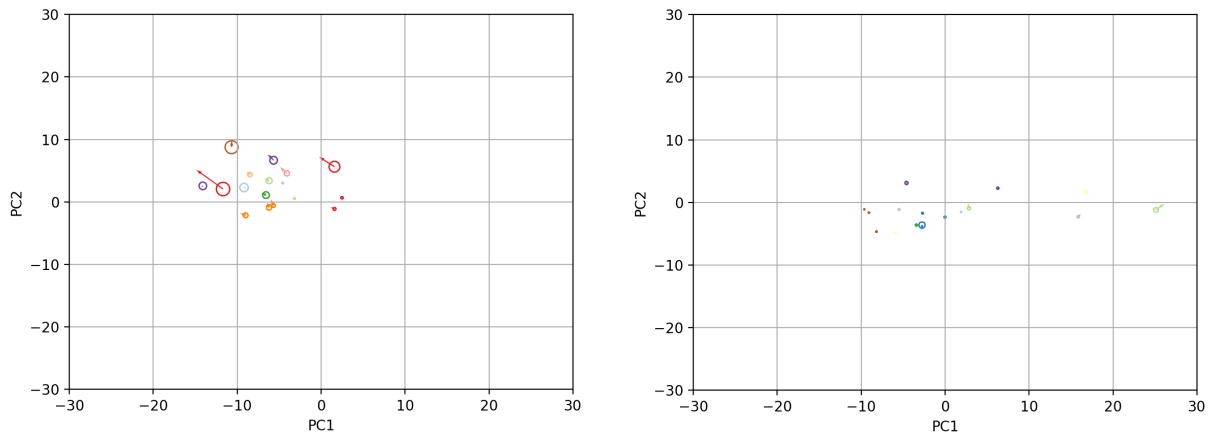


Figure 21. Plots of mean morphology space states and transition vectors of Apoptosis [+] / [-] cells. Plots of the mean space state coordinates and mean transition vectors on a single-cell basis, with Apoptosis[+] cells plotted on the left and Apoptosis[-] cells plotted on the right. Each vector represents a different cell, tracked over a 64h time course. The average $(PC1, PC2)$ coordinate of each cell is found at the origin of each vector. The radius of the circle at the origin of each vector is defined as $2 \times$ the variance of the positional variance of that cell. Smaller radii circle indicate more localized movement of the cell in morphology space, while larger radii circle indicate more extensive movement of that cell in morphology space. Transition vectors were calculated at 4h time intervals such that the origin of each vector is found at $(PC1_{(t)}, PC2_{(t)})$ and the terminus of each vector found at $(PC1_{(t+4h)}, PC2_{(t+4h)})$. Apoptosis[+] cells are characterized by higher positional variance, higher-than-average vector magnitudes, and a directional bias towards $(-30, 30)$. Apoptosis[-] cells are characterized by smaller positional variance and smaller-than-average vector magnitudes. Transition vectors have been scaled down by a factor of 1.5 to facilitate visualization of vectors.

Furthermore, while both classes of cells exhibit significant state occupancy in the central (0, 0) region of PC space, the vector magnitudes of Apoptosis[-] cells were noticeably smaller than those of Apoptosis[+] cells. This suggested the interesting possibility that different cells exhibit different degrees of morphological change even when at similar positions in morphology space, and that these differences in degree of morphological change may correlate directly with divergent behaviors at the cellular level.

To understand the extent of intercellular heterogeneity in transition dynamics, we plotted the mean morphology space coordinate as well as mean transition vector of each cell (Fig. 21). These plots confirmed that, compared to Apoptosis[-] cells, Apoptosis[+] cells exhibited higher variability in their state space coordinates as well as larger vector magnitudes. In contrast, Apoptosis[-] cells exhibited significantly less space state variance and smaller-than-average transition vector magnitudes. Taken together, these three sets of transition vector maps reveal three characteristic differences in the morphology space dynamics of Apoptosis[+] and Apoptosis[-] cells:

- 1) Apoptosis[+] cells exhibit, on average, greater positional variance in WT MEF morphology space when compared to Apoptosis[-] cells, indicating that over the same time interval, Apoptosis[+] cells exhibit a more diverse set of morphologies than Apoptosis[-] cells.
- 2) Apoptosis[+] cells exhibit, on average, transition vectors of larger magnitude than those of Apoptosis[-] cells, indicating that, over the same time interval, Apoptosis[+] cells undergo more dramatic morphological changes.
- 3) As a whole, Apoptosis[+] cells exhibit a directional preference towards the (-30, 30) corner of PC space; Apoptosis[-] cells do not display this directional bias and instead either cluster locally near (0, 0) or exhibit a weak directional bias towards the far right (30, 0) region of PC space.

To develop a deeper understanding of the subspace localization of morphology space dynamics, we binned morphology space into a 10x10 bin array and plotted a series of probability plots (Fig. 22) analogous to those originally developed for analyzing untreated WT MEFs (Chapter 3, pg. 36). These include plots of the probability density function (pdf), probability of entering into a bin (p_{enter}), probability

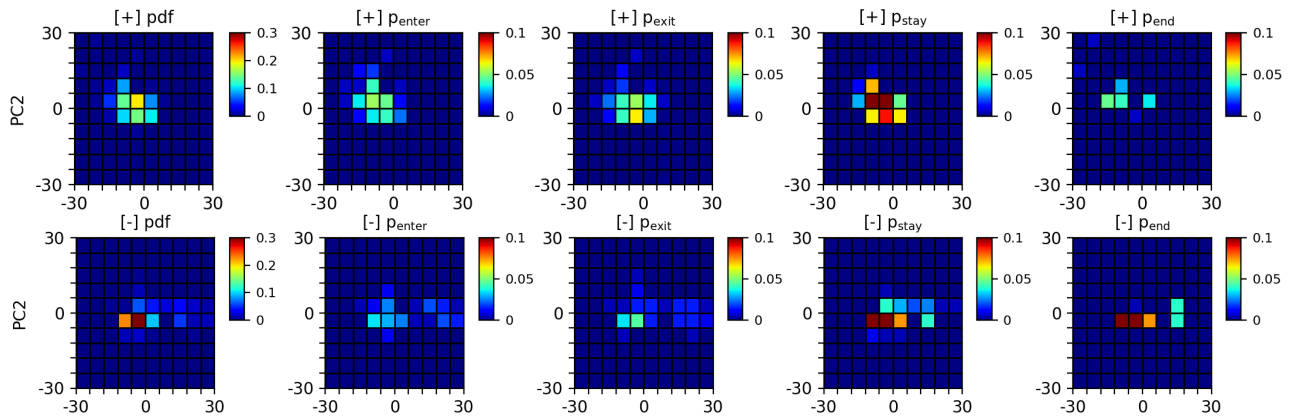


Figure 22. Probability plots of Apoptosis[+]/[-] density functions and transition dynamics. Colored surface plots to visualize various aspects of Apoptosis[+] (top) and Apoptosis[-] (bottom) transition dynamics. Plots of the probability density function (pdf, far left), probability of entering (p_{enter} , near left), probability of exiting (p_{exit} , center), probability of stay in the same bin between time intervals (p_{stay} , near right), and probability of being in the same bin as that occupied at the end of the time course (p_{end} , far right) The ensemble of these probability plots presents a model where Apoptosis[-] cells exhibit a more constrained range of movement within morphology space and are drawn to local space state attractors that act as protective barriers to apoptosis.

of exiting from a bin (p_{exit}), probability of staying within the same bin between adjacent time intervals

(p_{stay}), and probability of being in the same bin as that occupied at the end of the time course (p_{end}).

These plots point to deep underlying differences in the transition dynamics of Apoptosis[+] and Apoptosis[-] cells in morphology space. Plots of the probability density function (pdf, Fig. 22, far left) reveal non-uniform occupancy of morphology space in both Apoptosis[+] and Apoptosis[-] cells, with Apoptosis[-] cells exhibiting more concentrated pockets of non-uniformity relative to Apoptosis[+] cells. Plots of the probabilities of entering (p_{enter} , Fig. 22, near left) and exiting (p_{exit} , Fig. 22, center) indicate that the probabilities of entering and exiting are both higher in Apoptosis[+] cells relative to Apoptosis[-] cells, indicating that Apoptosis[-] cells are less likely to transition between bins during time intervals. A plot of the probability of staying in the same bin between time intervals (p_{stay} , Fig. 22, near right) indicates high rates of short-term occupancy in both Apoptosis[+] and Apoptosis[-] cells, particularly in the central bins near (0, 0) of PC space. However, plots of the probability of a cell being in the same bin as that occupied at the end of the time course (p_{end} , Fig. 22, far right) indicate that Apoptosis[-] cells also exhibit long-term occupancy of this space, whereas Apoptosis[+] cells do not. These probability plots lead us to a model in which Apoptosis[-] cells are less motile within morphology space and are drawn to energetically favorable state space attractor(s), entry into which often results in long-term occupancy. To test whether

these probability plots differ significantly from their WT counterparts, we ran a series of Kolmogorov-Smirnov tests, which incorporate the spatial organization of data and allow us to run significance tests on two-dimensional datasets. The Kolmogorov-Smirnov test calculates the supremum, or largest absolute value, between two x-axis aligned points of the cumulative probability distribution (Fig. 23). By summing the cumulative probability distribution in a consistent way across the 10x10 bin probability plots, we preserve the spatial orientation of the datasets, allowing us to run two-sample Kolmogorov-Smirnov significance tests between analogous probability plots. The Kolmogorov-Smirnov statistic is calculated as follows:

$$D_{n,m} = \sup |F_{1,n}(x) - F_{2,m}(x)| \quad (\text{Eq. 17})$$

where $D_{n,m}$ is the Kolmogorov-Smirnov statistic, \sup is the supremum function, and $F_{1,n}$ and $F_{2,m}$ are the cumulative distribution functions of the two samples being compared. We reject the null hypothesis that the two samples are not significantly different if:

$$D_{n,m} > c(\alpha) \sqrt{\frac{n+m}{nm}} \quad (\text{Eq. 18})$$

where n and m are the sizes of the two samples being compared, and $c(\alpha)$ is defined as

$$c(\alpha) = \sqrt{-\frac{1}{2} \ln \left(\frac{\alpha}{2} \right)} \quad (\text{Eq. 19})$$

where α is the user-defined statistical significance level.

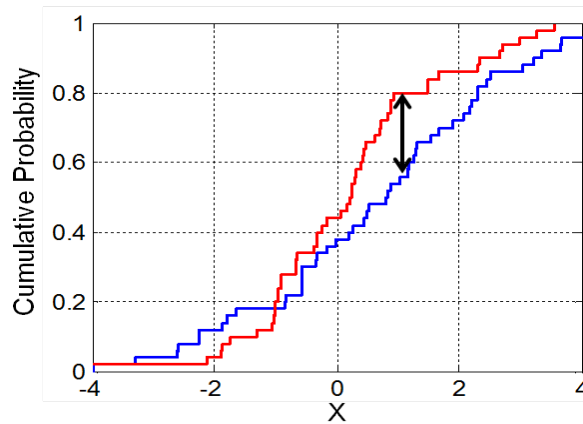


Figure 23. Example two-sample Kolmogorov-Smirnov significance test. The cumulative probability distribution functions of two sample datasets are depicted in red and blue, respectively. The black double-headed arrow identifies the x-axis aligned points at which the two cumulative probability distribution functions differ the most, otherwise known as the supremum. This value is considered the Kolmogorov-Smirnov statistic value.

The statistic values were calculated for various Kolmogorov-Smirnov significance tests run across two-sample permutations of untreated WT, Apoptosis[+], and Apoptosis[-] cells. Bar plots of these values are shown in (Fig. 24). These plots revealed that both Apoptosis[+] and Apoptosis[-] cells differ significantly from untreated WT cells in their pdf, p_{enter} , p_{exit} , p_{stay} , and p_{end} , statistically confirming our observations of altered transition dynamics of morphology space in response to camptothecin induction. A comparison of the probability plots of Apoptosis[+] and Apoptosis[-] cells revealed statistically significant differences in their p_{enter} , p_{exit} , and p_{end} , but a lack of statistically significant differences in their pdf and p_{stay} . These results are in agreement with earlier observations and lend themselves to a model in which Apoptosis[+] and Apoptosis[-] cells are dynamically different in WT MEF morphology space and that this dynamical variability correlates directly with functional heterogeneity at the population level.

The results of the probability maps, coupled with the transition vector maps, convincingly illustrate clear differences in the dynamic behavior of Apoptosis[+] and Apoptosis[-] cells in WT MEF morphology space. To develop a more nuanced understanding of the changes to morphology space that underlie the observed functional divergence, we again turned to statistical mechanical theory to construct an energy landscape underlying camptothecin-treated WT MEF morphology space.

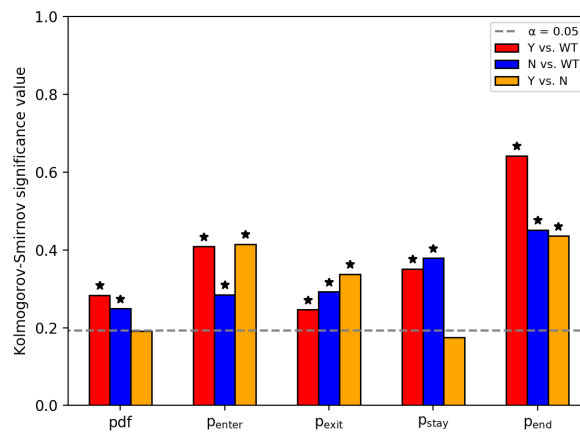


Figure 24. Camptothecin produces significant changes in transition probability plots. Two-sample Kolmogorov-Smirnov significance tests were used to compare probability plots between untreated WT, Apoptosis[+], and Apoptosis[-] cells. Asterisks indicate significance values above $\alpha = 0.05$. Untreated WT and Apoptosis[+] cells (red bars) differed significantly in their pdf, p_{enter} , p_{exit} , p_{stay} , and p_{end} . Untreated WT and Apoptosis[-] cells (blue bars) differed significantly in their pdf, p_{enter} , p_{exit} , p_{stay} , and p_{end} . Apoptosis[+] and Apoptosis[-] cells (orange bars) differed significantly in their p_{enter} , p_{exit} , and p_{end} , and did not differ significantly in their pdf and p_{stay} .

4d. Camptothecin Creates Local State Space Attractors

As previously described, the Boltzmann distribution describes the occupancy of an energy state as a function of the temperature and available energy states of the system. We can calculate values for these first two variables from our experimental data, with the energy state occupancy represented by the probability density function, and the temperature calculated by abstracting transition vector magnitudes in morphology space as “speeds” of particles in a two-dimensional plane.

A comparison of the transition vectors of camptothecin-treated versus untreated WT MEFs indicated that camptothecin induction produced a 36% decrease in the average magnitude of transition vectors in morphology space. To understand if this reduction in magnitude was constrained to specific subspaces, or occurred more generally across morphology space, we plotted a colored surface plot of the bin-by-bin mean transition vector magnitude of a 60x60 bin array of PC space (Fig. 25), revealing that camptothecin induction produces a near-universal decrease in the average magnitude of transition vectors across WT MEF morphology space.

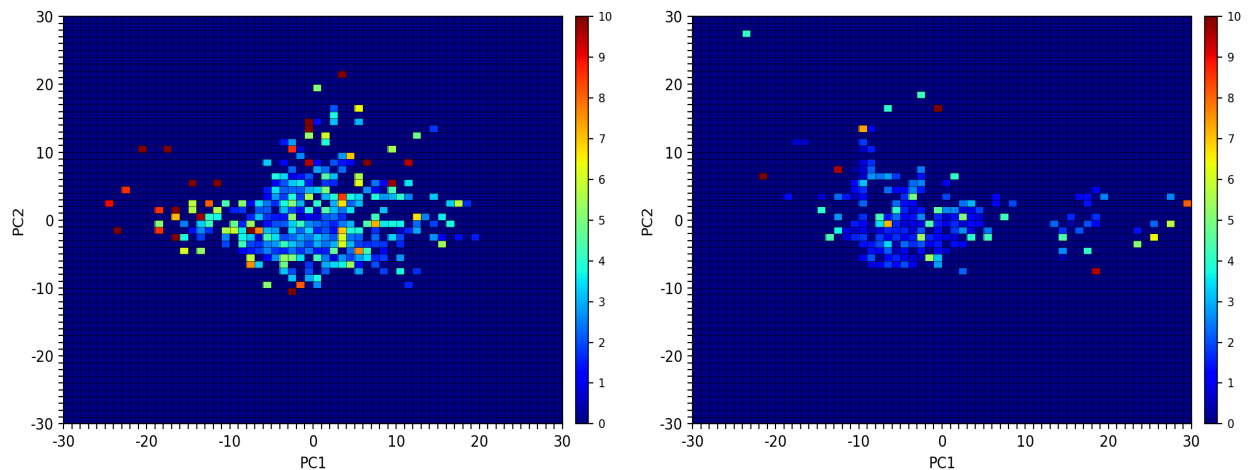


Figure 25. Camptothecin induction decreases the average transition vector magnitude of WT MEFs. The average magnitude of transition vectors of untreated (left) vs. camptothecin-treated (right) WT MEFs are plotted as colored surface plots on a bin-by-bin basis in the morphology space defined by PC1 vs. PC2, binned into a 60x60 bin array. Transition vectors were calculated at 4h time intervals such that the origin of each vector is found at $(PC1_{(t)}, PC2_{(t)})$ and the terminus of each vector found at $(PC1_{(t+4h)}, PC2_{(t+4h)})$. These colored surface plot reveal that camptothecin induction produces a near-universal decrease in the average transition vector magnitude of cells in WT MEF morphology space.

In the context of our adaptation of the Boltzmann distribution, a decrease in the mean transition vector magnitude indicates a decrease in the effective temperature of morphology space, signaling a “cooling” of the system. The temperature of a system is an important variable in the Boltzmann distribution, as it directly influences the predicted occupancies of available energy states. We earlier demonstrated that camptothecin induction produces statistically significant changes to the probability density function in morphology space; however, it was unclear whether these changes were entirely due to the decrease in effective temperature, or if there had been a concomitant change to the underlying energy landscape of WT MEF morphology space.

To address this question, we used our adaptation of the Boltzmann distribution (Eq. 10) to calculate the probability density function expected from occupation of our previously calculated untreated WT MEF energy landscape over a range of temperatures. We then ran a series of two-sample Kolmogorov-Smirnov (K-S) significance tests to compare these expected probability density functions to that observed experimentally in response to camptothecin induction. We plotted the K-S statistic values as a function of temperature (Fig. 26), where small K-S values indicate high similarity between datasets, and large K-S values indicate low similarity between datasets. Our plot indicated that maximum similarity at an effective temperature of $1.04 T_{WT}$, where T_{WT} is the effective temperature of untreated WT MEF morphology space. Our experimental data, however, indicated that camptothecin-treated morphology

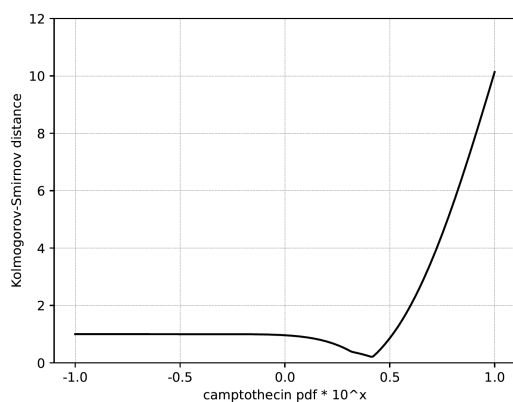


Figure 26. Statistic values for Kolmogorov-Smirnov tests of camptothecin-treated cells. Plot of the Kolmogorov-Smirnov statistic value (y-axis) as a function of the temperature of the system. The minimum occurs at $T = 1.04T_{WT}$, whereas the observed effective temperature is $0.41T_{WT}$, indicating a concomitant change in the underlying energy landscape of morphology space.

space was characterized by an effective temperature of $0.41 T_{WT}$. These results suggest that the change in effective temperature alone was not sufficient to explain the observed change in morphology space occupancy and that the change in effective temperature had been accompanied by a concomitant change in the energy landscape underlying morphology space.

Using the theoretical framework developed to construct an energy landscape of untreated WT MEF morphology space (Chapter 3, pg. 36-39), we used the new effective temperature of $0.41 T_{WT}$, coupled with the observed probability density function, to calculate an energy landscape describing WT MEF morphology space occupancy under $2\mu\text{M}$ camptothecin induction (Fig. 27). This plot revealed several significant changes to the energy landscape. While the untreated energy landscape was characterized by a single global minimum, the camptothecin-treated energy landscape instead expressed several local minima. These appeared in the upper left $(-30, 30)$ as well as far right $(30, 0)$ corners of PC space and were accompanied by a deep minimum in the central $(0, 0)$ region of PC space.

To better compare the untreated and camptothecin-treated energy landscapes, we plotted the relative differences between the two landscapes ($E_{\text{camptothecin}} - E_{\text{untreated}}$) (Fig. 28). This plot revealed that, within the same morphology space state, camptothecin-treated cells occupied a lower energy level than

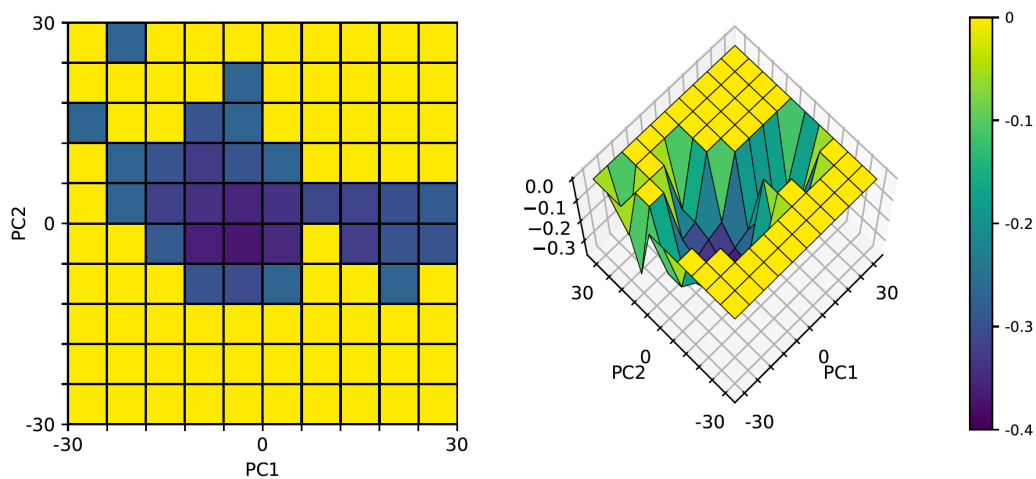


Figure 27. Plot of the effective energy landscape of camptothecin WT MEF morphology space. Colored surface plot of the calculated effective energy landscape of WT MEF morphology space under $2\mu\text{M}$ camptothecin induction. The landscape was calculated using the Boltzmann distribution by abstracting transition vectors as velocity vectors and calculating an effective temperature. A plot of the effective energy landscape reveals local minima in the upper left $(-30, 30)$, far right $(30, 0)$, and central $(0, 0)$ regions of PC space. All energy values were shifted down by $0.4 \cdot 10^{-19}$ (plotted energy = calculated energy - $0.4 \cdot 10^{-19}$) to facilitate visualization of the energy landscape.

their untreated counterparts, indicating a relative increase in energetic favorability. This is in agreement with the observed decrease in mean transition vector magnitude under camptothecin induction. This plot additionally reveals that camptothecin induction produces a mild deepening of the energy landscape in the central region (0, 0) of PC space, as well as more dramatic deepening in the far left (-30, 0) and far right (30, 0) regions. Though the original plot of the camptothecin-treated energy landscape (Fig. 27) revealed a local minimum in the upper left corner (-30, 30) of PC space, this does not appear in the differential plot, as only bins for which information was available for both the treated and untreated energy landscapes were included. This decision was made to avoid misleading representation of differentials resulting solely from a lack of data in specific subspaces.

Camptothecin induction effectively shifted the energy landscape of WT MEF morphology space from one characterized by a single global minimum to one characterized by several local minima. Given the hypothesized relationship between morphological and functional heterogeneity, we wanted to investigate whether the appearance of these new minima coincided with the observed functional heterogeneity of Apoptosis[+] and Apoptosis[-] cells. To do this, we separately calculated an effective temperature and energy landscape for each class and plotted the differentials between their energy landscapes and that of untreated WT MEFs.

The differential plot of the Apoptosis[+] and untreated energy landscapes ($E_{\text{Apoptosis}[+]} - E_{\text{untreated}}$) (Fig. 29) revealed that the energetics of Apoptosis[+] cells differed significantly from those of untreated cells in only one subspace, located in the far/upper left (-30, 10-30) corner of PC space. Since Apoptosis[+] cells are defined as cells that underwent apoptosis over the course of the 64h time lapse, we hypothesized that this energy minimum acts as a local space state attractor that functions to induce and/or facilitate apoptosis. In contrast, the differential plot of the Apoptosis[-] and untreated energy landscapes ($E_{\text{Apoptosis}[-]} - E_{\text{untreated}}$) (Fig. 30) did not exhibit the same local energy differential in the far/upper left corner of PC space. Instead, it indicated two new energy minimizations in Apoptosis[-] morphology space: one in the far right (30, 0) region of PC space, and a second, milder minimization in the central region (0, 0) of PC space, coinciding with the global energy minima observed in the untreated energy

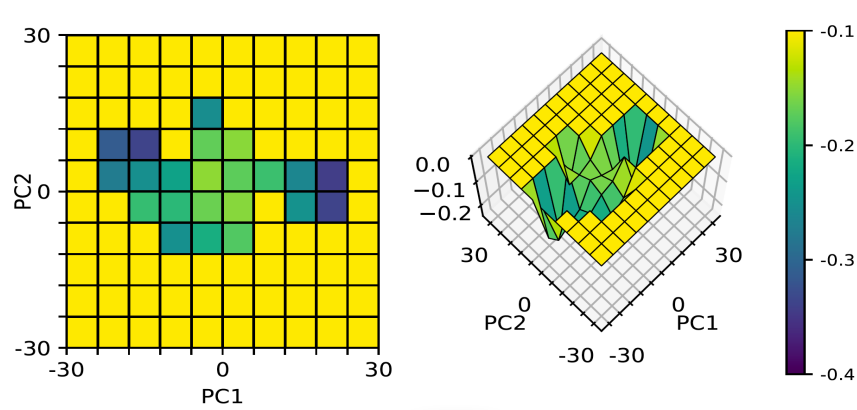


Figure 28. Plot of the differential between camptothecin and untreated energy landscapes. Colored surface plot of WT MEF (camptothecin energy landscape – untreated energy landscape). Plot indicates deepening of the original global minima as well as the appearance of new local minima in PC space.

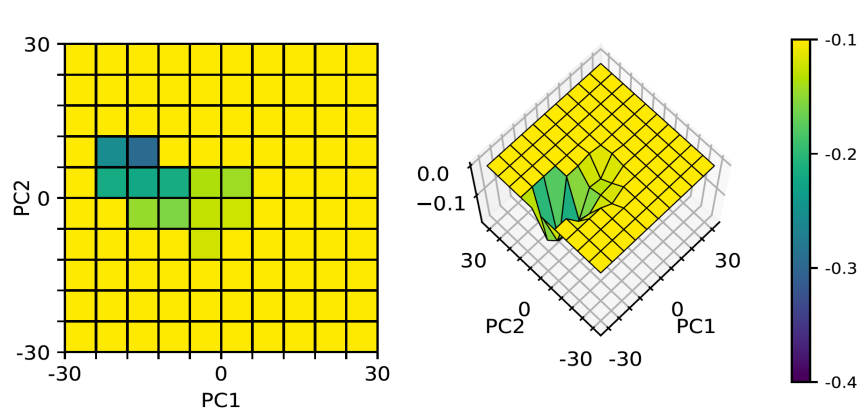


Figure 29. Plot of the differential between Apoptosis[+] and untreated energy landscapes. Colored surface plot of WT MEF (Apoptosis[+] energy landscape – untreated energy landscape). Plot indicates the appearance of a new local minimum in the far/upper left corner (-30, 30) of PC space.

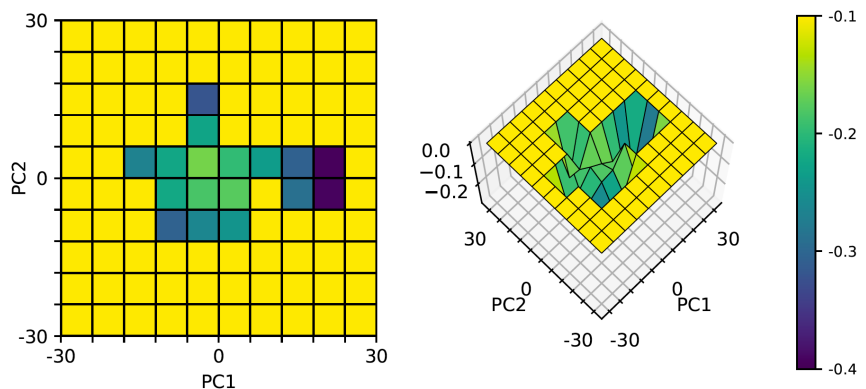


Figure 30. Plot of the differential between Apoptosis[-] and untreated energy landscapes. Colored surface plot of WT MEF (Apoptosis[-] energy landscape – untreated energy landscape). Plot indicates deepening of the original global minima near (0, 0), as well as the appearance of a new local minimum in the far right (30, 0) of PC space.

landscape. Several important insights can be garnered from this plot. First, the dramatic deepening of the far right (30, 0) region suggests that camptothecin induction produces an energetically favorable subspace from which exit may be energetically prohibitive. This hypothesis is supported by the earlier plot of bin-by-bin average transition vectors (Fig. 20), which revealed large-magnitude vectors entering this space, but minimal to no vectors leaving this space. Furthermore, since this energy minima appears exclusively in Apoptosis[-] cells, which are defined as cells that did not undergo apoptosis over the course of the 64h time lapse, we hypothesized that this subspace acts as an energetically favorable state space attractor that functions as a protective barrier to apoptosis, preventing cells from transitioning to the state space attractor in the upper left (-30, 10-30) corner associated with cellular apoptosis.

The second energy minimization observed in Apoptosis[-] cells occurred in the central (0, 0) region of PC space. Interestingly, both Apoptosis[+] and Apoptosis[-] cells exhibit occupancy in this region, suggesting that this subspace is not characterized by the all-or-none properties hypothesized for the two previously discussed energy minima. An examination of the transition vector maps (Fig. 19, Fig. 20) revealed that vectors both enter and exit from this subspace, suggesting that, though energetically favorable, entry into this subspace is non-binding and exit from this subspace is not energetically prohibited. This leads to our hypothesis that this region functions as an “intermediate” subspace, both spatially and functionally, that confers partial, but non-absolute, protection against apoptosis.

To test our hypothesis regarding the functional importance of each of these energy minima, we generated a heat map of the probability of undergoing apoptosis given the space state of a cell (Fig. 31). This plot strongly supports our interpretation of the functional equivalence of the three aforementioned subspaces of WT MEF morphology space:

- 1) a subspace in the far/upper left (-30, 10-30) of PC space functions as an apoptotic “death” well that induces and/or facilitates cellular apoptosis; occupancy of this well carries a 100% probability of apoptosis;
- 2) a subspace in the far right (30, 0) of PC space that functions as a protective barrier against apoptosis; occupancy into this well carries a 100% probability of survival;

3) a central subspace in the (0, 0) region of PC space functions as a moderately protective barrier against apoptosis; occupancy of this space confers partial, but non-absolute, protection against apoptosis.

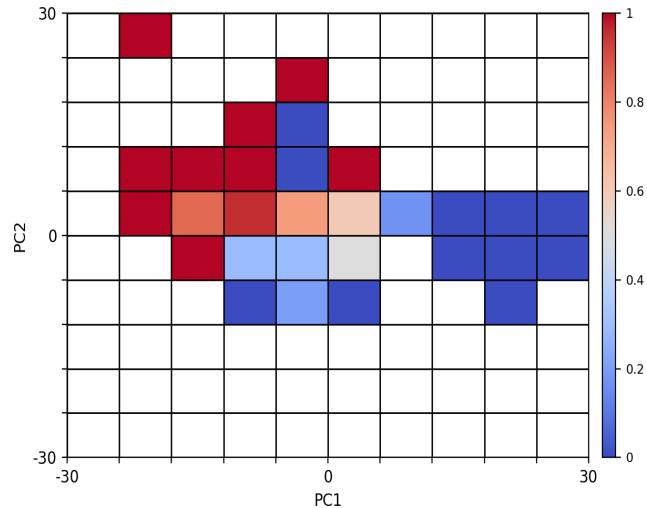


Figure 31. Heat map of apoptosis probability as a function of morphology space state. The probability of a cell undergoing apoptosis is represented along the color bar, with deep blue corresponding to a 0% probability of apoptosis and deep red corresponding to a 100% probability of apoptosis. Probabilities of apoptosis were calculated by summing the morphology space states of all cells across the 64h time course and calculating the probability of apoptosis given occupancy in a space state at any point in time.

4e. Results and Interpretation

These results produce several important insights into the effects of camptothecin induction on the topology and dynamics of morphology space. We show here that apoptotic induction of WT MEFs under 2 μ M camptothecin produces a decrease in the mean magnitude of transition vectors in morphology space. Biologically speaking, this means that, over the same time interval, cells under camptothecin induction undergo less extensive morphological changes compared to their untreated counterparts, providing strong evidence that exogenous inputs can directly influence the morphological behavior of cells. It may be of interest in the future to determine the mechanism(s) responsible for the observed dampening of morphological transitions, as well as to identify additional exogenous inputs capable of either increasing or decreasing the speed of morphological transitions.

Perhaps the most important result of this chapter is the observation of a clear correlative relationship between morphological and functional heterogeneity. We demonstrate here that camptothecin

induction fundamentally shifts the energy landscape underlying morphology space from one characterized by a single global minimum to one characterized by several local minima. These energy minima facilitate functional heterogeneity by acting as local state space attractors, producing spatially isolated subspaces within morphology space that attract separate subsets of cells within the population. We find that each subspace is correlated with varying degrees of apoptotic potential, providing a working model for the observed non-uniform apoptotic response of an isogenic population.

CHAPTER 5. Conclusion and Future Directions

In this work we present a framework for investigating the topology and dynamics of morphological heterogeneity in isogenic populations. We discover several important principles of morphological heterogeneity, namely that it is driven by the non-uniform energetics of morphology space and that the parameters of morphological heterogeneity can be fundamentally altered upon drug induction. These alterations facilitate functional heterogeneity within an isogenic population, providing the first body of evidence for morphological heterogeneity as an important and functionally consequential form of non-genetic heterogeneity.

The first part of this work consisted of developing a framework for the quantification of morphological heterogeneity in isogenic populations. Accordingly, we developed a set of molecular biology, feature extraction, and statistical analysis tools to accurately capture high-dimensional feature sets across a large number of cells and dimensionally reduce this dataset into an interpretable representation of morphology space. We demonstrated that this approach is capable of capturing morphological heterogeneity within isogenic populations and, more specifically, that WT MEFs occupy a heterogeneous and largely continuous region of morphology space rather than clustering into discrete subspaces.

To better understand the dynamics underlying morphology space, we developed methods for imaging morphological structures in live cells. We designed and engineered a plasmid for lentivirus-based delivery of a 3-Reporter cassette encoding fluorescent reporters targeted to the microtubule cytoskeleton, nucleus, and mitochondria. This approach allowed us to simultaneously visualize multiple morphological structures of interest in live cells. We imaged 3-Reporter transduced WT MEFs over a 60h time course and developed transition vector maps to visualize morphological changes. This work produced several important insights into the dynamics underlying morphological space in WT MEFs. First, morphological transitions cannot be described by a deterministic process, as indicated by a lack of closed flux loops within the transition vector map. Secondly, transition vector magnitudes are non-uniform across

morphology space, with central space states displaying, on average, smaller-magnitude transition vectors than more peripherally located space states. These findings illustrate non-uniformity in the dynamics underlying morphology space and indicate that, within the same time interval, the degree of morphological changes varies as a function of the starting morphological state of a cell.

To develop a more quantitative understanding of these dynamics, we adapted concepts from statistical mechanical theory that allowed us to use transition vector magnitudes and probability density functions derived from experimental data to construct a map of the effective energy landscape underlying WT MEF morphology space. We discovered that this energy landscape is characterized by a single global minimum, indicating dynamical heterogeneity in morphology space, with some morphological states being more energetically favorable than others. Hypothesizing that the observed morphological heterogeneity might correlate with functional heterogeneity at the population level, we screened a panel of apoptosis inducers for conditions producing a heterogeneous response in WT MEFs. We identified camptothecin as a promising candidate and tracked and quantified the morphological behavior of WT MEFs under camptothecin induction, discovering several interesting effects of drug induction on morphology space. First, camptothecin induction slowed the rate of morphological transitions by approximately 36%, indicating that, over the same time interval camptothecin-treated cells exhibited morphological changes that were 36% less extensive than those exhibited by untreated cells. Perhaps most interestingly, we showed that drug exposure can fundamentally alter the energetics of morphology space, shifting the energy landscape from one characterized by a single global minimum to one characterized by several local minima. Furthermore, these nascent energy minima correlated directly with divergent functional responses to apoptotic induction, suggesting that localized changes to the topology of morphology space might serve as a mechanism for producing functional heterogeneity within isogenic populations.

Here we present, to our knowledge, the first body of evidence establishing a relationship between native morphological heterogeneity in isogenic populations and functionally divergent behavior. Whether this link is correlative or causative remains to be explored, but this work suggests that morphological

heterogeneity may function as a facilitator of functional heterogeneity in isogenic populations. As a result, we make the case for further studies of morphological heterogeneity, as it holds the potential to reveal fundamental insights into the nature of non-genetic heterogeneities in biological systems.

The results of this study set the groundwork for many additional lines of inquiry into morphological heterogeneity in isogenic populations. Morphology exists at an intermediate scale between the molecular microstate and physiological behavior of cells and there remain many questions at both ends of this spectrum. At the molecular scale, we are particularly interested in developing our understanding of factors that contribute to the establishment and control of morphological heterogeneity. In theory, there may be “noise-controlling” factors that influence the type and extent of morphological heterogeneity within a population. Through the development of more high-throughput and automated imaging and feature analysis approaches, we will be able to screen for both endogenous and exogenous factors capable of controlling or altering the topology of morphology space.

Numerous studies over the years have identified noise in gene expression as a fundamental contributor to functional heterogeneity within isogenic populations. This study presents clear evidence that morphological heterogeneity may be similarly consequential. In particular, it will be important to establish whether morphological heterogeneity arises as a strict function of transcriptional and/or epigenetic heterogeneity, or if there are additional layers of “noise” at the morphological scale. If one abstracts a molecule as a bipolar magnetic bar, one can imagine that if a collection of such bars were repeatedly tossed together, they would fall into a variety of spatial arrangements despite the type and number of starting materials being identical. Similarly, identical numbers and types of molecules could, in theory, produce morphologically variable structures, which themselves may exhibit functional variability. By this mechanism, morphological “noise” would be another non-genetic source of functional heterogeneity on top of that engendered by molecular “noise.” Additionally, there are many functional factors beyond mRNA and proteins (e.g. siRNAs, lncRNAs, microRNAs, protein modifications, etc.) that, in theory, could contribute to the determination of morphological structures. A clearer understanding

of the relationship between molecular microstate and morphology will help us better understand the validity and utility of morphology as a coarse-grain proxy for the molecular state of a cell.

In this study we demonstrate a relationship between heterogeneity in morphology space dynamics and functional heterogeneity at the population level. In particular, we observe specific subspaces of WT MEF morphology space that are associated with either increased or decreased sensitivity to apoptotic induction. An important next step in this work is to understand the generalizability of these findings. In other words, if we functionalize WT MEFs to be either more or less sensitive to apoptotic induction, how would their occupancy of morphology space change and would they natively adapt more locally constrained subspaces of morphology space? One could, for example, create a line of p53 KO MEFs and map out their probability density function in WT MEF morphology space, under the hypothesis that a more apoptotic-resistant variant of WT MEFs may natively occupy those subspaces associated with decreased sensitivity to apoptotic induction. If proven true, this would point to a deeper underlying relationship between morphology and function than the correlative relationship demonstrated thus far.

Finally, this study develops a framework that allows for further investigation of causative and functional properties of morphological changes observed in numerous disease states. If established that there truly is a 1:1 correlation between morphology and function, we would, in theory, be able to use the more easily-accessible parameter of morphology to assess the internal microstate of a cell. For example, physicians may be able to use morphology-based tools to more accurately screen and diagnose for diseases, or to monitor disease progression and therapeutic response. It remains to be established the fidelity of morphology as a functional indicator, understanding that this may vary as a function of cell type, morphological structure, and/or disease state. Additionally, if determined that morphology in and of itself is not a sufficient indicator of the functional state of a cell, it may still be useful when coupled with other cellular assays (e.g. adhesion assays, substrate stiffness assays, growth assay, etc.) to develop a complete picture of the functional state of a cell. This study serves to position morphology as a potentially useful clinical tool that merits further investigation.

We present here the first body of work, to our knowledge, that demonstrates that heterogeneities in the topology and dynamics of morphology space correlate directly with functional heterogeneity in an isogenic population. These results position morphological heterogeneity as a potentially important novel mode of non-genetic heterogeneity, sister to the more widely studied forms of transcriptional and epigenetic heterogeneity. We hope that, in future years, morphology and statistical analysis tools will continue to be developed and a more precise and wide-ranging understanding of the sources and consequences of morphological heterogeneity in isogenic populations established. By illuminating the principles intertwining the molecular microstate, morphology, and function, of a cell, we hope that this work will contribute to a deeper understanding of the fundamental building block of all living organisms.

REFERENCES

- Alirol E and Martinou JC. Mitochondria and cancer: is there a morphological connection? *Oncogene*. **25**: 4706-16; doi: 10.1038/sj.onc.1209600
- Aung-Htut MT, Lam YT, Lim Y-L, Rinnerthaler M, Gelling CL, Yang H, Breitenbach M, Dawes IW. (2013). Maintenance of mitochondrial morphology by autophagy and its role in high glucose effects on chronological lifespan of *Saccharomyces cerevisiae*. *Oxidative Medicine and Cellular Longevity*. **2013**(636287); doi: 10.1155/2013/636287
- Bigger JW. (1944). Treatment of staphylococcal infections with penicillin by intermittent sterilization. *Lancet*. **244**: 497-500; doi: 10.1017/S0140-6736(00)74210-3
- Cataldo AM, McPhie DL, Lange NT, Punzell S, Elmiligy S, Ye NZ, Froimowitz MP, Hassinger LC, Menesale EB, Sargent LW, Logan DJ, Carpenter AE, Cohen BM. (2010). Abnormalities in mitochondrial structure in cells from patients with bipolar disorder. *American Journal of Pathology*. **177**(2): 575-85. doi: 10.2353/ajpath.2010.081068
- Chang HH, Hemberg M, Barahona M, Ingber DE, Huang S. (2008). Transcriptome-wide noise controls lineage choice in mammalian progenitor cells. **453**(7194), 544-47; doi: 10.1038/nature06965
- Chen A, Beetham H, Black MA, Priya R, Telford BJ, Guest J, Wiggins GAR, Godwin TD, Yap AS, Guilford PJ. (2014). E-cadherin loss alters cytoskeletal organization and adhesion in non-malignant breast cells but is insufficient to induce an epithelial-mesenchymal transition. *BMC Cancer*. **14**, 552; doi: 10.1186/1471-2407-14-552
- Chen H, Detmer SA, Ewald AJ, Griffin EE, Fraser SE, Chan DC. (2003). Mitofusins Mfn1 and Mfn2 coordinately regulate mitochondrial fusion and are essential for embryonic development. *Journal of Cell Biology*. **160**, 189-200; doi: 10.1083/jcb.200211046
- Chen H, Chomyn A, Chan DC. (2005). Disruption of fusion results in mitochondrial heterogeneity and dysfunction. *Journal of Biological Chemistry*. **280**, 26185-192; doi: 10.1074/jbc.M503062200
- Collins TJ, Berridge MJ, Lipp P, Bootman MD. (2002). Mitochondria are morphologically and functionally heterogeneous within cells. **21**, 1616-1627; doi: 10.1093/emboj/21.7.1616
- Friedman JR, Lackner LL, West M, DiBenedetto JR, Nunnari J, Voeltz GK. (2011). ER tubules mark sites of mitochondrial division. *Science*. **334**: 358-62; doi: 10.1126/science.1207385
- Iannetti EF, Willems PH, Pellegrini M, Beyrath J, Smeitink JA, Blanchet L, Koopman WJ. (2015). Toward high-content screening of mitochondrial morphology and membrane potential in living cells. *The International Journal of Biochemistry and Cell Biology*. **63**, 66-70; doi: 10.1016/j.biocel.2015.01.020
- Levinthal C. (1969). How to fold graciously. *Mossbauer Spectroscopy in Biological Systems Proceedings*. **67**(41): 22-26.
- Locey KJ and Lennon JT. (2016). Scaling laws predict global microbial diversity. *Proceedings of the National Academy of Sciences*. **113**(21), 5970-75; doi: 10.1073/pnas.1521291113

Kim JH, Lee S-R, Li L-H, Park H-J, Park J-H, Lee KY, Kim M-K, Shin BA, Choi S-Y. (2011). High cleavage efficiency of a 2A peptide derived from porcine teschovirus-1 in human cell lines, zebrafish, and mice. *PLoS ONE*. **6**(4): e18556; doi: 10.1371/journal.pone.0018556

Maamar H, Raj A, Dubnau D. (2007). Noise in gene expression determines cell fate in *Bacillus subtilis*. **317**(5837): 526-29; doi: 10.1126/science.1140818

Scaffidi P, Gordon L, Misteli T. (2005). The cell nucleus and aging: tantalizing clues and hopeful promises. *PLoS Biology* **3**(11): e395; doi: 10.1371/journal.pbio.0030395

Shah D, Zhang Z, Khodursky AB, Kaldalu N, Kurg K, Lewis K. (2006). Persisters: a distinct physiological state of *E.coli*. *BMC Microbiology*. **6**, 53; doi: 10.1186/1471/2180/6/53.

Suen DF, Norris KL, Youle RJ. Mitochondrial dynamics and apoptosis. (2008). *Genes & Development*. **22**(12), 1577-1590; doi: 10.1101/gad.1658508

Tabrizi SJ, Cleeter MW, Xuereb J, Taanman JW, Cooper JM, Schapira AH. (1999). Biochemical abnormalities and excitotoxicity in Huntington's disease brain. *Annals of Neurology*. **45**, 25-32.

Trimmer PA, Swerdlow RH, Parks JK, Keeney P, Bennett Jr. JP, Miller SW, Davis RE, Davis Parker Jr. W. (2000) Abnormal mitochondrial morphology in sporadic Parkinson's and Alzheimer's disease cybrid cell lines. *Experimental Neurology*, **162**(1): 37-50. doi: 10.1006/exnr.2000.7333

Vilariño N, Nicolaou KC, Frederick MO, Cagide E, Ares IR, Louzao C, Vieytes MR, Botana LM. (2006). Cell growth inhibition and actin cytoskeleton disorganization induced by azaspiracid-1 structure-activity studies. *Chemical Research in Toxicology*. **19**(11), 1459-1466; doi: 10.1021/tx060131z

Walker FO. (2007). Huntington's disease. *Lancet*. **369**(9557), 218-228; doi: 10.1016/S0140-6736(07)60111-1

Wang H, Lim PJ, Karbowski M, Monteiro M. (2009). Effects of overexpression of huntingtin proteins on mitochondrial integrity. *Human Molecular Genetics*. **18**, 737-52; doi: 10.1093/hmg/ddn404

Wang X, Su B, Zheng L, Perry G, Smith MA, Zhu X. (2009). The role of abnormal mitochondrial dynamics in the pathogenesis of Alzheimer's Disease. *The Journal of Neurochemistry*. **109**(1): 153-59. doi: 10.1111/j.1471-4159.2009.05867.x

Wiemerslage L, Ismael S, Lee D. (2016). Early alterations of mitochondrial morphology in dopaminergic neurons from Parkinson's disease-like pathology and time-dependent neuroprotection with D2 receptor activation. *Mitochondrion*. **30**: 138-47; doi: 10.1016/j.mito.2016.07.004

Yu D, Baird MA, Allen JR, Howe ES, Klassen MP, Reade A, Makhijani K, Song Y, Liu S, Murthy Z, Zhang S-Q, Weiner OD, Kornberg TB, Jan Y-N, Davidson MW, Shu X. (2015). A naturally monomeric infrared fluorescent protein for protein labeling *in vivo*. *Nature Methods*. **12**: 763-65; doi: 10.1038/nmeth.3447

APPENDIX

Principal Component 1; variance explained = 23.4%

Feature Name	Feature Type	Loading
CellMeanCentroidDist	Cell morphometry	0.1324
CellConvexPerimeter	Cell morphometry	0.1321
NucEquivDiameterArea	Nucleus morphometry	0.1307
CellEquivDiameterArea	Cell morphometry	0.1305
CellLowSmoothPerimeter	Cell morphometry	0.1296
NucMeanCentroidDist	Nucleus morphometry	0.1295
CellPerimeter	Cell morphometry	0.1292
CellEquivDiameterPerim	Cell morphometry	0.1292
CellHighSmoothPerimeter	Cell morphometry	0.1290

Principal Component 2; variance explained = 11.8%

Feature Name	Feature Type	Loading
NucMinContrast	Nucleus texture	0.1583
CellMinContrast	Cell texture	0.1563
CellMeanContrast	Cell texture	0.1551
CellMeanHomogeneity	Cell texture	-0.1538
CellMaxHomogeneity	Cell texture	-0.1530
CellMeanCorrelation	Cell texture	-0.1529
CellMaxCorrelation	Cell texture	-0.1526
CellMinHomogeneity	Cell texture	-0.1524
CellMinCorrelation	Cell texture	-0.1519
NucMaxHomogeneity	Nucleus texture	-0.1515

Principal Component 3; variance explained = 8.6%

Feature Name	Feature Type	Loading
NucCVDisc3	Nucleus texture	0.1919
NucCVDisc4	Nucleus texture	0.1902
NucCVCentroidDist	Nucleus morphometry	0.1825
NucFracTotalDisc1	Nucleus texture	0.1786
NucVarDisc3	Nucleus texture	0.1745
NucRatioMajorMinor	Nucleus morphometry	0.1741
NucCircularity	Nucleus morphometry	-0.1726
NucCVDisc2	Nucleus texture	0.1693
NucFracTotalDisc2	Nucleus texture	0.1658
NucVarDisc2	Nucleus texture	0.1652

Table A1. Dominant loadings of the first three Principal Components of live WT MEFs. The top 10 loadings of the first three principal components of a 205-feature set analysis of WT MEF morphology. Principal Component 1 captures 23.4% of total variance and is dominated by cell and nucleus morphometric features. Principal Component 2 captures 11.8% of total variance and is dominated by cell and nucleus textural features. Principal Component 3 captures 8.6% of total variance and is dominated by nucleus morphometric and textural features. Mitochondrial features do not factor heavily into the first three Principal Components.

Feature Name	Feature Type	PC1 (fixed)	PC2 (fixed)	PC3 (fixed)
CellArea	Cell morphometry	0.1025	-0.0494	-0.0633
CellConvexArea	Cell morphometry	0.0995	-0.0786	-0.0426
CellEccentricity	Cell morphometry	-0.0350	-0.0841	0.1133
CellEquivDiameterArea	Cell morphometry	0.1185	-0.0230	-0.0359
CellMajorAxisLength	Cell morphometry	0.0971	-0.0946	0.0498
CellMinorAxisLength	Cell morphometry	0.1126	-0.0122	-0.0589
CellPerimeter	Cell morphometry	0.1068	-0.0787	-0.01367
CellSolidity	Cell morphometry	-0.0167	0.1191	-0.1204
CellConvexPerimeter	Cell morphometry	0.1133	-0.0731	0.0151
CellEquivDiameterPerim	Cell morphometry	0.1068	-0.0787	-0.0137
CellRatioMajorMinor	Cell morphometry	-0.0527	-0.1147	0.1160
CellCircularity	Cell morphometry	0.0372	0.1216	-0.1464
CellMeanCentroidDist	Cell morphometry	0.1151	-0.0593	0.0065
CellMaxCentroidDist	Cell morphometry	0.1010	-0.0926	0.0507
CellMinCentroidDist	Cell morphometry	0.0878	0.0444	-0.0818
CellCVCentroidDist	Cell morphometry	-0.0338	-0.1318	0.1546
CellVarCentroidDist	Cell morphometry	0.0554	-0.1169	0.0625
CellLowSmoothArea	Cell morphometry	0.1022	-0.0478	-0.0645
CellLowSmoothPerimeter	Cell morphometry	0.1090	-0.0709	-0.0145
CellLowSmoothOrigAreaChange	Cell morphometry	-0.0202	0.0597	-0.0348
CellLowSmoothOrigAreaChangeRel	Cell morphometry	0.0495	0.0904	-0.0571
CellLowSmoothOrigPerimeterChange	Cell morphometry	-0.0792	0.0804	0.0089
CellLowSmoothOrigPerimeterChangeRel	Cell morphometry	-0.0290	0.0639	-0.0388
CellLowSmoothOrigAreaRatio	Cell morphometry	0.0495	0.0904	-0.0571
CellLowSmoothOrigPerimeterRatio	Cell morphometry	-0.0290	0.0639	-0.0388
CellHighSmoothArea	Cell morphometry	0.1023	-0.0404	-0.0571
CellHighSmoothPerimeter	Cell morphometry	0.1132	-0.0437	-0.0388
CellHighSmoothOrigAreaChange	Cell morphometry	-0.0284	0.0855	-0.0664
CellHighSmoothOrigAreaChangeRel	Cell morphometry	0.0777	0.1119	-0.0199
CellHighSmoothOrigPerimeterChange	Cell morphometry	-0.0770	0.1047	-0.0079
CellHighSmoothOrigPerimeterChangeRel	Cell morphometry	0.0122	0.1223	-0.0446
CellHighSmoothOrigAreaRatio	Cell morphometry	0.0777	0.1119	0.0034
CellHighSmoothOrigPerimeterRatio	Cell morphometry	0.0122	0.1223	-0.0547
NucNumber	Nucleus morphometry	0.0253	-0.0495	-0.0288
NucArea	Nucleus morphometry	0.1084	-0.0587	-0.0434
NucMeanArea	Nucleus morphometry	0.1025	-0.0395	-0.0283
NucCellAreaRatio	Nucleus morphometry	-0.0936	-0.0338	-0.0423
NucCellCentroidDist	Nucleus morphometry	0.0606	-0.0669	0.0127
NucConvexArea	Nucleus morphometry	0.1077	-0.0628	-0.0472
NucEccentricity	Nucleus morphometry	-0.0166	-0.0815	0.0542
NucEquivDiameterArea	Nucleus morphometry	0.1173	-0.0374	-0.0222
NucMajorAxisLength	Nucleus morphometry	0.1051	-0.0661	-0.0035
NucMinorAxisLength	Nucleus morphometry	0.1145	-0.0134	-0.0391
NucPerimeter	Nucleus morphometry	0.1118	-0.0591	-0.0313
NucMeanPerimeter	Nucleus morphometry	0.1005	-0.0271	-0.0093
NucCellPerimeterRatio	Nucleus morphometry	-0.0885	0.0217	-0.0955
NucSolidity	Nucleus morphometry	-0.0078	0.0824	0.0795
NucConvexPerimeter	Nucleus morphometry	0.1143	-0.0519	-0.0205
NucEquivDiameterPerim	Nucleus morphometry	0.1118	-0.0591	-0.0313
NucRatioMajorMinor	Nucleus morphometry	-0.0139	-0.0913	0.0607
NucCircularity	Nucleus morphometry	0.0168	0.0941	-0.0506
NucMeanCentroidDist	Nucleus morphometry	0.1166	-0.0424	-0.0181

Feature Name	Feature Type	PC1 (fixed)	PC2 (fixed)	PC3 (fixed)
NucMaxCentroidDist	Nucleus morphometry	0.1055	-0.0698	-0.0121
NucMinCentroidDist	Nucleus morphometry	0.1047	0.0143	-0.0115
NucCVCentroidDist	Nucleus morphometry	-0.0155	-0.1018	0.0338
NucVarCentroidDist	Nucleus morphometry	0.0373	-0.0898	0.0077
NucLowSmoothArea	Nucleus morphometry	0.1084	-0.0585	-0.0432
NucLowSmoothPerimeter	Nucleus morphometry	0.1130	-0.0548	-0.0248
NucLowSmoothOrigAreaChange	Nucleus morphometry	-0.0241	0.0439	0.0482
NucLowSmoothOrigAreaChangeRel	Nucleus morphometry	0.1021	0.0425	0.0516
NucLowSmoothOrigPerimeterChange	Nucleus morphometry	-0.0329	0.07571	0.0907
NucLowSmoothOrigPerimeterChangeRel	Nucleus morphometry	0.0088	0.07282	0.1059
NucLowSmoothOrigAreaRatio	Nucleus morphometry	0.1021	0.04250	0.0516
NucLowSmoothOrigPerimeterRatio	Nucleus morphometry	0.0088	0.0728	0.1059
NucHighSmoothArea	Nucleus morphometry	0.1084	-0.0585	-0.0432
NucHighSmoothPerimeter	Nucleus morphometry	0.1140	-0.0513	-0.0212
NucHighSmoothOrigAreaChange	Nucleus morphometry	-0.0401	0.0437	0.0451
NucHighSmoothOrigAreaChangeRel	Nucleus morphometry	0.1089	0.03579	0.0369
NucHighSmoothOrigPerimeterChange	Nucleus morphometry	-0.0271	0.0882	0.0962
NucHighSmoothOrigPerimeterChangeRel	Nucleus morphometry	0.0420	0.0871	0.1056
NucHighSmoothOrigAreaRatio	Nucleus morphometry	0.1089	0.0358	0.0369
NucHighSmoothOrigPerimeterRatio	Nucleus morphometry	0.0420	0.0871	0.1056
CellMeanContrast	Cell texture	-0.0659	0.0448	0.0497
CellMinContrast	Cell texture	-0.0426	0.0957	0.0119
CellMaxContrast	Cell texture	-0.0687	0.0107	0.0730
CellCVContrast	Cell texture	-0.0585	-0.0933	0.1252
CellVarContrast	Cell texture	-0.0438	-0.0303	0.0546
CellMeanCorrelation	Cell texture	-0.0343	-0.0721	-0.0892
CellMinCorrelation	Cell texture	-0.0199	-0.0409	-0.1279
CellMaxCorrelation	Cell texture	-0.0503	-0.0928	-0.0382
CellCVCorrelation	Cell texture	-0.0068	-0.0033	0.1573
CellVarCorrelation	Cell texture	-0.0101	-0.0185	0.1433
CellMeanEnergy	Cell texture	0.0370	-0.1062	0.0048
CellMinEnergy	Cell texture	0.0405	-0.1019	-0.0019
CellMaxEnergy	Cell texture	0.0331	-0.1096	0.0093
CellCVEnergy	Cell texture	-0.0673	0.0182	0.0524
CellVarEnergy	Cell texture	-0.0463	-0.0948	0.0676
CellMeanHomogeneity	Cell texture	0.0553	-0.0926	-0.0238
CellMinHomogeneity	Cell texture	0.0615	-0.0734	-0.0442
CellMaxHomogeneity	Cell texture	0.0402	-0.1118	-0.0042
CellCVHomogeneity	Cell texture	-0.0736	-0.0013	0.0768
CellVarHomogeneity	Cell texture	-0.0713	-0.0342	0.0774
CellFracTotalDisc1	Cell texture	-0.0316	-0.1393	0.1055
CellCVDisc1	Cell texture	-0.0327	-0.1397	0.1245
CellVarDisc1	Cell texture	-0.0686	-0.0826	-0.0200
CellFracTotalDisc2	Cell texture	-0.0194	-0.1021	0.0604
CellCVDisc2	Cell texture	-0.0383	-0.1526	0.1344
CellVarDisc2	Cell texture	-0.0707	-0.0459	-0.0884
CellFracTotalDisc3	Cell texture	-0.0102	-0.0157	-0.0113
CellCVDisc3	Cell texture	-0.0398	-0.1558	0.1324
CellVarDisc3	Cell texture	-0.0636	-0.0209	-0.1152
CellFracTotalDisc4	Cell texture	0.1032	0.0342	0.0315
CellCVDisc4	Cell texture	-0.0463	-0.1528	0.1208
CellVarDisc4	Cell texture	-0.0602	-0.01498	-0.1191

Feature Name	Feature Type	PC1 (fixed)	PC2 (fixed)	PC3 (fixed)
NucMeanContrast	Nucleus texture	-0.0962	-0.0062	0.0238
NucMinContrast	Nucleus texture	-0.0866	0.0138	0.0280
NucMaxContrast	Nucleus texture	-0.0986	-0.0201	0.0236
NucCVContrast	Nucleus texture	-0.0891	-0.05296	0.0214
NucVarContrast	Nucleus texture	-0.0839	-0.0451	0.0101
NucMeanCorrelation	Nucleus texture	-0.0467	-0.0860	-0.1183
NucMinCorrelation	Nucleus texture	-0.0340	-0.0791	-0.1303
NucMaxCorrelation	Nucleus texture	-0.0590	-0.0863	-0.1048
NucCVCorrelation	Nucleus texture	0.0156	0.0729	0.1339
NucVarCorrelation	Nucleus texture	0.0098	0.0664	0.1287
NucMeanEnergy	Nucleus texture	0.0811	0.0348	0.0339
NucMinEnergy	Nucleus texture	0.0817	0.0359	0.0290
NucMaxEnergy	Nucleus texture	0.0806	0.0348	0.0371
NucCVEnergy	Nucleus texture	-0.0894	-0.0493	-0.0020
NucVarEnergy	Nucleus texture	0.0498	0.01853	0.0712
NucMeanHomogeneity	Nucleus texture	0.1041	0.02283	0.0212
NucMinHomogeneity	Nucleus texture	0.1065	0.03256	0.0181
NucMaxHomogeneity	Nucleus texture	0.0986	0.01130	0.0214
NucCVHomogeneity	Nucleus texture	-0.1028	-0.0605	-0.0202
NucVarHomogeneity	Nucleus texture	-0.0929	-0.0697	-0.0134
NucFracTotalDisc1	Nucleus texture	-0.0497	-0.1191	0.0032
NucCVDisc1	Nucleus texture	0.0310	-0.0271	0.0015
NucVarDisc1	Nucleus texture	-0.0441	-0.0518	-0.0597
NucFracTotalDisc2	Nucleus texture	-0.0541	-0.1134	0.0009
NucCVDisc2	Nucleus texture	0.0001	-0.0850	0.0185
NucVarDisc2	Nucleus texture	-0.0525	-0.0650	-0.0500
NucFracTotalDisc3	Nucleus texture	-0.0478	-0.0991	-0.0231
NucCVDisc3	Nucleus texture	-0.0279	-0.1161	0.0230
NucVarDisc3	Nucleus texture	-0.0685	-0.07284	-0.0551
NucFracTotalDisc4	Nucleus texture	0.1058	0.0005	0.0077
NucCVDisc4	Nucleus texture	-0.0305	-0.1204	0.0174
NucVarDisc4	Nucleus texture	-0.0730	-0.0568	-0.0750
MitoNumber	Mito morphometry	0.0926	-0.0221	-0.0650
MitoSumArea	Mito morphometry	0.0965	-0.0542	-0.0721
MitoMeanArea	Mito morphometry	-0.0620	-0.0806	-0.0583
MitoMedianArea	Mito morphometry	0.0026	-0.0094	0.0736
MitoMaxArea	Mito morphometry	0.0390	-0.0994	-0.1042
MitoMinArea	Mito morphometry	-0.0305	-0.0317	-0.0138
MitoCVArea	Mito morphometry	0.0153	-0.0921	-0.1174
MitoVarArea	Mito morphometry	-0.0187	-0.0581	-0.0740
MitoCellAreaRatio	Mito morphometry	-0.06	-0.0466	-0.0658
MitoSumPerimeter	Mito morphometry	0.0986	-0.0394	-0.0615
MitoMeanPerimeter	Mito morphometry	-0.0419	-0.0649	-0.0025
MitoMedianPerimeter	Mito morphometry	0.0071	-0.0063	0.0795
MitoMaxPerimeter	Mito morphometry	0.0517	-0.0836	-0.0784
MitoMinPerimeter	Mito morphometry	-0.0328	-0.0311	-0.0142
MitoCVPerimeter	Mito morphometry	0.0093	-0.0860	-0.1048
MitoVarPerimeter	Mito morphometry	-0.0119	-0.0839	-0.0551
MitoCellPerimeterRatio	Mito morphometry	0.0772	0.0569	-0.0500
MitoCellCentroidDist	Mito morphometry	0.05280	-0.0661	0.0128
MitoNucCentroidDist	Mito morphometry	0.0601	-0.0578	0.0017
MitoObjSkepRatio	Mito morphometry	-0.0714	-0.0954	-0.0848

Feature Name	Feature Type	PC1 (fixed)	PC2 (fixed)	PC3 (fixed)
MitoNumBranchpoints	Mito morphometry	0.0945	-0.0558	-0.0736
MitoNumEndpoints	Mito morphometry	0.0962	-0.0291	-0.0677
MitoNumberFused	Mito morphometry	0.0967	-0.0210	-0.0580
MitoMeanFusedArea	Mito morphometry	-0.0595	-0.0736	-0.0888
MitoMaxFusedArea	Mito morphometry	0.0390	-0.0994	-0.1042
MitoMinFusedArea	Mito morphometry	-0.0338	-0.0131	-0.0571
MitoCVFusedArea	Mito morphometry	0.0372	-0.0830	-0.0875
MitoVarFusedArea	Mito morphometry	-0.0168	-0.0559	-0.0705
MitoPercentFusedTotalArea	Mito morphometry	-0.0676	-0.0818	-0.0656
MitoNumberFragmented	Mito morphometry	0.0893	-0.0220	-0.0665
MitoMeanFragmentedArea	Mito morphometry	0.0310	-0.0135	0.1068
MitoMaxFragmentedArea	Mito morphometry	0.0689	-0.0345	0.0418
MitoMinFragmentedArea	Mito morphometry	-0.0299	-0.0299	-0.0165
MitoCVFragmentedArea	Mito morphometry	0.0165	-0.0502	0.0210
MitoVarFragmentedArea	Mito morphometry	0.0034	-0.0452	0.0543
MitoRatioFusedFragmented	Mito morphometry	-0.0327	-0.0173	-0.0406
MitoPercentFragmentedTotalArea	Mito morphometry	0.0676	0.0818	0.0656
MitoMeanContrast	Mitochondria texture	-0.0859	0.0268	-0.0188
MitoMinContrast	Mitochondria texture	-0.0837	0.0317	-0.0269
MitoMaxContrast	Mitochondria texture	-0.0871	0.0193	-0.0099
MitoCVContrast	Mitochondria texture	-0.0425	-0.0364	0.0738
MitoVarContrast	Mitochondria texture	-0.0802	-0.0015	-0.0211
MitoMeanCorrelation	Mitochondria texture	-0.0749	-0.0765	-0.1055
MitoMinCorrelation	Mitochondria texture	-0.0695	-0.0670	-0.1279
MitoMaxCorrelation	Mitochondria texture	-0.0741	-0.0733	-0.0774
MitoCVCorrelation	Mitochondria texture	0.0625	0.0698	0.1369
MitoVarCorrelation	Mitochondria texture	0.0529	0.0618	0.1436
MitoMeanEnergy	Mitochondria texture	0.0803	0.0075	0.0518
MitoMinEnergy	Mitochondria texture	0.0807	0.0088	0.0479
MitoMaxEnergy	Mitochondria texture	0.0797	0.0066	0.0544
MitoCVEnergy	Mitochondria texture	-0.0852	-0.0393	-0.0108
MitoVarEnergy	Mitochondria texture	-0.0587	-0.0448	0.0619
MitoMeanHomogeneity	Mitochondria texture	0.0864	-0.0014	0.0458
MitoMinHomogeneity	Mitochondria texture	0.0873	0.0052	0.0392
MitoMaxHomogeneity	Mitochondria texture	0.0849	-0.0072	0.0506
MitoCVHomogeneity	Mitochondria texture	-0.0876	-0.0341	-0.0207
MitoVarHomogeneity	Mitochondria texture	-0.0846	-0.0499	-0.0131
MitoFracTotalDisc1	Mitochondria texture	0.0189	-0.1073	0.0938
MitoCVDisc1	Mitochondria texture	0.0017	-0.0029	0.0584
MitoVarDisc1	Mitochondria texture	-0.0029	0.0034	-0.0567
MitoFracTotalDisc2	Mitochondria texture	0.0190	-0.0614	0.0612
MitoCVDisc2	Mitochondria texture	0.0315	-0.1074	0.1725
MitoVarDisc2	Mitochondria texture	-0.0168	0.0258	-0.0779
MitoFracTotalDisc3	Mitochondria texture	0.0112	0.0107	0.0025
MitoCVDisc3	Mitochondria texture	0.0339	-0.1069	0.1716
MitoVarDisc3	Mitochondria texture	-0.0194	0.0241	-0.0774
MitoFracTotalDisc4	Mitochondria texture	0.0961	0.0283	0.0297
MitoCVDisc4	Mitochondria texture	0.03475	-0.0981	0.1698
MitoVarDisc4	Mitochondria texture	-0.0185	0.0200	-0.0737

Table A2. Complete loadings of the first three Principal Components of fixed WT MEFs. The loading values of the first three principal components of a 205-feature set analysis of WT MEF morphology. Principal Component 1 captures 29.6% of the total variance; Principal Component 2 captures 10.6% of the total variance; Principal Component 3 captures 6.7% of the total variance.

Feature Name	Feature Type	PC1 (live)	PC2 (live)	PC3 (live)
CellArea	Cell morphometry	0.1240	-0.0392	-0.0452
CellConvexArea	Cell morphometry	0.1284	-0.0459	-0.0215
CellEccentricity	Cell morphometry	-0.0032	-0.0439	0.1229
CellEquivDiameterArea	Cell morphometry	0.1301	-0.0391	-0.0492
CellMajorAxisLength	Cell morphometry	0.1124	-0.0677	0.0546
CellMinorAxisLength	Cell morphometry	0.1153	-0.0156	-0.0864
CellPerimeter	Cell morphometry	0.1292	-0.0396	-0.0013
CellSolidity	Cell morphometry	-0.0574	0.0336	-0.0731
CellConvexPerimeter	Cell morphometry	0.1321	-0.0541	0.0052
CellEquivDiameterPerim	Cell morphometry	0.1292	-0.0396	-0.0013
CellRatioMajorMinor	Cell morphometry	-0.0009	-0.0476	0.1375
CellCircularity	Cell morphometry	-0.0131	0.0476	-0.1369
CellMeanCentroidDist	Cell morphometry	0.1324	-0.0537	-0.0051
CellMaxCentroidDist	Cell morphometry	0.1202	-0.0611	0.0379
CellMinCentroidDist	Cell morphometry	0.07416	0.0064	-0.1114
CellCVCentroidDist	Cell morphometry	0.0220	-0.0489	0.1355
CellVarCentroidDist	Cell morphometry	0.0772	-0.0674	0.0879
CellLowSmoothArea	Cell morphometry	0.1239	-0.0394	-0.0454
CellLowSmoothPerimeter	Cell morphometry	0.1296	-0.0502	0.0002
CellLowSmoothOrigAreaChange	Cell morphometry	0.0068	-0.0164	-0.0181
CellLowSmoothOrigAreaChangeRel	Cell morphometry	0.0309	-0.0230	-0.0378
CellLowSmoothOrigPerimeterChange	Cell morphometry	-0.0949	-0.0024	0.0053
CellLowSmoothOrigPerimeterChangeRel	Cell morphometry	-0.0608	-0.0392	-0.0070
CellLowSmoothOrigAreaRatio	Cell morphometry	0.0309	-0.0230	-0.0378
CellLowSmoothOrigPerimeterRatio	Cell morphometry	-0.0608	-0.0392	-0.0070
CellHighSmoothArea	Cell morphometry	0.1226	-0.0383	-0.0469
CellHighSmoothPerimeter	Cell morphometry	0.129	-0.0477	-0.0068
CellHighSmoothOrigAreaChange	Cell morphometry	-0.0427	0.0245	-0.0296
CellHighSmoothOrigAreaChangeRel	Cell morphometry	0.0188	0.0126	-0.0646
CellHighSmoothOrigPerimeterChange	Cell morphometry	-0.0944	0.0172	-0.0072
CellHighSmoothOrigPerimeterChangeRel	Cell morphometry	-0.0575	-0.0038	-0.0311
CellHighSmoothOrigAreaRatio	Cell morphometry	0.0188	0.0126	-0.0646
CellHighSmoothOrigPerimeterRatio	Cell morphometry	-0.0575	-0.0038	-0.0311
NucNumber	Nucleus morphometry	0.0550	-0.0218	0.0539
NucArea	Nucleus morphometry	0.1270	-0.0051	0.0368
NucMeanArea	Nucleus morphometry	0.1059	0.0073	0.0121
NucCellAreaRatio	Nucleus morphometry	-0.0819	0.0533	0.1070
NucCellCentroidDist	Nucleus morphometry	0.0751	-0.0151	0.0236
NucConvexArea	Nucleus morphometry	0.1257	-0.0008	0.0469
NucEccentricity	Nucleus morphometry	0.0161	-0.0453	0.1496
NucEquivDiameterArea	Nucleus morphometry	0.1307	-0.0043	0.0327
NucMajorAxisLength	Nucleus morphometry	0.1133	-0.0225	0.1046
NucMinorAxisLength	Nucleus morphometry	0.1201	0.0196	-0.0447
NucPerimeter	Nucleus morphometry	0.1219	0.0081	0.0811
NucMeanPerimeter	Nucleus morphometry	0.0832	0.0258	0.0403
NucCellPerimeterRatio	Nucleus morphometry	-0.0959	0.0603	0.0622
NucSolidity	Nucleus morphometry	-0.0387	-0.0507	-0.1263
NucConvexPerimeter	Nucleus morphometry	0.1259	-0.0055	0.0691
NucEquivDiameterPerim	Nucleus morphometry	0.1219	0.0081	0.0811
NucRatioMajorMinor	Nucleus morphometry	0.0185	-0.0472	0.1741
NucCircularity	Nucleus morphometry	-0.0178	0.0455	-0.1726
NucMeanCentroidDist	Nucleus morphometry	0.1295	-0.0059	0.0452

Feature Name	Feature Type	PC1 (live)	PC2 (live)	PC3 (live)
NucMaxCentroidDist	Nucleus morphometry	0.1139	-0.0117	0.1082
NucMinCentroidDist	Nucleus morphometry	0.0808	0.0213	-0.0987
NucCVCentroidDist	Nucleus morphometry	0.0223	-0.0399	0.1825
NucVarCentroidDist	Nucleus morphometry	0.0627	-0.0272	0.1475
NucLowSmoothArea	Nucleus morphometry	0.1270	-0.0057	0.0363
NucLowSmoothPerimeter	Nucleus morphometry	0.1238	-0.0043	0.0736
NucLowSmoothOrigAreaChange	Nucleus morphometry	-0.0328	-0.0708	-0.0721
NucLowSmoothOrigAreaChangeRel	Nucleus morphometry	0.0640	-0.0652	-0.0532
NucLowSmoothOrigPerimeterChange	Nucleus morphometry	-0.0491	-0.0931	-0.0956
NucLowSmoothOrigPerimeterChangeRel	Nucleus morphometry	-0.0321	-0.1145	-0.0957
NucLowSmoothOrigAreaRatio	Nucleus morphometry	0.0640	-0.0652	-0.0532
NucLowSmoothOrigPerimeterRatio	Nucleus morphometry	-0.0321	-0.1145	-0.0957
NucHighSmoothArea	Nucleus morphometry	0.1269	-0.0057	0.0361
NucHighSmoothPerimeter	Nucleus morphometry	0.1253	-0.0090	0.0668
NucHighSmoothOrigAreaChange	Nucleus morphometry	-0.0370	-0.0401	-0.0533
NucHighSmoothOrigAreaChangeRel	Nucleus morphometry	0.1069	-0.0262	-0.0166
NucHighSmoothOrigPerimeterChange	Nucleus morphometry	-0.0448	-0.0800	-0.1037
NucHighSmoothOrigPerimeterChangeRel	Nucleus morphometry	-0.0199	-0.0967	-0.1048
NucHighSmoothOrigAreaRatio	Nucleus morphometry	0.1069	-0.0262	-0.0166
NucHighSmoothOrigPerimeterRatio	Nucleus morphometry	-0.0199	-0.0967	-0.1048
CellMeanContrast	Cell texture	0.0149	0.1551	0.0290
CellMinContrast	Cell texture	0.0231	0.1563	0.0205
CellMaxContrast	Cell texture	0.0060	0.1513	0.0391
CellCVContrast	Cell texture	-0.0741	-0.0992	0.0781
CellVarContrast	Cell texture	-0.0665	0.0004	0.0618
CellMeanCorrelation	Cell texture	-0.0297	-0.1529	-0.0137
CellMinCorrelation	Cell texture	-0.0269	-0.1520	-0.0182
CellMaxCorrelation	Cell texture	-0.0319	-0.1526	-0.0106
CellCVCorrelation	Cell texture	-0.0243	0.0920	0.0751
CellVarCorrelation	Cell texture	-0.0393	0.0607	0.0773
CellMeanEnergy	Cell texture	-0.0523	-0.0696	0.0177
CellMinEnergy	Cell texture	-0.0505	-0.0678	0.0151
CellMaxEnergy	Cell texture	-0.0540	-0.0707	0.0202
CellCVEnergy	Cell texture	-0.0491	-0.0704	0.0905
CellVarEnergy	Cell texture	-0.0721	0.0364	0.0629
CellMeanHomogeneity	Cell texture	-0.0432	-0.1538	0.0055
CellMinHomogeneity	Cell texture	-0.0395	-0.1524	-0.0031
CellMaxHomogeneity	Cell texture	-0.0468	-0.1531	0.0126
CellCVHomogeneity	Cell texture	-0.0660	-0.0698	0.09765
CellVarHomogeneity	Cell texture	-0.0612	-0.0677	0.0966
CellFracTotalDisc1	Cell texture	0.0285	-0.0942	0.0617
CellCVDisc1	Cell texture	0.0414	-0.0839	0.1141
CellVarDisc1	Cell texture	0.0298	-0.0874	0.0810
CellFracTotalDisc2	Cell texture	0.0108	-0.0717	0.0371
CellCVDisc2	Cell texture	0.0310	-0.0922	0.1268
CellVarDisc2	Cell texture	-0.0603	-0.0068	0.0497
CellFracTotalDisc3	Cell texture	0.0002	-0.0399	-0.0173
CellCVDisc3	Cell texture	0.0213	-0.0913	0.1184
CellVarDisc3	Cell texture	-0.0817	0.0526	0.0052
CellFracTotalDisc4	Cell texture	0.0442	-0.1036	-0.0330
CellCVDisc4	Cell texture	0.0017	-0.0936	0.1051
CellVarDisc4	Cell texture	-0.0734	0.0652	-0.0050

Feature Name	Feature Type	PC1 (live)	PC2 (live)	PC3 (live)
NucMeanContrast	Nucleus texture	-0.0036	0.1442	0.0573
NucMinContrast	Nucleus texture	0.0166	0.1583	0.0462
NucMaxContrast	Nucleus texture	-0.0274	0.1162	0.0690
NucCVContrast	Nucleus texture	-0.0640	-0.1452	0.0037
NucVarContrast	Nucleus texture	-0.0816	-0.0773	0.0375
NucMeanCorrelation	Nucleus texture	-0.0346	-0.1451	-0.0406
NucMinCorrelation	Nucleus texture	-0.0273	-0.1364	-0.0465
NucMaxCorrelation	Nucleus texture	-0.0399	-0.1504	-0.0366
NucCVCorrelation	Nucleus texture	-0.0639	-0.0902	0.0255
NucVarCorrelation	Nucleus texture	-0.0641	-0.0993	0.0236
NucMeanEnergy	Nucleus texture	0.0321	-0.1047	-0.0705
NucMinEnergy	Nucleus texture	0.0336	-0.1035	-0.0716
NucMaxEnergy	Nucleus texture	0.0308	-0.1059	-0.0697
NucCVEnergy	Nucleus texture	-0.0888	-0.0231	0.0665
NucVarEnergy	Nucleus texture	-0.0191	-0.1131	-0.0214
NucMeanHomogeneity	Nucleus texture	0.0200	-0.1435	-0.0726
NucMinHomogeneity	Nucleus texture	0.0304	-0.1348	-0.0799
NucMaxHomogeneity	Nucleus texture	0.0093	-0.1515	-0.0638
NucCVHomogeneity	Nucleus texture	-0.0975	-0.0681	0.0660
NucVarHomogeneity	Nucleus texture	-0.0860	-0.0766	0.0608
NucFracTotalDisc1	Nucleus texture	-0.0040	-0.0291	0.1786
NucCVDisc1	Nucleus texture	0.0067	0.0350	0.0596
NucVarDisc1	Nucleus texture	0.0111	0.0241	0.0539
NucFracTotalDisc2	Nucleus texture	-0.0180	-0.0208	0.1658
NucCVDisc2	Nucleus texture	0.0191	-0.0141	0.1693
NucVarDisc2	Nucleus texture	0.0227	-0.0295	0.1657
NucFracTotalDisc3	Nucleus texture	-0.0311	0.0036	0.1109
NucCVDisc3	Nucleus texture	0.0033	-0.0338	0.1919
NucVarDisc3	Nucleus texture	0.0007	-0.0453	0.1745
NucFracTotalDisc4	Nucleus texture	0.0378	-0.0854	-0.0143
NucCVDisc4	Nucleus texture	-0.0021	-0.0319	0.1902
NucVarDisc4	Nucleus texture	0.0163	-0.0708	0.0052
MitoNumber	Mito morphometry	0.1054	0.00008	-0.0330
MitoSumArea	Mito morphometry	0.1194	-0.0230	-0.0236
MitoMeanArea	Mito morphometry	-0.0645	-0.0177	0.0278
MitoMedianArea	Mito morphometry	-0.0274	0.0122	0.0242
MitoMaxArea	Mito morphometry	0.0967	-0.0388	-0.0341
MitoMinArea	Mito morphometry	-0.0343	0.0027	0.0152
MitoCVArea	Mito morphometry	0.1004	-0.0202	-0.0472
MitoVarArea	Mito morphometry	0.0062	-0.0471	-0.0129
MitoCellAreaRatio	Mito morphometry	-0.0281	0.0309	0.0412
MitoSumPerimeter	Mito morphometry	0.1189	-0.0034	-0.0178
MitoMeanPerimeter	Mito morphometry	-0.0577	-0.0050	0.0487
MitoMedianPerimeter	Mito morphometry	-0.0215	0.0070	0.0291
MitoMaxPerimeter	Mito morphometry	0.1086	-0.0178	-0.0233
MitoMinPerimeter	Mito morphometry	-0.0380	0.0045	0.0156
MitoCVPerimeter	Mito morphometry	0.0865	-0.0110	-0.0389
MitoVarPerimeter	Mito morphometry	0.0220	-0.0241	0.0053
MitoCellPerimeterRatio	Mito morphometry	0.0621	0.0360	-0.0438
MitoCellCentroidDist	Mito morphometry	0.0598	-0.0413	0.0094
MitoNucCentroidDist	Mito morphometry	0.0609	-0.0042	0.0203
MitoObjSkepRatio	Mito morphometry	-0.0633	-0.0429	0.0266

Feature Name	Feature Type	PC1 (live)	PC2 (live)	PC3 (live)
MitoNumBranchpoints	Mito morphometry	0.1038	0.0233	-0.0215
MitoNumEndpoints	Mito morphometry	0.1121	0.0078	-0.0299
MitoNumberFused	Mito morphometry	0.1098	0.0075	-0.0315
MitoMeanFusedArea	Mito morphometry	-0.0679	-0.0293	0.0259
MitoMaxFusedArea	Mito morphometry	0.0967	-0.0388	-0.0341
MitoMinFusedArea	Mito morphometry	-0.0427	0.0069	0.0295
MitoCVFusedArea	Mito morphometry	0.1122	-0.0164	-0.0520
MitoVarFusedArea	Mito morphometry	0.0116	-0.0541	-0.0233
MitoPercentFusedTotalArea	Mito morphometry	-0.0424	0.01715	0.0143
MitoNumberFragmented	Mito morphometry	0.0983	-0.0035	-0.0320
MitoMeanFragmentedArea	Mito morphometry	0.01231	-0.0308	0.0291
MitoMaxFragmentedArea	Mito morphometry	0.06332	-0.0217	0.0140
MitoMinFragmentedArea	Mito morphometry	-0.0270	-0.0002	0.0117
MitoCVFragmentedArea	Mito morphometry	0.0540	0.0137	-0.0050
MitoVarFragmentedArea	Mito morphometry	0.0187	-0.0089	0.0313
MitoRatioFusedFragmented	Mito morphometry	-0.0544	0.0145	0.0239
MitoPercentFragmentedTotalArea	Mito morphometry	0.0424	-0.0171	-0.0143
MitoMeanContrast	Mitochondria texture	-0.0079	0.0694	0.0567
MitoMinContrast	Mitochondria texture	0.0035	0.0990	0.0286
MitoMaxContrast	Mitochondria texture	-0.0117	0.0476	0.0750
MitoCVContrast	Mitochondria texture	-0.0418	-0.1210	0.0654
MitoVarContrast	Mitochondria texture	-0.0237	-0.0144	0.0883
MitoMeanCorrelation	Mitochondria texture	-0.0491	-0.0893	-0.0021
MitoMinCorrelation	Mitochondria texture	-0.0469	-0.0715	-0.0218
MitoMaxCorrelation	Mitochondria texture	-0.0487	-0.1082	0.0166
MitoCVCorrelation	Mitochondria texture	0.0281	0.0084	0.0440
MitoVarCorrelation	Mitochondria texture	0.0223	0.0008	0.0494
MitoMeanEnergy	Mitochondria texture	-0.0287	-0.1270	-0.0138
MitoMinEnergy	Mitochondria texture	-0.0282	-0.1262	-0.0154
MitoMaxEnergy	Mitochondria texture	-0.0294	-0.1278	-0.0123
MitoCVEnergy	Mitochondria texture	-0.0435	-0.0005	0.0876
MitoVarEnergy	Mitochondria texture	-0.0443	-0.1039	0.0800
MitoMeanHomogeneity	Mitochondria texture	-0.0404	-0.1406	-0.0104
MitoMinHomogeneity	Mitochondria texture	-0.0384	-0.1380	-0.0169
MitoMaxHomogeneity	Mitochondria texture	-0.0427	-0.1428	-0.0041
MitoCVHomogeneity	Mitochondria texture	-0.0321	-0.0006	0.0918
MitoVarHomogeneity	Mitochondria texture	-0.0462	-0.0442	0.0962
MitoFracTotalDisc1	Mitochondria texture	0.0766	-0.0533	0.0248
MitoCVDisc1	Mitochondria texture	-0.0131	0.0234	0.0128
MitoVarDisc1	Mitochondria texture	0.0177	-0.0427	-0.0392
MitoFracTotalDisc2	Mitochondria texture	0.0762	-0.0251	0.0052
MitoCVDisc2	Mitochondria texture	0.0698	-0.0376	0.0950
MitoVarDisc2	Mitochondria texture	-0.0877	0.0119	-0.0671
MitoFracTotalDisc3	Mitochondria texture	0.0598	-0.0110	-0.0167
MitoCVDisc3	Mitochondria texture	0.0775	-0.0374	0.0812
MitoVarDisc3	Mitochondria texture	-0.0995	0.0093	-0.0442
MitoFracTotalDisc4	Mitochondria texture	0.1041	-0.0275	-0.0337
MitoCVDisc4	Mitochondria texture	0.0783	-0.0339	0.0709
MitoVarDisc4	Mitochondria texture	-0.0988	0.0080	-0.0299

Table A3. Complete loadings of the first three Principal Components of live WT MEFs. The loading values of the first three principal components of a 205-feature set analysis of WT MEF morphology. Principal Component 1 captures 23.4% of the total variance; Principal Component 2 captures 11.8% of the total variance; Principal Component 3 captures 8.6% of the total variance.

ATGCCAGAGCCAGCGAAGTCTGCTCCCGCCCCGAAAAAGGGCTCCAAGAAGGCGGTGACTAAGGCGC
AGAAGAAAGGCGGCAAGAAGCGCAAGCGCAGCCGCAAGGAGAGCTATTCCATCTATGTGTACAAGGT
TCTGAAGCAGGTCCACCCTGACACCGGCATTCGTCCAAGGCCATGGGCATCATGAATTCGTTTGTGA
ACGACATTTTCGAGCGCATCGCAGGTGAGGCTTCCCGCCTGGCGCATTACAACAAGCGCTCGACCATC
ACCTCCAGGGAGATCCAGACGGCCGTGCGCCTGCTGCTGCCTGGGGAGTTGGCCAAGCACGCCGTGTC
CGAGGGTACTAAGGCCATCACCAAGTACACCAGCGCTAAGGATCCACCGGTGCGCCACCATGTCGGTAC
CGCTGACTACCTCAGCATTCGGCCACGCGTTTCTGGCTAACTGTGAACGCGAGCAGATCCACCTGGCG
GGCTCCATTAGCCGCACGGTATCCTGCTGGCTGTGAAAGAGCCGGACAACGTGGTGATCCAGGCTTC
TATTAACGCTGCGGAGTTCCTGAACACCAACTCTGTTGTTGGCCGTCCGCTGCGTGACCTGGGCGGCG
ATCTGCCTTTGCAGATCCTGCCGCACCTGAACGGCCCGCTGCACCTGGCTCCGATGACCCTGCGTTGTA
CCGTGGGTTCTCCGCCGCGTCGTGTGGACTGTACCATTATCGTCCGTCTAACGGCGGCCTGATCGTAG
AACTGGAACCAGCAACCAAGACCACTAACATTGCGCCGGCTCTGGACGGTGCGTTTTCATCGTATCACT
TCTTCATCCTCCCTGATGGGCCTGTGTGACGAAACCGCGACTATTATCCGTGAGATTACTGGCTACGAC
CGTGTGATGGTAGTACGTTTCGATGAAGAGGGTAATGGCGAAATTCTGTCCGAACGTCGTCGTGCGGA
CCTGGAAGCGTTCCTGGGTAACCGCTACCCGGCGTCTACTATTCCGCAGATCGCTCGTCGCCTGTACGA
ACATAACCGTGTTCGCCTGCTGGTAGATGTGAACTATACTCCGGTTCGGCTACAGCCGCGCATCAGCCC
GCTGAACGGTCGTGATCTGGATATGTCCTGTCTTGCTGCGCTCTATGTCCCCGATCCACCAGAAATA
CATGCAGGACATGGGCGTTGGCGGACCCCTGGTTTGCTCTCTGATGGTGTCTGGTCGTCTGTGGGGTCT
GATCGCTTGCCACCACTACGAACCGCGCTTCGTTCCGTTCCACATTCGCGCTGCTGGCGAAGCGCTGGC
GGAAACTTGTGCGATCCGCATCGCGACGCTGGAGAGCTTGCACAGTCTCAGTCCAAAAGGAAGCGGA
GCTACTAACTTCAGCCTGCTGAAGCAGGCTGGAGACGTGGAGGAGAACCCTGGACCTTCCGTCCTGAC
GCCGCTGCTGCTGCGGGGCTTGACAGGCTCGGCCCGGCGGCTCCAGTGCCGCGCGCCAAGATCCAT
CGTTGGGGATCCACCGGTGCGCCACCATGGTGAGCAAGGGCGAGGAGGTCATCAAAGAGTTCATGCG
CTTCAAGGTGCGCATGGAGGGCTCCATGAACGGCCACGAGTTCGAGATCGAGGGCGAGGGCGAGGGC
CGCCCCTACGAGGGCACCCAGACCGCCAAGCTGAAGGTGACCAAGGGCGGCCCCCTGCCCTTCGCCTG
GGACATCCTGTCCCCCAGTTCATGTACGGCTCCAAGGCGTACGTGAAGCACCCCGCCGACATCCCCG
ATTACAAGAAGCTGTCTTCCCCGAGGGCTTCAAGTGGGAGCGCGTGATGAACTTCGAGGACGGCGGT
CTGGTGACCGTGACCCAGGACTCCTCCCTGCAGGACGGCACGCTGATCTACAAGGTGAAGATGCGCGG

CACCAACTTCCCCCGACGGCCCCGTAATGCAGAAGAAGACCATGGGCTGGGAGGCCTCCACCGAG
GGCCTGTACCCCGCGACGGCGTGCTGAAGGGCGAGATCCACCAGGCCCTGAAGCTGAAGGACGGCG
GCCACTACCTGGTGGAGTTCAAGACCATCTACATGGCCAAGAAGCCCGTGCAACTGCCCGGCTACTAC
TACGTGGACACCAAGCTGGACATCACCTCCCACAACGAGGACTACACCATCGTGGAACAGTACGAGC
GCTCCGAGGGCCGCCACCACCTGTTCCCTGGGGCATGGCACCGGCAGCACCGGCAGCGGCAGCTCCGGC
ACCGCCTCCTCCGAGGACAACAACATGGCCGTCATCAAAGAGTTCATGCGCTTCAAGGTGCGCATGGA
GGGCTCCATGAACGGCCACGAGTTCGAGATCGAGGGCGAGGGCGAGGGCCGCCCTACGAGGGCACC
CAGACCGCCAAGCTGAAGGTGACCAAGGGCGGCCCCCTGCCCTTCGCCTGGGACATCCTGTCCCCCA
GTTTCATGTACGGCTCCAAGGCGTACGTGAAGCACCCCGCCGACATCCCCGATTACAAGAAGCTGTCTT
TCCCCGAGGGCTTCAAGTGGGAGCGCGTGATGAACTTCGAGGACGGCGGTCTGGTGACCGTGACCCAG
GACTCCTCCTGCAGGACGGCACGCTGATCTACAAGGTGAAGATGCGCGGCACCAACTTCCCCCCGA
CGGCCCGTAATGCAGAAGAAGACCATGGGCTGGGAGGCCTCCACCGAGCGCCTGTACCCCGCGAC
GGCGTGCTGAAGGGCGAGATCCACCAGGCCCTGAAGCTGAAGGACGGCGGCCACTACCTGGTGGAGT
TCAAGACCATCTACATGGCCAAGAAGCCCGTGCAACTGCCCGGCTACTACTACGTGGACACCAAGCTG
GACATCACCTCCCACAACGAGGACTACACCATCGTGGAACAGTACGAGCGCTCCGAGGGCCGCCACC
ACCTGTTCCCTGTACGGCATGGACGAGCTGTACAAGGGAAGCGGAGCTACTAACTTCAGCCTGCTGAAG
CAGGCTGGAGACGTGGAGGAGAACCCTGGACCTGTGAGCAAGGGCGAGGAGCTGTTACCCGGGGTGG
TGCCCATCCTGGTCGAGCTGGACGGCGACGTAAACGGCCACAAGTTCAGCGTGTCCGGCGAGGGCGA
GGGCGATGCCACCTACGGCAAGCTGACCCTGAAGTTCATCTGCACCACCGGCAAGCTGCCCGTGCCCT
GGCCACCCCTCGTGACCACCCTGACCTACGGCGTGCAAGTTCAGCCGCTACCCCGACCACATGAAG
CAGCACGACTTCTTCAAGTCCGCCATGCCCGAAGGCTACGTCCAGGAGCGCACCATCTTCTTCAAGGA
CGACGGCAACTACAAGACCCGCGCCGAGGTGAAGTTCGAGGGCGACACCCTGGTGAACCCGATCGAG
CTGAAGGGCATCGACTTCAAGGAGGACGGCAACATCCTGGGGCACAAGCTGGAGTACA ACTACAACA
GCCACAACGTCTATATCATGGCCGACAAGCAGAAGAACGGCATCAAGGTGAACTTCAAGATCCGCCA
CAACATCGAGGACGGCAGCGTGCAGCTCGCCGACCACTACCAGCAGAACACCCCCATCGGCGACGGC
CCCGTGCTGCTGCCCGACAACCACTACCTGAGCACCCAGTCCGCCCTGAGCAAAGACCCCAACGAGAA
GCGCGATCACATGGTCCCTGCTGGAGTTCGTGACCGCCGCCGGGATCACTCTCGGCATGGACGAGCTGT
ACAAGTCCGGACTCAGATCTCGAGTGCCTGAGTGCATCTCCATCCACGTTGGCCAGGCTGGTGTCCAG

ATTGGCAATGCCTGCTGGGAGCTCTACTGCCTGGAACACGGCATCCAGCCCGATGGCCAGATGCCAAG
TGACAAGACCATTGGGGGAGGAGATGACTCCTTCAACACCTTCTTCAGTGAGACGGGCGCTGGCAAGC
ACGTGCCCCGGGCTGTGTTTGTAGACTTGAACCCACAGTCATTGATGAAGTTCGCACTGGCACCTAC
CGCCAGCTCTTCCACCCTGAGCAGCTCATCACAGGCAAGGAAGATGCTGCCAATAACTATGCCCGAGG
GCACTACACCATTGGCAAGGAGATCATTGACCTTGTGTTGGACCGAATTCGCAAGCTGGCTGACCAGT
GCACCGGTCTTCAGGGCTTCTTGTTTTCCACAGCTTTGGTGGGGGAACTGGTTCTGGGTTACCTCCC
TGCTCATGGAACGTCTCTCAGTTGATTATGGCAAGAAGTCCAAGCTGGAGTTCTCCATTTACCCAGCAC
CCCAGTTTTCCACAGCTGTAGTTGAGCCCTACAACCTCCATCCTCACCACCCACACCACCCTGGAGCACT
CTGATTGTGCCTTCATGGTAGACAATGAGGCCATCTATGACATCTGTCTGAGAAACCTCGATATCGAG
CGCCCAACCTACACTAACCTTAACCGCCTTATTAGCCAGATTGTGTCCTCCATCACTGCTTCCCTGAGA
TTTGATGGAGCCCTGAATGTTGACCTGACAGAATTCAGACCAACCTGGTGCCCTACCCCCGCATCCA
CTTCCCTCTGGCCACATATGCCCTGTCATCTCTGCTGAGAAAGCCTACCATGAACAGCTTTCTGTAGC
AGAGATACCAATGCTTGCTTTGAGCCAGCCAACCAGATGGTGAAATGTGACCCTCGCCATGGTAAAT
ACATGGCTTGCTGCCTGTTGTACCGTGGTGACGTGGTTCCCAAAGATGTCAATGCTGCCATTGCCACCA
TCAAAACCAAGCGCAGCATCCAGTTTGTGGATTGGTGCCCCACTGGCTTCAAGGTTGGCATCAACTAC
CAGCCTCCCCTGTGGTGCCTGGTGGAGACCTGGCCAAGGTACAGAGAGCTGTGTGCATGCTGAGCAA
CACCACAGCCATTGCTGAGGCCTGGGCTCGCCTGGACCACAAGTTTGACCTGATGTATGCCAAGCGTG
CCTTTGTTCACTGGTACGTGGGTGAGGGGATGGAGGAAGGCGAGTTTTTCAGAGGCCCGTGAAGATATG
GCTGCCCTTGAGAAGGATTATGAGGAGGTTGGTGTGGATTCTGTTGAAGGAGAGGGTGAGGAAGAAG
GAGAGGAATACTAA

Figure A1. Sequence of 3Reporter Cassette. Full sequence of the 3ReporterCassette inserted into the pWPXL lentivirus expression vector. cyan = H2B; green = mIFP; red = P2A; blue = mitochondria localization sequence; yellow = tdTomato dimer; magenta = EGFP; grey = α -tubulin

```

% Algorithm to segment and categorize cells, and stitch necessary ones
% (using MIJ ImageJ interface).
% Revised 03/02/2017 by Amy Chang (Marshall Lab, UCSF)

javaaddpath('/Applications/MATLAB_R2014b.app/java/mij.jar')
javaaddpath('/Applications/MATLAB_R2014b.app/java/ij.jar')
MIJ.start('/Applications/ImageJ/ImageJ/ImageJ/plugins')
alphabet = 'ABCDEFGHJKLMNPO'
column = 1:24
Cy5_7x7 = cell(7);
FITC_7x7 = cell(7);
DAPI_7x7 = cell(7);
DAPI_7x7orig = cell(7);
DAPIlines = zeros(1024, 1024);
for i = 2:length(alphabet);
    for j = 24:length(column);
        for k = 1:49;
            Cy5file = strcat('/Volumes/Fantom
HD/20141223/Amy_Chang/Amy_Chang_Chang1_2014.12.24.20.10.07/',
alphabet(i), '-', {' '}, num2str(j), '(fld ', {' '}, num2str(k), ' wv
Cy5 - Cy5).tif');
            FITCfile = strcat('/Volumes/Fantom
HD/20141223/Amy_Chang/Amy_Chang_Chang1_2014.12.24.20.10.07/',
alphabet(i), '-', {' '}, num2str(j), '(fld ', {' '}, num2str(k), ' wv
FITC - FITC).tif');
            DAPIfile = strcat('/Volumes/Fantom
HD/20141223/Amy_Chang/Amy_Chang_Chang1_2014.12.24.20.10.07/',
alphabet(i), '-', {' '}, num2str(j), '(fld ', {' '}, num2str(k), ' wv
DAPI - DAPI).tif');
            Cy5image = imread(Cy5file{1});
            FITCimage = imread(FITCfile{1});
            DAPIimage = imread(DAPIfile{1});
            Cy5_7x7{k} = Cy5image;
            FITC_7x7{k} = FITCimage;
            DAPI_7x7orig{k} = DAPIimage;
            DAPIlines = DAPIimage;
            DAPIlines(:, 1023) = 1;
            DAPIlines(:, 1024) = 1;
Add line on right side of FOV
            DAPIlines(1023, :) = 1;
            DAPIlines(1024, :) = 1;
Add line on bottom of FOV
            DAPI_7x7{k} = DAPIlines;
        end
        DAPImatrixorig = [DAPI_7x7orig{1} DAPI_7x7orig{2}
DAPI_7x7orig{3} DAPI_7x7orig{4} DAPI_7x7orig{5} DAPI_7x7orig{6}
DAPI_7x7orig{7};
            DAPI_7x7orig{8} DAPI_7x7orig{9} DAPI_7x7orig{10}
DAPI_7x7orig{11} DAPI_7x7orig{12} DAPI_7x7orig{13} DAPI_7x7orig{14};
            DAPI_7x7orig{15} DAPI_7x7orig{16} DAPI_7x7orig{17}
DAPI_7x7orig{18} DAPI_7x7orig{19} DAPI_7x7orig{20} DAPI_7x7orig{21};
            DAPI_7x7orig{22} DAPI_7x7orig{23} DAPI_7x7orig{24}
DAPI_7x7orig{25} DAPI_7x7orig{26} DAPI_7x7orig{27} DAPI_7x7orig{28};
            DAPI_7x7orig{29} DAPI_7x7orig{30} DAPI_7x7orig{31}
DAPI_7x7orig{32} DAPI_7x7orig{33} DAPI_7x7orig{34} DAPI_7x7orig{35};
            DAPI_7x7orig{36} DAPI_7x7orig{37} DAPI_7x7orig{38}
DAPI_7x7orig{39} DAPI_7x7orig{40} DAPI_7x7orig{41} DAPI_7x7orig{42};
            DAPI_7x7orig{43} DAPI_7x7orig{44} DAPI_7x7orig{45}

```

```

DAPI_7x7orig{46} DAPI_7x7orig{47} DAPI_7x7orig{48} DAPI_7x7orig{49}];
    Cy5matrix = [Cy5_7x7{1} Cy5_7x7{2} Cy5_7x7{3} Cy5_7x7{4}
Cy5_7x7{5} Cy5_7x7{6} Cy5_7x7{7};
                Cy5_7x7{8} Cy5_7x7{9} Cy5_7x7{10} Cy5_7x7{11}
Cy5_7x7{12} Cy5_7x7{13} Cy5_7x7{14};
                Cy5_7x7{15} Cy5_7x7{16} Cy5_7x7{17} Cy5_7x7{18}
Cy5_7x7{19} Cy5_7x7{20} Cy5_7x7{21};
                Cy5_7x7{22} Cy5_7x7{23} Cy5_7x7{24} Cy5_7x7{25}
Cy5_7x7{26} Cy5_7x7{27} Cy5_7x7{28};
                Cy5_7x7{29} Cy5_7x7{30} Cy5_7x7{31} Cy5_7x7{32}
Cy5_7x7{33} Cy5_7x7{34} Cy5_7x7{35};
                Cy5_7x7{36} Cy5_7x7{37} Cy5_7x7{38} Cy5_7x7{39}
Cy5_7x7{40} Cy5_7x7{41} Cy5_7x7{42};
                Cy5_7x7{43} Cy5_7x7{44} Cy5_7x7{45} Cy5_7x7{46}
Cy5_7x7{47} Cy5_7x7{48} Cy5_7x7{49}];
    FITCmatrix = [FITC_7x7{1} FITC_7x7{2} FITC_7x7{3} FITC_7x7{4}
FITC_7x7{5} FITC_7x7{6} FITC_7x7{7};
                FITC_7x7{8} FITC_7x7{9} FITC_7x7{10} FITC_7x7{11}
FITC_7x7{12} FITC_7x7{13} FITC_7x7{14};
                FITC_7x7{15} FITC_7x7{16} FITC_7x7{17} FITC_7x7{18}
FITC_7x7{19} FITC_7x7{20} FITC_7x7{21};
                FITC_7x7{22} FITC_7x7{23} FITC_7x7{24} FITC_7x7{25}
FITC_7x7{26} FITC_7x7{27} FITC_7x7{28};
                FITC_7x7{29} FITC_7x7{30} FITC_7x7{31} FITC_7x7{32}
FITC_7x7{33} FITC_7x7{34} FITC_7x7{35};
                FITC_7x7{36} FITC_7x7{37} FITC_7x7{38} FITC_7x7{39}
FITC_7x7{40} FITC_7x7{41} FITC_7x7{42};
                FITC_7x7{43} FITC_7x7{44} FITC_7x7{45} FITC_7x7{46}
FITC_7x7{47} FITC_7x7{48} FITC_7x7{49}];
    DAPImatrix = [DAPI_7x7{1} DAPI_7x7{2} DAPI_7x7{3} DAPI_7x7{4}
DAPI_7x7{5} DAPI_7x7{6} DAPI_7x7{7};
                DAPI_7x7{8} DAPI_7x7{9} DAPI_7x7{10} DAPI_7x7{11}
DAPI_7x7{12} DAPI_7x7{13} DAPI_7x7{14};
                DAPI_7x7{15} DAPI_7x7{16} DAPI_7x7{17} DAPI_7x7{18}
DAPI_7x7{19} DAPI_7x7{20} DAPI_7x7{21};
                DAPI_7x7{22} DAPI_7x7{23} DAPI_7x7{24} DAPI_7x7{25}
DAPI_7x7{26} DAPI_7x7{27} DAPI_7x7{28};
                DAPI_7x7{29} DAPI_7x7{30} DAPI_7x7{31} DAPI_7x7{32}
DAPI_7x7{33} DAPI_7x7{34} DAPI_7x7{35};
                DAPI_7x7{36} DAPI_7x7{37} DAPI_7x7{38} DAPI_7x7{39}
DAPI_7x7{40} DAPI_7x7{41} DAPI_7x7{42};
                DAPI_7x7{43} DAPI_7x7{44} DAPI_7x7{45} DAPI_7x7{46}
DAPI_7x7{47} DAPI_7x7{48} DAPI_7x7{49}];
    composite_adjusted = cat(3, imadjust(FITCmatrix),
imadjust(Cy5matrix), imadjust(DAPImatrixorig));
    figure, imshow(composite_adjusted)
    Cy5matrix_adjusted = imadjust(Cy5matrix);
    figure, imshow(Cy5matrix_adjusted)
    BW = edge(Cy5matrix_adjusted, 'sobel');
    se90 = strel('line', 6, 90);
    se0 = strel('line', 6, 0);
    BWdil = imdilate(BW, [se90, se0]);
    BWfill = imfill(BWdil, 'holes');
    seD = strel('diamond', 1);
    BWsmooth = imerode(BWfill, seD);
    L = bwlabel(BWsmooth);
    stats = regionprops(L, 'Area');
    areas = cat(1, stats.Area);

```

```

BWsmooth_clean = BWsmooth;
for m = 1:length(stats);
    if stats(m).Area < 1000
        I = find(L==m);
        for n = 1:length(I);
            p = I(n);
            BWsmooth_clean(p) = 0;
        end
    end
end
BWoutline = bwperim(BWsmooth_clean);
%at this point, have the outline of each segmented cell
%need to present each cell to user to identify whether or not
it is
%an acceptable cell (isolated, single cell) and also figure out
%which cells span FOVs and need to be stitched
outline_blue = DAPImatrix;
outline_blue(BWoutline) = 65535;
combo_segmented = imfuse(imadjust(Cy5matrix),
imadjust(outline_blue));
figure, imshow(combo_segmented), title(strcat('Well', {' '},
alphabet(i), '-', {' '}, num2str(j)))
L_clean = bwlabel(BWsmooth_clean); %enumerates
each object in BWsmooth_clean (each cell)
stats_clean = regionprops(L_clean, 'Centroid', 'BoundingBox');
%BoundingBox returns the smallest rectangle
centroids = cat(1, stats_clean.Centroid);
%containing the object
bboxes = cat(1, stats_clean.BoundingBox);
hold on
for p = 1:length(centroids);
    text(centroids(p,1), centroids(p,2), num2str(p), 'color' ,
'r', 'fontsize', 14)
end
hold off
cellinfo = struct('cellnumber', (1:length(bboxes)).',
'coordinates', bboxes(:, :))
for u = 1:length(bboxes);
    if floor(cellinfo.coordinates(u,1)) < 11
        left_x = 1;
    else
        left_x = floor(cellinfo.coordinates(u,1)) - 10;
    end
    if floor(cellinfo.coordinates(u,2)) < 11
        upper_y = 1;
    else
        upper_y = floor(cellinfo.coordinates(u,2)) - 10;
    end
    if ceil(cellinfo.coordinates(u,3) +
cellinfo.coordinates(u,1)) > 7158
        right_x = 7168;
    else
        right_x = ceil(cellinfo.coordinates(u,3) +
cellinfo.coordinates(u,1) + 10);
    end
    if ceil(cellinfo.coordinates(u,4) +
cellinfo.coordinates(u,2)) > 7158
        lower_y = 7168;
    end
end

```

```

else
    lower_y = ceil(cellinfo.coordinates(u,4) +
cellinfo.coordinates(u,2) + 10);
end
boxedDAPIlines = outline_blue(upper_y:lower_y,
left_x:right_x);
boxedDAPIorig = DAPImatrixorig(upper_y:lower_y,
left_x:right_x);
boxedFITC = FITCmatrix(upper_y:lower_y, left_x:right_x);
boxedCy5 = Cy5matrix(upper_y:lower_y, left_x:right_x);
comboboxedadjusted = cat(3, imadjust(boxedFITC),
imadjust(boxedCy5), imadjust(boxedDAPIlines));
origwith_outline = cat(3, boxedFITC, boxedCy5,
boxedDAPIlines);
orig = cat(3, boxedFITC, boxedCy5, boxedDAPIorig);
cellnumber = cellinfo.cellnumber(u);
if cellinfo.coordinates(u,1) < 1;
    category = 5;
    filename = sprintf('/Users/amychang/Documents/Marshall
Lab/20170117_NewWTAlgorithms/Platel_Well%c%d/Platel_Well%c%d_Cell%d_Typ
e%d.tif', alphabet(i), j, alphabet(i), j, u, category);
    imwrite(origwith_outline, filename)
    filename3 = sprintf('/Users/amychang/Documents/Marshall
Lab/20170117_NewWTAlgorithms/Platel_Well%c%d/Platel_Well%c%d_Cell%d_Typ
e%doriginal.tif', alphabet(i), j, alphabet(i), j, u, category);
    imwrite(orig, filename3)
elseif cellinfo.coordinates(u,2) < 1;
    category = 5;
    filename = sprintf('/Users/amychang/Documents/Marshall
Lab/20170117_NewWTAlgorithms/Platel_Well%c%d/Platel_Well%c%d_Cell%d_Typ
e%d.tif', alphabet(i), j, alphabet(i), j, u, category);
    imwrite(origwith_outline, filename)
    filename3 = sprintf('/Users/amychang/Documents/Marshall
Lab/20170117_NewWTAlgorithms/Platel_Well%c%d/Platel_Well%c%d_Cell%d_Typ
e%doriginal.tif', alphabet(i), j, alphabet(i), j, u, category);
    imwrite(orig, filename3)
elseif ceil(cellinfo.coordinates(u,1) +
cellinfo.coordinates(u,3)) > 7067
    category = 5;
    filename = sprintf('/Users/amychang/Documents/Marshall
Lab/20170117_NewWTAlgorithms/Platel_Well%c%d/Platel_Well%c%d_Cell%d_Typ
e%d.tif', alphabet(i), j, alphabet(i), j, u, category);
    imwrite(origwith_outline, filename)
    filename3 = sprintf('/Users/amychang/Documents/Marshall
Lab/20170117_NewWTAlgorithms/Platel_Well%c%d/Platel_Well%c%d_Cell%d_Typ
e%doriginal.tif', alphabet(i), j, alphabet(i), j, u, category);
    imwrite(orig, filename3)
elseif ceil(cellinfo.coordinates(u,2) +
cellinfo.coordinates(u,4)) > 7067
    category = 5;
    filename = sprintf('/Users/amychang/Documents/Marshall
Lab/20170117_NewWTAlgorithms/Platel_Well%c%d/Platel_Well%c%d_Cell%d_Typ
e%d.tif', alphabet(i), j, alphabet(i), j, u, category);
    imwrite(origwith_outline, filename)
    filename3 = sprintf('/Users/amychang/Documents/Marshall
Lab/20170117_NewWTAlgorithms/Platel_Well%c%d/Platel_Well%c%d_Cell%d_Typ
e%doriginal.tif', alphabet(i), j, alphabet(i), j, u, category);
    imwrite(orig, filename3)

```

```

else
    figure, imshow(comboboxedadjusted)
    query = sprintf('This is cell %d. How should it be
categorized? ', cellnumber);
    category = input(query);
    if category == 1;
        filename =
sprintf('/Users/amychang/Documents/Marshall
Lab/20170117_NewWTAlgorithms/Platel_Well%c%d/Platel_Well%c%d_Cell%d_Typ
e%d.tif', alphabet(i), j, alphabet(i), j, u, category);
        imwrite(origwith_outline, filename)
        filename3 =
sprintf('/Users/amychang/Documents/Marshall
Lab/20170117_NewWTAlgorithms/Platel_Well%c%d/Platel_Well%c%d_Cell%d_Typ
e%doriginal.tif', alphabet(i), j, alphabet(i), j, u, category);
        imwrite(orig, filename3)
        close
    end
    if category == 2;
        filename =
sprintf('/Users/amychang/Documents/Marshall
Lab/20170117_NewWTAlgorithms/Platel_Well%c%d/Platel_Well%c%d_Cell%d_Typ
e%d.tif', alphabet(i), j, alphabet(i), j, u, category);
        imwrite(origwith_outline, filename)
        filename3 =
sprintf('/Users/amychang/Documents/Marshall
Lab/20170117_NewWTAlgorithms/Platel_Well%c%d/Platel_Well%c%d_Cell%d_Typ
e%doriginal.tif', alphabet(i), j, alphabet(i), j, u, category);
        imwrite(orig, filename3)
        yesno = 0;
        while yesno == 0
            figure, imshow(mat2gray(boxedCy5))
            h2 = imcontrast(gca)
            waitfor(h2)
            Cy5manual = getimage(gca);
            BW = edge(Cy5manual, 'sobel');
            se90 = strel('line', 6, 90);
            se0 = strel('line', 6, 0);
            BWdil = imdilate(BW, [se90, se0]);
            BWfill = imfill(BWdil, 'holes');
            seD = strel('diamond', 1);
            BWsmooth = imerode(BWfill, seD);
            L = bwlabel(BWsmooth);
            stats = regionprops(L, 'Area');
            areas = cat(1, stats.Area);
            BWsmooth_clean = BWsmooth;
            for m = 1:length(stats);
                if stats(m).Area < 1000
                    I = find(L==m);
                    for q = 1:length(I);
                        p = I(q);
                        BWsmooth_clean(p) = 0;
                    end
                end
            end
            BWoutline2 = bwperim(BWsmooth_clean);
            outline_blue2 = boxedDAPIorig;
            outline_blue2(BWoutline2) = 65535;

```

```

        compositeoutlined = cat(3, boxedFITC, boxedCy5,
outline_blue2);
        figure, imshow(imfuse(imadjust(boxedCy5),
imadjust(outline_blue2)))
        askyesno = sprintf('Is the segmentation
acceptable? (0 = No, 1 = Yes) ');
        yesno = input(askyesno);
        end
        filename4 = strcat(filename(1:(length(filename)-
4)), '_Type1.tif');
        imwrite(compositeoutlined, filename4)
        filename5 = strcat(filename(1:(length(filename)-
4)), '_Type1original.tif');
        composite5 = cat(3, boxedFITC, boxedCy5,
boxedDAPIorig);
        imwrite(composite5, filename5)
        close
        end
        if category == 3;                %Category 3
means cell spans multiple FOVs and needs to be stitched
        filename =
sprintf('/Users/amychang/Documents/Marshall
Lab/20170117_NewWTAlgorithms/Platel_Well%c%d/Platel_Well%c%d_Cell%d_Typ
e%d.tif', alphabet(i), j, alphabet(i), j, u, category);
        imwrite(origwith_outline, filename)
        filename3 =
sprintf('/Users/amychang/Documents/Marshall
Lab/20170117_NewWTAlgorithms/Platel_Well%c%d/Platel_Well%c%d_Cell%d_Typ
e%doriginal.tif', alphabet(i), j, alphabet(i), j, u, category);
        imwrite(orig, filename3)
        askwhichFOVs = sprintf('Which FOVs need to be
stitched? ');
        whichFOVs = input(askwhichFOVs);
        askstitch = 0;
        while askstitch == 0
            for z = 1:length(whichFOVs)
                Cy5filename = strcat('path=[/Volumes/Fantom
HD/20141223/Amy_Chang/Amy_Chang_Chang1_2014.12.24.20.10.07/',
alphabet(i), '-', {' '}, num2str(j), '(fld ', {' '},
num2str(whichFOVs(z)), ' wv Cy5 - Cy5).tif]');
                FITCfilename =
strcat('path=[/Volumes/Fantom
HD/20141223/Amy_Chang/Amy_Chang_Chang1_2014.12.24.20.10.07/',
alphabet(i), '-', {' '}, num2str(j), '(fld ', {' '},
num2str(whichFOVs(z)), ' wv FITC - FITC).tif]');
                DAPIfilename =
strcat('path=[/Volumes/Fantom
HD/20141223/Amy_Chang/Amy_Chang_Chang1_2014.12.24.20.10.07/',
alphabet(i), '-', {' '}, num2str(j), '(fld ', {' '},
num2str(whichFOVs(z)), ' wv DAPI - DAPI).tif]');
                MIJ.run('Open...', Cy5filename)
                MIJ.run('Open...', FITCfilename)
                MIJ.run('Open...', DAPIfilename)
                MIJ.run('Merge Channels...', strcat('c1=[',
alphabet(i), '-', {' '}, num2str(j), '(fld ', {' '},
num2str(whichFOVs(z)), ' wv FITC - FITC).tif]', 'c2=[', alphabet(i),
-', {' '}, num2str(j), '(fld ', {' '}, num2str(whichFOVs(z)), ' wv Cy5
- Cy5).tif]', 'c3=[', alphabet(i), '-', {' '}, num2str(j), '(fld ', {'

```

```

'} , num2str(whichFOVs(z)), ' wv DAPI - DAPI).tif] create'));
    A = MIJ.getCurrentImage;
    A1 = uint16(A(:,:,1));
    A2 = uint16(A(:,:,2));
    A3 = uint16(A(:,:,3));
    filename2 =
sprintf('/Users/amychang/Documents/Marshall
Lab/20170117_NewWTAlgorithms/Platel_Well%%d/Platel_Well%%d_FOV%d.tif'
, alphabet(i), j, alphabet(i), j, whichFOVs(z));
    imwrite(cat(3,A1,A2,A3), filename2)
    MIJ.closeAllWindows
end
for z = 1:length(whichFOVs)
    filename2 =
sprintf('/Users/amychang/Documents/Marshall
Lab/20170117_NewWTAlgorithms/Platel_Well%%d/Platel_Well%%d_FOV%d.tif'
, alphabet(i), j, alphabet(i), j, whichFOVs(z));
    MIJ.run('Open...', strcat('path=[',
filename2, ']'))
    askchannels = sprintf('Channels set to
tubulin? ');
    if input(askchannels) == 1
        MIJ.run('Enhance Contrast',
'saturated=0.35');
    end
end
askready = sprintf('FOVs cropped and ready? ');
if input(askready) == 1
    MIJ.run('Pairwise stitching',
'fusion_method=[Linear Blending] check_peaks=100 compute_overlap
subpixel_accuracy x=0.0000 y=0.0000 registration_channel_image_1=[Only
channel 2] registration_channel_image_2=[Only channel 2]');
end
askchannels = sprintf('Channels set to tubulin?
');
if input(askchannels) == 1
    MIJ.run('Enhance Contrast',
'saturated=0.35');
end
askstitch = sprintf('Stitching looks ok? ');
askstitch = input(askstitch);
end
B = MIJ.getCurrentImage;
C = uint16(B);
composite = cat(3, C(:,:,1), C(:,:,2), C(:,:,3));
yesno = 0;
while yesno == 0
    figure, imshow(mat2gray(C(:,:,2)))
    h2 = imcontrast(gca)
    waitfor(h2)
    Cy5manual = getimage(gca);
    BW = edge(Cy5manual, 'sobel');
    se90 = strel('line', 6, 90);
    se0 = strel('line', 6, 0);
    BWdil = imdilate(BW, [se90, se0]);
    BWfill = imfill(BWdil, 'holes');
    seD = strel('diamond', 1);
    BWsmooth = imerode(BWfill, seD);

```

```

L = bwlabel(BWsmooth);
stats = regionprops(L, 'Area');
areas = cat(1, stats.Area);
BWsmooth_clean = BWsmooth;
for m = 1:length(stats);
    if stats(m).Area < 1000
        I = find(L==m);
        for q = 1:length(I);
            p = I(q);
            BWsmooth_clean(p) = 0;
        end
    end
end
BWoutline2 = bwperim(BWsmooth_clean);
outline_blue2 = C(:,:,3);
outline_blue2(BWoutline2) = 65535;
compositeoutlined = cat(3, C(:,:,1), C(:,:,2),
outline_blue2);
figure, imshow(imfuse(imadjust(C(:,:,2)),
imadjust(outline_blue2)))
askyesno = sprintf('Is the segmentation
acceptable? (0 = No, 1 = Yes) ');
yesno = input(askyesno);
end
celloutline = outline_blue2;
celloutline(outline_blue2 < 65535) = 0;
BWfill = imfill(celloutline);
Lfill = bwlabel(BWfill);
statsFill = regionprops(Lfill, 'Area', 'Centroid',
'BoundingBox');
area = cat(1, statsFill.Area);
maxPos = find(area == max(area));
rectangleDim = size(BWfill);
centroid = statsFill(maxPos).Centroid;
bbox = statsFill(maxPos).BoundingBox;
if floor(bbox(1,1)) < 11
    left_x = 1;
else
    left_x = floor(bbox(1,1)) - 10;
end
if floor(bbox(1,2)) < 11
    upper_y = 1;
else
    upper_y = floor(bbox(1,2)) - 10;
end
if ceil(bbox(1,1) + bbox(1,3)) + 10 >
(rectangleDim(2) - left_x)
    right_x = rectangleDim(2);
else
    right_x = ceil(bbox(1,1) + bbox(1,3)) + 10;
end
if ceil(bbox(1,2) + bbox(1,4)) + 10 >
(rectangleDim(1) - upper_y)
    lower_y = rectangleDim(1);
else
    lower_y = ceil(bbox(1,2) + bbox(1,4)) + 10;
end
compositeBoxed = cat(3, C(upper_y:lower_y,

```

```

left_x:right_x, 1), C(upper_y:lower_y, left_x:right_x, 2),
outline_blue2(upper_y:lower_y, left_x:right_x));
    filename4 = strcat(filename3(1:(length(filename)-
4)), 'Stitched_Type1.tif');
    imwrite(compositeBoxed, filename4)
    filename5 = strcat(filename(1:(length(filename)-
4)), 'Stitched_Type1original.tif');
    composite5 = cat(3, C(upper_y:lower_y,
left_x:right_x, 1), C(upper_y:lower_y, left_x:right_x, 2),
C(upper_y:lower_y, left_x:right_x, 3));
    imwrite(composite5, filename5)
    MIJ.closeAllWindows
    close
    end
    if category == 4;
        filename =
sprintf('/Users/amychang/Documents/Marshall
Lab/20170117_NewWTAlgorithms/Platel_Well%c%d/Platel_Well%c%d_Cell%d_Typ
e%d.tif', alphabet(i), j, alphabet(i), j, u, category);
        imwrite(origwith_outline, filename)
        filename3 =
sprintf('/Users/amychang/Documents/Marshall
Lab/20170117_NewWTAlgorithms/Platel_Well%c%d/Platel_Well%c%d_Cell%d_Typ
e%doriginal.tif', alphabet(i), j, alphabet(i), j, u, category);
        imwrite(orig, filename3)
        close
    end
    if category == 6;
        filename =
sprintf('/Users/amychang/Documents/Marshall
Lab/20170117_NewWTAlgorithms/Platel_Well%c%d/Platel_Well%c%d_Cell%d_Typ
e%d.tif', alphabet(i), j, alphabet(i), j, u, category);
        imwrite(origwith_outline, filename)
        filename3 =
sprintf('/Users/amychang/Documents/Marshall
Lab/20170117_NewWTAlgorithms/Platel_Well%c%d/Platel_Well%c%d_Cell%d_Typ
e%doriginal.tif', alphabet(i), j, alphabet(i), j, u, category);
        imwrite(orig, filename3)
        close
    end
end
end
end
end

% CATEGORIES
% 1 = properly segmented, ready for parameterization
% 2 = improperly segmented, needs manual segmentation
% 3 = needs stitching (found at borders of FOVs, overlap is incorrect)
% 4 = binucleate/overlapping cells, not analysable
% 5 = in contact with edge of well (not useful)
% 6 = trash / not analysable

```

Figure A2. Cell segmentation algorithm. Script written in MATLAB 2014b to segment cells based on a microtubule cytoskeleton stain.

```

% This is an algorithm to measure various size and shape parameters of
the
% input image. Useful primarily for nuclear and cellular analysis.
% Revised 03/02/2017 by Amy Chang (Marshall Lab, UCSF)

directory = cd;
D = dir(directory);
b = zeros(1, length(D));
for a = 1:length(D)
    b(a) = isempty(strfind(D(a).name, 'Type1.tif'));
end

measurements = struct([]);
counter = 0;
for i = 1:length(b)
    if b(i) == 0
        counter = counter + 1;
        measurements(counter).SegmentedFilename = D(i).name;
        temp = D(i).name;
        k = length(temp) - 4;
        temp = temp(1:k);
        measurements(counter).OriginalFilename = strcat(temp,
'original.tif');
        i = i + 1;
    elseif b(i) == 1
        i = i + 1;
    end
end

for m = 1:length(measurements)
    segmented = imread(measurements(m).SegmentedFilename);
    original = imread(measurements(m).OriginalFilename);
    segmentedBlue = segmented(:,:,3);
    originalBlue = original(:,:,3);
    allOutlines = segmentedBlue - originalBlue;
    originalGreen = original(:,:,2);
    measurements(m).CellImage = originalGreen;
    L = bwlabel(allOutlines);
    statsOutline = regionprops(L, 'Area', 'PixelIdxList');
    cellIndex = find([statsOutline.Area] == max([statsOutline.Area]));
    cellOutline = zeros(size(originalBlue));
    cellOutline(statsOutline(cellIndex).PixelIdxList) = 65535;
    figure, imshow(imfuse(imadjust(originalGreen), cellOutline))
    askyesno = sprintf('This is the cell outline. Enter 1 to
acknowledge. ');
    yesno = input(askyesno);
    if yesno == 1
        close all
    end
    measurements(m).CellOutline = cellOutline;
    measurements(m).CellOutlinePixels =
statsOutline(cellIndex).PixelIdxList;
    cellFilled = imfill(cellOutline);
    measurements(m).CellMask = cellFilled;
    L = bwlabel(cellFilled);
    stats = regionprops(L, 'Area', 'Centroid', 'ConvexArea',
'ConvexHull', ...
'ConvexImage', 'Eccentricity',

```

```

'EquivDiameter', ...
'MajorAxisLength', 'MinorAxisLength',
'Perimeter', ...
'PixelList', 'Solidity')
measurements(m).CellArea = stats.Area;
measurements(m).CellCentroid = stats.Centroid;
measurements(m).CellConvexArea = stats.ConvexArea;
measurements(m).CellConvexHull = stats.ConvexHull;
measurements(m).CellConvexImage = stats.ConvexImage;
measurements(m).CellEccentricity = stats.Eccentricity;
measurements(m).CellEquivDiameterArea = stats.EquivDiameter;
measurements(m).CellMajorAxisLength = stats.MajorAxisLength;
measurements(m).CellMinorAxisLength = stats.MinorAxisLength;
measurements(m).CellPerimeter = stats.Perimeter;
measurements(m).CellPixelList = stats.PixelList;
measurements(m).CellSolidity = stats.Solidity;
end

% Calculate parameters not included in the 'regionprops' function of
MATLAB.

% Calculate ConvexPerimeter, the perimeter of the convex hull.
for n = 1:length(measurements)
    A = measurements(n).CellConvexImage;
    L = bwlabel(A);
    convexLabel = regionprops(L, 'Perimeter');
    measurements(n).CellConvexPerimeter = convexLabel.Perimeter;
end

% Calculate EquivDiameterPerim, the diameter of an equivalent perimeter
circle
for p = 1:length(measurements)
    perimeter = measurements(p).CellPerimeter;      % perimeter of a
circle is pi*diameter
    diameter = perimeter / pi;
    measurements(p).CellEquivDiameterPerim = diameter;
end

% Calculate ratio between the major axis and minor axis lengths.
for q = 1:length(measurements)
    ratioMajorMinor = (measurements(q).CellMajorAxisLength) /
(measurements(q).CellMinorAxisLength);
    measurements(q).CellRatioMajorMinor = ratioMajorMinor;
end

% Calculate the area filled by the cell vs area of a circle w/ diameter
% equal to the major axis length (a rough measure of the "circularity"
of the object).
for r = 1:length(measurements)
    circleArea = (((measurements(r).CellMajorAxisLength) / 2)^2) * pi;
    measurements(r).CellCircularity = measurements(r).CellArea /
circleArea;
end

% Calculate pairwise distances between all perimeter pixels and the
cell
% centroid. Calculate MeanCentroidDist, MaxCentroidDist,
MinCentroidDist, CVCentroidDist, and VarCentroidDist.

```

```

for s = 1:length(measurements)
    [I J] = find(measurements(s).CellOutline > 0);           % convert
    perimeter pixels to Euclidean coordinates
    centroid = measurements(s).CellCentroid;                % cell centroid
    distances = pdist2([J I], centroid, 'Euclidean');
    measurements(s).CellMeanCentroidDist = mean(distances);
    measurements(s).CellMaxCentroidDist = max(distances);
    measurements(s).CellMinCentroidDist = min(distances);
    measurements(s).CellCVCentroidDist =
    (std(distances))/(mean(distances));
    measurements(s).CellVarCentroidDist = var(distances);
end

%smoothness/roughness measurements
for t = 1:length(measurements)
    A = measurements(t).CellOutline;
    H1 = fspecial('gaussian', [10 10], 2);
    A1 = imfilter(A, H1);
    A1Thinned = bwmorph(A1, 'thin', inf);
    A1Filled = imfill(A1Thinned, 'holes');
    SE1 = strel('disk', 1);
    A1Eroded = imerode(A1Filled, SE1);
    A1Dilated = imdilate(A1Eroded, SE1);
    L1 = bwlabel(A1Dilated);
    stats1 = regionprops(L1, 'Area', 'Perimeter', 'PixelIdxList');
    u = cat(1, stats1.Area);
    w = find(u == max(u));
    A1Cleaned = zeros(size(A));
    A1Cleaned(stats1(w).PixelIdxList) = 65535;
    figure
    subplot(1,2,1), imshow(A), title('original')
    subplot(1,2,2), imshow(A1Cleaned), title('low smooth')
    askyesno = sprintf('This is the low smoothed outline. Enter 1 to
accept. ');
    yesno = input(askyesno);
    if yesno == 1
        close all
    end
    measurements(t).CellLowSmoothMask = A1Cleaned;
    measurements(t).CellLowSmoothArea = stats1(w).Area;
    measurements(t).CellLowSmoothPerimeter = stats1(w).Perimeter;
    measurements(t).CellLowSmoothOrigAreaChange = (stats1(w).Area -
measurements(t).CellArea);
    measurements(t).CellLowSmoothOrigAreaChangeRel =
    (measurements(t).CellLowSmoothOrigAreaChange /
measurements(t).CellArea);
    measurements(t).CellLowSmoothOrigPerimeterChange =
    (stats1(w).Perimeter - measurements(t).CellPerimeter);
    measurements(t).CellLowSmoothOrigPerimeterChangeRel =
    (measurements(t).CellLowSmoothOrigPerimeterChange /
measurements(t).CellPerimeter);
    measurements(t).CellLowSmoothOrigAreaRatio = (stats1(w).Area /
measurements(t).CellArea);
    measurements(t).CellLowSmoothOrigPerimeterRatio =
    (stats1(w).Perimeter / measurements(t).CellPerimeter);
    H2 = fspecial('gaussian', [20 20], 2);
    A2 = imfilter(A, H2);
    A2Thinned = bwmorph(A2, 'thin', inf);

```

```

A2Filled = imfill(A2Thinned, 'holes');
SE2 = strel('disk', 1);
A2Eroded = imerode(A2Filled, SE2);
A2Dilated = imdilate(A2Eroded, SE2);
L2 = bwlabel(A2Dilated);
stats2 = regionprops(L2, 'Area', 'Perimeter', 'PixelIdxList');
x = cat(1, stats2.Area);
z = find(x == max(x));
A2Cleaned = zeros(size(A));
A2Cleaned(stats2(z).PixelIdxList) = 65535;
figure
subplot(1,2,1), imshow(A), title('original')
subplot(1,2,2), imshow(A2Cleaned), title('high smooth')
askyesno = sprintf('This is the high smoothed outline. Enter 1 to
accept. ');
yesno = input(askyesno);
if yesno == 1
    close all
end
measurements(t).CellHighSmoothMask = A2Cleaned;
measurements(t).CellHighSmoothArea = stats2(z).Area;
measurements(t).CellHighSmoothPerimeter = stats2(z).Perimeter;
measurements(t).CellHighSmoothOrigAreaChange = (stats2(z).Area -
measurements(t).CellArea);
measurements(t).CellHighSmoothOrigAreaChangeRel =
(measurements(t).CellHighSmoothOrigAreaChange /
measurements(t).CellArea);
measurements(t).CellHighSmoothOrigPerimeterChange =
(stats2(z).Perimeter - measurements(t).CellPerimeter);
measurements(t).CellHighSmoothOrigPerimeterChangeRel =
(measurements(t).CellHighSmoothOrigPerimeterChange /
measurements(t).CellPerimeter);
measurements(t).CellHighSmoothOrigAreaRatio = (stats2(z).Area /
measurements(t).CellArea);
measurements(t).CellHighSmoothOrigPerimeterRatio =
(stats2(z).Perimeter / measurements(t).CellPerimeter);
end

close all

save('WT_cellsizeShape.mat', 'measurements')

```

Figure A3. Cell morphometric feature extraction algorithm. Script written in MATLAB 2014b to extract morphometric features from microtubule cytoskeletal-based fluorescence.

```

% Algorithm to analyze textural/spatial distribution features of the
% cell/cytoskeleton.
% Revised 03/02/2017 by Amy Chang (Marshall Lab, UCSF)

load('WT_nucsize.shape.mat')

%Textural calculations (Haralick features).

for a = 1:length(measurements)
    CellImage = measurements(a).CellImage;
    CellMask = measurements(a).CellMask;
    CellImageNoBG = CellImage;
    CellImageNoBG(CellMask == 0) = 0;
    measurements(a).CellImageNoBG = CellImageNoBG;
    CellImageFull = CellImage;
    CellImageFull(CellMask == 0) = 65535; %set by
pixels to 65536 so they show up in (16, 16) of the GSCM; true low bin
interacting pixels are revealed in (1,1)
    K = unique(CellImageNoBG);
    minpixel = K(2);
    maxpixel = max(K);
    offsets = [0 1; -1 1;-1 0;-1 -1];
    glcmsFull = graycomatrix(CellImageFull, 'NumLevel', 16,
'GrayLimits', [minpixel maxpixel], 'Symmetric', true, 'Offset',
offsets);
    glcmsnoBG = graycomatrix(CellImageNoBG, 'NumLevel', 16,
'GrayLimits', [minpixel maxpixel], 'Symmetric', true, 'Offset',
offsets);
    glcmsTrue = glcmsnoBG;
    for b = 1:4
        glcmsTrue(1,1,b) = glcmsFull(1,1,b);
    end
    stats = graycoprops(glcmsTrue);
    measurements(a).CellContrast = stats.Contrast;
    measurements(a).CellMeanContrast = mean(stats.Contrast);
    measurements(a).CellMinContrast = min(stats.Contrast);
    measurements(a).CellMaxContrast = max(stats.Contrast);
    measurements(a).CellCVContrast = (std(stats.Contrast) /
mean(stats.Contrast));
    measurements(a).CellVarContrast = var(stats.Contrast);
    measurements(a).CellCorrelation = stats.Correlation;
    measurements(a).CellMeanCorrelation = mean(stats.Correlation);
    measurements(a).CellMinCorrelation = min(stats.Correlation);
    measurements(a).CellMaxCorrelation = max(stats.Correlation);
    measurements(a).CellCVCorrelation = (std(stats.Correlation) /
mean(stats.Correlation));
    measurements(a).CellVarCorrelation = var(stats.Correlation);
    measurements(a).CellEnergy = stats.Energy;
    measurements(a).CellMeanEnergy = mean(stats.Energy);
    measurements(a).CellMinEnergy = min(stats.Energy);
    measurements(a).CellMaxEnergy = max(stats.Energy);
    measurements(a).CellCVEnergy = (std(stats.Energy) /
mean(stats.Energy));
    measurements(a).CellVarEnergy = var(stats.Energy);
    measurements(a).CellHomogeneity = stats.Homogeneity;
    measurements(a).CellMeanHomogeneity = mean(stats.Homogeneity);
    measurements(a).CellMinHomogeneity = min(stats.Homogeneity);
    measurements(a).CellMaxHomogeneity = max(stats.Homogeneity);

```

```

    measurements(a).CellCVHomogeneity = (std(stats.Homogeneity) /
mean(stats.Homogeneity));
    measurements(a).CellVarHomogeneity = var(stats.Homogeneity);
end

%Radial distribution calculations.
for c = 1:length(measurements)
    NucCentroid = measurements(c).NucCentroid;
    [J, I] = ind2sub(size(measurements(c).CellImage),
measurements(c).CellOutlinePixels); %J is rows, I is columns (from top
left)
    D = pdist2(NucCentroid, [I J], 'euclidean'); %Euclidean
distances between nuclear centroid and all perimeter pixels
    maxD = max(D); %maximum
distance between nuclear centroid and perimeter
    [Y, X] = ind2sub(size(measurements(c).CellImage),
transpose(1:numel(measurements(c).CellImage)));
    Dall = pdist2(NucCentroid, [X Y], 'euclidean'); %distances
between nuclear centroid and ALL pixels in image rectangle
    Disc1Pos = find(Dall < maxD/4);
    disc1 = [];
    cellimage = measurements(c).CellImageNoBG;
    total = sum(sum(measurements(c).CellImageNoBG)); %sum of all
intensities within the cell (background set to 0)
    for d = 1:length(Disc1Pos)
        disc1 = [disc1 cellimage(Disc1Pos(d))];
    end
    measurements(c).CellFracTotalDisc1 = sum(disc1)/total;
    measurements(c).CellCVDisc1 = std(double(disc1)) / mean(disc1);
    measurements(c).CellVarDisc1 = var(double(disc1));
    Disc2Pos = find(Dall < maxD/2);
    disc2 = [];
    for d = 1:length(Disc2Pos)
        disc2 = [disc2 cellimage(Disc2Pos(d))];
    end
    measurements(c).CellFracTotalDisc2 = sum(disc2)/total;
    measurements(c).CellCVDisc2 = std(double(disc2)) / mean(disc2);
    measurements(c).CellVarDisc2 = var(double(disc2));
    Disc3Pos = find(Dall < maxD*3/4);
    disc3 = [];
    for d = 1:length(Disc3Pos)
        disc3 = [disc3 cellimage(Disc3Pos(d))];
    end
    measurements(c).CellFracTotalDisc3 = sum(disc3)/total;
    measurements(c).CellCVDisc3 = std(double(disc3)) / mean(disc3);
    measurements(c).CellVarDisc3 = var(double(disc3));
    Disc4Pos = find(Dall < maxD);
    disc4 = [];
    for d = 1:length(Disc4Pos)
        disc4 = [disc4 cellimage(Disc4Pos(d))];
    end
    measurements(c).CellFracTotalDisc4 = sum(disc4)/total;
    measurements(c).CellCVDisc4 = std(double(disc4)) / mean(disc4);
    measurements(c).CellVarDisc4 = var(double(disc4));
end

save('WT_celltexture.mat', 'measurements')

```

Figure A4. Cell textural feature extraction algorithm. Script written in MATLAB 2014b to extract textural features from microtubule cytoskeletal-based fluorescence.

```

% This is an algorithm to segment the nucleus and run shape/size
analyses.
% Revised 03/02/2017 by Amy Chang (Marshall Lab, UCSF)

load('WT_cellsize_shape.mat')

for a = 1:length(measurements)
    filename = measurements(a).OriginalFilename;
    composite = imread(filename);
    DAPI = composite(:,:,3);
    DAPIAdjusted = imadjust(DAPI);
    BW = edge(DAPIAdjusted, 'sobel');
    se90 = strel('line', 6, 90);
    se0 = strel('line', 6, 0);
    BWdilate = imdilate(BW, [se90, se0]);
    BWfill = imfill(BWdilate, 'holes');
    seD = strel('diamond', 1);
    BWsmooth = imerode(BWfill, seD);
    L = bwlabel(BWsmooth);
    stats = regionprops(L, 'Area', 'PixelIdxList');
    areas = cat(1, stats.Area);
    b = find(areas == max(areas));
    BWsmooth_clean = zeros(size(BWsmooth));
    BWsmooth_clean(stats(b).PixelIdxList) =
BWsmooth(stats(b).PixelIdxList);
    BWoutline = bwperim(BWsmooth_clean);
    figure
    subplot(1,2,1), imshow(imfuse(measurements(a).CellOutline,
DAPIAdjusted)), title('DAPI, contrast adjusted')
    subplot(1,2,2), imshow(imfuse(BWoutline, DAPIAdjusted)),
title('segmented')
    askyesno = sprintf('This is the nuclear segmentation. Enter 1 to
accept or 0 to reject. ');
    yesno = input(askyesno);
    while yesno == 0
        figure, imshow(mat2gray(DAPI));
        h2 = imcontrast(gca);
        waitfor(h2)
        DAPImanual = getimage(gca);
        BW = edge(DAPImanual, 'sobel');
        BWdilate = imdilate(BW, [se90, se0]);
        BWfill = imfill(BWdilate, 'holes');
        BWsmooth = imerode(BWfill, seD);
        L = bwlabel(BWsmooth);
        stats = regionprops(L, 'Area', 'PixelIdxList');
        areas = cat(1, stats.Area);
        c = find(areas == max(areas))
        BWsmooth_clean = zeros(size(BWsmooth));
        BWsmooth_clean(stats(c).PixelIdxList) =
BWsmooth(stats(c).PixelIdxList);
        BWoutline = bwperim(BWsmooth_clean);
        figure
        subplot(1,2,1), imshow(imfuse(measurements(a).CellOutline,
DAPIAdjusted)), title('DAPI, contrast adjusted')
        subplot(1,2,2), imshow(imfuse(BWoutline, DAPIAdjusted)),
title('segmented')
        askyesno = sprintf('Is the segmentation acceptable? (0 = No, 1
= Yes) ');

```

```

        yesno = input(askyesno);
    end
    measurements(a).NucImage = DAPI;
    nucOutline = zeros(size(DAPI));
    nucOutline(BWoutline) = 65535;
    measurements(a).NucOutline = nucOutline;
    LOutline = bwlabel(nucOutline);
    statsOutline = regionprops(LOutline, 'PixelIdxList');
    measurements(a).NucOutlinePixels = statsOutline.PixelIdxList;
    nucFilled = imfill(nucOutline);
    measurements(a).NucMask = nucFilled;
    figure, imshow(imfuse(measurements(a).CellOutline, DAPIAdjusted))
    nucnumber = input('How many nuclei are there? ');
    measurements(a).NucNumber = nucnumber;
    L_clean = bwlabel(BWsmooth_clean);
    stats_clean = regionprops(L_clean, 'Area', 'Centroid',
'ConvexArea', 'ConvexHull', ...
                                'ConvexImage', 'Eccentricity',
'EquivDiameter', ...
                                'MajorAxisLength',
'MinorAxisLength', 'Perimeter', ...
                                'PixelList', 'Solidity');
    measurements(a).NucArea = stats_clean.Area;
    measurements(a).NucMeanArea = (stats_clean.Area) / nucnumber;
    measurements(a).NucCellAreaRatio = stats_clean.Area /
measurements(a).CellArea;
    measurements(a).NucCentroid = stats_clean.Centroid;
    measurements(a).NucCellCentroidDist =
pdist2(measurements(a).NucCentroid, measurements(a).CellCentroid,
'Euclidean');
    measurements(a).NucConvexArea = stats_clean.ConvexArea;
    measurements(a).NucConvexHull = stats_clean.ConvexHull;
    measurements(a).NucConvexImage = stats_clean.ConvexImage;
    measurements(a).NucEccentricity = stats_clean.Eccentricity;
    measurements(a).NucEquivDiameterArea = stats_clean.EquivDiameter;
    measurements(a).NucMajorAxisLength = stats_clean.MajorAxisLength;
    measurements(a).NucMinorAxisLength = stats_clean.MinorAxisLength;
    measurements(a).NucPerimeter = stats_clean.Perimeter;
    measurements(a).NucMeanPerimeter = (stats_clean.Perimeter) /
nucnumber;
    measurements(a).NucCellPerimeterRatio = stats_clean.Perimeter /
measurements(a).CellPerimeter;
    measurements(a).NucPixelList = stats_clean.PixelList;
    measurements(a).NucSolidity = stats_clean.Solidity;
    close all
end

% Calculate parameters not included in the 'regionprops' function of
MATLAB.

% Calculate ConvexPerimeter, the perimeter of the convex hull.
for n = 1:length(measurements)
    A = measurements(n).NucConvexImage;
    L = bwlabel(A);
    convexLabel = regionprops(L, 'Perimeter');
    measurements(n).NucConvexPerimeter = convexLabel.Perimeter;
end

```

```

% Calculate EquivDiameterPerim, the diameter of an equivalent perimeter
circle
for p = 1:length(measurements)
    perimeter = measurements(p).NucPerimeter;      % perimeter of a
circle is pi*diameter
    diameter = perimeter / pi;
    measurements(p).NucEquivDiameterPerim = diameter;
end

% Calculate ratio between the major axis and minor axis lengths.
for q = 1:length(measurements)
    ratioMajorMinor = (measurements(q).NucMajorAxisLength) /
(measurements(q).NucMinorAxisLength);
    measurements(q).NucRatioMajorMinor = ratioMajorMinor;
end

% Calculate the area filled by the nucleus vs area of a circle w/
diameter
% equal to the major axis length (a rough measure of the "circularity"
of the object).
for r = 1:length(measurements)
    circleArea = ((measurements(r).NucMajorAxisLength) / 2)^2 * pi;
    measurements(r).NucCircularity = measurements(r).NucArea /
circleArea;
end

% Calculate pairwise distances between all perimeter pixels and the
nucleus
% centroid. Calculate MeanCentroidDist, MaxCentroidDist,
MinCentroidDist, CVCentroidDist, and VarCentroidDist.
for s = 1:length(measurements)
    [I J] = find(measurements(s).NucOutline > 0);      % convert
perimeter pixels to Euclidean coordinates
    centroid = measurements(s).NucCentroid;           % cell centroid
    distances = pdist2([J I], centroid, 'Euclidean');
    measurements(s).NucMeanCentroidDist = mean(distances);
    measurements(s).NucMaxCentroidDist = max(distances);
    measurements(s).NucMinCentroidDist = min(distances);
    measurements(s).NucCVCentroidDist =
(std(distances))/(mean(distances));
    measurements(s).NucVarCentroidDist = var(distances);
end

%smoothness/roughness measurements
for t = 1:length(measurements)
    A = measurements(t).NucOutline;
    H1 = fspecial('gaussian', [5 5], 2);
    A1 = imfilter(A, H1);
    A1Thinned = bwmorph(A1, 'thin', inf);
    A1Filled = imfill(A1Thinned, 'holes');
    SE1 = strel('disk', 1);
    A1Eroded = imerode(A1Filled, SE1);
    A1Dilated = imdilate(A1Eroded, SE1);
    L1 = bwlabel(A1Dilated);
    stats1 = regionprops(L1, 'Area', 'Perimeter', 'PixelIdxList');
    u = cat(1, stats1.Area);
    w = find(u == max(u));

```

```

A1Cleaned = zeros(size(A));
A1Cleaned(stats1(w).PixelIdxList) = 65535;
figure
subplot(1,2,1), imshow(A), title('original')
subplot(1,2,2), imshow(A1Cleaned), title('low smooth')
askyesno = sprintf('This is the low smoothed outline. Enter 1 to
accept. ');
yesno = input(askyesno);
if yesno == 1
    close all
end
measurements(t).NucLowSmoothMask = A1Cleaned;
measurements(t).NucLowSmoothArea = stats1(w).Area;
measurements(t).NucLowSmoothPerimeter = stats1(w).Perimeter;
measurements(t).NucLowSmoothOrigAreaChange = (stats1(w).Area -
measurements(t).NucArea);
measurements(t).NucLowSmoothOrigAreaChangeRel =
(measurements(t).NucLowSmoothOrigAreaChange / measurements(t).NucArea);
measurements(t).NucLowSmoothOrigPerimeterChange =
(stats1(w).Perimeter - measurements(t).NucPerimeter);
measurements(t).NucLowSmoothOrigPerimeterChangeRel =
(measurements(t).NucLowSmoothOrigPerimeterChange /
measurements(t).NucPerimeter);
measurements(t).NucLowSmoothOrigAreaRatio = (stats1(w).Area /
measurements(t).NucArea);
measurements(t).NucLowSmoothOrigPerimeterRatio =
(stats1(w).Perimeter / measurements(t).NucPerimeter);
H2 = fspecial('gaussian', [10 10], 2);
A2 = imfilter(A, H2);
A2Thinned = bwmorph(A2, 'thin', inf);
A2Filled = imfill(A2Thinned, 'holes');
SE2 = strel('disk', 1);
A2Eroded = imerode(A2Filled, SE2);
A2Dilated = imdilate(A2Eroded, SE2);
L2 = bwlabel(A2Dilated);
stats2 = regionprops(L2, 'Area', 'Perimeter', 'PixelIdxList');
x = cat(1, stats2.Area);
z = find(x == max(x));
A2Cleaned = zeros(size(A));
A2Cleaned(stats2(z).PixelIdxList) = 65535;
figure
subplot(1,2,1), imshow(A), title('original')
subplot(1,2,2), imshow(A2Cleaned), title('high smooth')
askyesno = sprintf('This is the high smoothed outline. Enter 1 to
accept. ');
yesno = input(askyesno);
if yesno == 1
    close all
end
measurements(t).NucHighSmoothMask = A2Cleaned;
measurements(t).NucHighSmoothArea = stats2(z).Area;
measurements(t).NucHighSmoothPerimeter = stats2(z).Perimeter;
measurements(t).NucHighSmoothOrigAreaChange = (stats2(z).Area -
measurements(t).NucArea);
measurements(t).NucHighSmoothOrigAreaChangeRel =
(measurements(t).NucHighSmoothOrigAreaChange /
measurements(t).NucArea);
measurements(t).NucHighSmoothOrigPerimeterChange =

```

```
(stats2(z).Perimeter - measurements(t).NucPerimeter);
    measurements(t).NucHighSmoothOrigPerimeterChangeRel =
(measurements(t).NucHighSmoothOrigPerimeterChange /
measurements(t).NucPerimeter);
    measurements(t).NucHighSmoothOrigAreaRatio = (stats2(z).Area /
measurements(t).NucArea);
    measurements(t).NucHighSmoothOrigPerimeterRatio =
(stats2(z).Perimeter / measurements(t).NucPerimeter);
end
save('WT_nucsizehape.mat', 'measurements')
```

Figure A5. Nucleus morphometric feature extraction algorithm. Script written in MATLAB 2014b to extract morphometric features from nucleus-based fluorescence.

```

% Algorithm to analyze textural/spatial distribution features of the
% nucleus.
% Revised 03/02/2017 by Amy Chang (Marshall Lab, UCSF)

```

```

load('WT_celltexture.mat')

```

```

%Textural calculations (Haralick features).

```

```

for a = 1:length(measurements)
    NucImage = measurements(a).NucImage;
    NucMask = measurements(a).NucMask;
    NucImageNoBG = NucImage;
    NucImageNoBG(NucMask == 0) = 0;
    measurements(a).NucImageNoBG = NucImageNoBG;
    NucImageFull = NucImage;
    NucImageFull(NucMask == 0) = 65535; %set by
pixels to 65536 so they show up in (16, 16) of the GSCM; true low bin
interacting pixels are revealed in (1,1)
    K = unique(NucImageNoBG);
    minpixel = K(2);
    maxpixel = max(K);
    offsets = [0 1; -1 1;-1 0;-1 -1];
    glcmsFull = graycomatrix(NucImageFull, 'NumLevel', 16,
'GrayLimits', [minpixel maxpixel], 'Symmetric', true, 'Offset',
offsets);
    glcmsnoBG = graycomatrix(NucImageNoBG, 'NumLevel', 16,
'GrayLimits', [minpixel maxpixel], 'Symmetric', true, 'Offset',
offsets);
    glcmsTrue = glcmsnoBG;
    for b = 1:4
        glcmsTrue(1,1,b) = glcmsFull(1,1,b);
    end
    stats = graycoprops(glcmsTrue);
    measurements(a).NucContrast = stats.Contrast;
    measurements(a).NucMeanContrast = mean(stats.Contrast);
    measurements(a).NucMinContrast = min(stats.Contrast);
    measurements(a).NucMaxContrast = max(stats.Contrast);
    measurements(a).NucCVContrast = (std(stats.Contrast) /
mean(stats.Contrast));
    measurements(a).NucVarContrast = var(stats.Contrast);
    measurements(a).NucCorrelation = stats.Correlation;
    measurements(a).NucMeanCorrelation = mean(stats.Correlation);
    measurements(a).NucMinCorrelation = min(stats.Correlation);
    measurements(a).NucMaxCorrelation = max(stats.Correlation);
    measurements(a).NucCVCorrelation = (std(stats.Correlation) /
mean(stats.Correlation));
    measurements(a).NucVarCorrelation = var(stats.Correlation);
    measurements(a).NucEnergy = stats.Energy;
    measurements(a).NucMeanEnergy = mean(stats.Energy);
    measurements(a).NucMinEnergy = min(stats.Energy);
    measurements(a).NucMaxEnergy = max(stats.Energy);
    measurements(a).NucCVEnergy = (std(stats.Energy) /
mean(stats.Energy));
    measurements(a).NucVarEnergy = var(stats.Energy);
    measurements(a).NucHomogeneity = stats.Homogeneity;
    measurements(a).NucMeanHomogeneity = mean(stats.Homogeneity);
    measurements(a).NucMinHomogeneity = min(stats.Homogeneity);
    measurements(a).NucMaxHomogeneity = max(stats.Homogeneity);

```

```

    measurements(a).NucCVHomogeneity = (std(stats.Homogeneity) /
mean(stats.Homogeneity));
    measurements(a).NucVarHomogeneity = var(stats.Homogeneity);
end

%Radial distribution calculations.
for c = 1:length(measurements)
    NucCentroid = measurements(c).NucCentroid;
    [J, I] = ind2sub(size(measurements(c).CellImage),
measurements(c).NucOutlinePixels); %J is rows, I is columns (from top
left)
    D = pdist2(NucCentroid, [I J], 'euclidean'); %Euclidean
distances between nuclear centroid and all perimeter pixels
    maxD = max(D); %maximum
distance between nuclear centroid and perimeter
    [Y, X] = ind2sub(size(measurements(c).CellImage),
transpose(1:numel(measurements(c).CellImage)));
    Dall = pdist2(NucCentroid, [X Y], 'euclidean'); %distances
between nuclear centroid and ALL pixels in image rectangle
    Disc1Pos = find(Dall < maxD/4);
    disc1 = [];
    nucimage = measurements(c).NucImageNoBG;
    total = sum(sum(measurements(c).NucImageNoBG)); %sum of all
intensities within the nucleus (cell and background set to 0)
    for d = 1:length(Disc1Pos)
        disc1 = [disc1 nucimage(Disc1Pos(d))];
    end
    measurements(c).NucFracTotalDisc1 = sum(disc1)/total;
    measurements(c).NucCVDisc1 = std(double(disc1)) / mean(disc1);
    measurements(c).NucVarDisc1 = var(double(disc1));
    Disc2Pos = find(Dall < maxD/2);
    disc2 = [];
    for d = 1:length(Disc2Pos)
        disc2 = [disc2 nucimage(Disc2Pos(d))];
    end
    measurements(c).NucFracTotalDisc2 = sum(disc2)/total;
    measurements(c).NucCVDisc2 = std(double(disc2)) / mean(disc2);
    measurements(c).NucVarDisc2 = var(double(disc2));
    Disc3Pos = find(Dall < maxD*3/4);
    disc3 = [];
    for d = 1:length(Disc3Pos)
        disc3 = [disc3 nucimage(Disc3Pos(d))];
    end
    measurements(c).NucFracTotalDisc3 = sum(disc3)/total;
    measurements(c).NucCVDisc3 = std(double(disc3)) / mean(disc3);
    measurements(c).NucVarDisc3 = var(double(disc3));
    Disc4Pos = find(Dall < maxD);
    disc4 = [];
    for d = 1:length(Disc4Pos)
        disc4 = [disc4 nucimage(Disc4Pos(d))];
    end
    measurements(c).NucFracTotalDisc4 = sum(disc4)/total;
    measurements(c).NucCVDisc4 = std(double(disc4)) / mean(disc4);
    measurements(c).NucVarDisc4 = var(double(disc4));
end

save('WT_nuctexture.mat', 'measurements')

```

Figure A6. Nucleus textural feature extraction algorithm. Script written in MATLAB 2014b to extract textural features from nucleus-based fluorescence.

```

% This algorithm calculates mitochondrial morphology parameters
including
% network parameters and texture/spatial distribution measurements.
% Revised 03/02/2017 by Amy Chang (Marshall Lab, UCSF)

load('WT_nuctexture.mat')

for a = 1:length(measurements)
    segmented = imread(measurements(a).SegmentedFilename);
    FITC = segmented(:,:,1);
    cellmask = measurements(a).CellMask;
    FITCnoBG = FITC;
    FITCnoBG(cellmask == 0) = 0;
    thresh = isodata(imadjust(FITCnoBG));
    BW = im2bw(imadjust(FITCnoBG), thresh);
    figure
    subplot(1,2,1), imshow(imadjust(FITCnoBG)), title('original FITC,
adjusted')
    subplot(1,2,2), imshow(BW), title('thresholded with automatic
threshold')
    askyesno = sprintf('This is the mitochondria segmentation. Enter 1
to accept or 0 to reject. ');
    yesno = input(askyesno);
    while yesno == 0
        figure, imshow(mat2gray(FITCnoBG));
        h2 = imcontrast(gca);
        waitfor(h2)
        FITCmanual = getimage(gca);
        threshManual = isodata(imadjust(FITCmanual));
        BW = im2bw(imadjust(FITCmanual), threshManual);
        figure, imshow(BW)
        askyesno = sprintf('Is the segmentation acceptable? (0 = No, 1
= Yes) ');
        yesno = input(askyesno);
    end
    close all
    L = bwlabel(BW);
    stats = regionprops(L, 'Area', 'Centroid', 'Perimeter',
'PixelIdxList');
    areas = cat(1, stats.Area);
    perimeters = cat(1, stats.Perimeter);
    centroids = [];
    for b = 1:length(stats)
        centroids = [centroids; stats(b).Centroid];
    end
    measurements(a).MitoImage = FITC;
    measurements(a).MitoImageNoBG = FITCnoBG;
    measurements(a).MitoMask = BW;
    measurements(a).MitoPixels = cat(1, stats.PixelIdxList);
    measurements(a).MitoNumber = length(stats);
    measurements(a).MitoSumArea = sum(areas);
    measurements(a).MitoMeanArea = mean(areas);
    measurements(a).MitoMedianArea = median(areas);
    measurements(a).MitoMaxArea = max(areas);
    measurements(a).MitoMinArea = min(areas);
    measurements(a).MitoCVArea = std(areas) / mean(areas);
    measurements(a).MitoVarArea = var(areas);
    measurements(a).MitoCellAreaRatio = sum(areas) /

```

```

measurements(a).CellArea;
    measurements(a).MitoSumPerimeter = sum(perimeters);
    measurements(a).MitoMeanPerimeter = mean(perimeters);
    measurements(a).MitoMedianPerimeter = median(perimeters);
    measurements(a).MitoMaxPerimeter = max(perimeters);
    measurements(a).MitoMinPerimeter = min(perimeters);
    measurements(a).MitoCVPerimeter = std(perimeters) /
mean(perimeters);
    measurements(a).MitoVarPerimeter = var(perimeters);
    measurements(a).MitoCellPerimeterRatio = sum(perimeters) /
measurements(a).CellPerimeter;
    weightedcentroids = [];
    for c = 1:length(stats)
        weightedcentroids = [weightedcentroids;
stats(c).Centroid*stats(c).Area];
    end
    measurements(a).MitoCentroid = sum(weightedcentroids)/sum(areas);
    measurements(a).MitoCellCentroidDist =
pdist2(measurements(a).MitoCentroid, measurements(a).CellCentroid,
'Euclidean');
    measurements(a).MitoNucCentroidDist =
pdist2(measurements(a).MitoCentroid, measurements(a).NucCentroid,
'Euclidean');
    skeleton = bwmorph(BW, 'skel', Inf);
    figure
    subplot(1,2,1), imshow(BW), title('segmented mitochondria')
    subplot(1,2,2), imshow(skeleton), title('skeletonized')
    statsskel = regionprops(skeleton, 'Area', 'PixelIdxList');
    skelareas = cat(1, statsskel.Area);
    sumskel = sum(skelareas);
    measurements(a).MitoObjSkelRatio = measurements(a).MitoSumArea /
sumskel;
    branchpoints = bwmorph(skeleton, 'branchpoints');
    endpoints = bwmorph(skeleton, 'endpoints');
    measurements(a).MitoNumBranchpoints = sum(sum(branchpoints));
    measurements(a).MitoNumEndpoints = sum(sum(endpoints));
    diff = skeleton - branchpoints;
    mitoFused = zeros(size(FITC));
    mitoFragmented = zeros(size(FITC));
    IdxBranchpoints = find(branchpoints == 1);
    for d = 1:length(stats)
        if isempty(intersect(stats(d).PixelIdxList, IdxBranchpoints))
== 0        %if not empty, there is an intersection, and it is a fused
object
            mitoFused(stats(d).PixelIdxList) = 1;
        elseif isempty(intersect(stats(d).PixelIdxList,
IdxBranchpoints)) == 1
            mitoFragmented(stats(d).PixelIdxList) = 1;
        end
    end
    figure
    subplot(1,2,1), imshow(mitoFused), title('fused mitochondria');
    subplot(1,2,2), imshow(mitoFragmented), title('fragmented
mitochondria');
    measurements(a).MitoFusedMask = mitoFused;
    measurements(a).MitoFragmentedMask = mitoFragmented;
    measurements(a).MitoMaskFull = mitoFused + mitoFragmented;
    LFused = bwlabel(mitoFused);

```

```

statsFused = regionprops(LFused, 'Area');
areasFused = cat(1, statsFused.Area);
totalArea = sum(sum(measurements(a).MitoMaskFull));
measurements(a).MitoNumberFused = length(statsFused);
measurements(a).MitoMeanFusedArea = mean(areasFused);
measurements(a).MitoMaxFusedArea = max(areasFused);
measurements(a).MitoMinFusedArea = min(areasFused);
measurements(a).MitoCVFusedArea = std(areasFused) /
mean(areasFused);
measurements(a).MitoVarFusedArea = var(areasFused);
measurements(a).MitoPercentFusedTotalArea = sum(areasFused) /
totalArea;
LFragmented = bwlabel(mitoFragmented);
statsFragmented = regionprops(LFragmented, 'Area');
areasFragmented = cat(1, statsFragmented.Area);
measurements(a).MitoNumberFragmented = length(statsFragmented);
measurements(a).MitoMeanFragmentedArea = mean(areasFragmented);
measurements(a).MitoMaxFragmentedArea = max(areasFragmented);
measurements(a).MitoMinFragmentedArea = min(areasFragmented);
measurements(a).MitoCVFragmentedArea = std(areasFragmented) /
mean(areasFragmented);
measurements(a).MitoVarFragmentedArea = var(areasFragmented);
measurements(a).MitoRatioFusedFragmented = sum(areasFused) /
sum(areasFragmented);
measurements(a).MitoPercentFragmentedTotalArea =
sum(areasFragmented) / totalArea;
close all
end

for e = 1:length(measurements)
    cellmask = measurements(e).CellMask;
    mitoImageNoBG = measurements(e).MitoImageNoBG;
    mitoImageFull = mitoImageNoBG;
    mitoImageFull(cellmask == 0) = 65535; %set bg pixels
to 65536 so they show up in (16, 16) of the GSCM; true low bin
interacting pixels are revealed in (1,1)
    K = unique(mitoImageNoBG);
    minpixel = K(2);
    maxpixel = max(K);
    offsets = [0 1; -1 1;-1 0;-1 -1];
    glcmsFull = graycomatrix(mitoImageFull, 'NumLevel', 16,
'GrayLimits', [minpixel maxpixel], 'Symmetric', true, 'Offset',
offsets);
    glcmsnoBG = graycomatrix(mitoImageNoBG, 'NumLevel', 16,
'GrayLimits', [minpixel maxpixel], 'Symmetric', true, 'Offset',
offsets);
    glcmsTrue = glcmsnoBG;
    for b = 1:4
        glcmsTrue(1,1,b) = glcmsFull(1,1,b);
    end
    stats = graycoprops(glcmsTrue);
    measurements(e).MitoContrast = stats.Contrast;
    measurements(e).MitoMeanContrast = mean(stats.Contrast);
    measurements(e).MitoMinContrast = min(stats.Contrast);
    measurements(e).MitoMaxContrast = max(stats.Contrast);
    measurements(e).MitoCVContrast = (std(stats.Contrast) /
mean(stats.Contrast));
    measurements(e).MitoVarContrast = var(stats.Contrast);

```

```

    measurements(e).MitoCorrelation = stats.Correlation;
    measurements(e).MitoMeanCorrelation = mean(stats.Correlation);
    measurements(e).MitoMinCorrelation = min(stats.Correlation);
    measurements(e).MitoMaxCorrelation = max(stats.Correlation);
    measurements(e).MitoCVCorrelation = (std(stats.Correlation) /
mean(stats.Correlation));
    measurements(e).MitoVarCorrelation = var(stats.Correlation);
    measurements(e).MitoEnergy = stats.Energy;
    measurements(e).MitoMeanEnergy = mean(stats.Energy);
    measurements(e).MitoMinEnergy = min(stats.Energy);
    measurements(e).MitoMaxEnergy = max(stats.Energy);
    measurements(e).MitoCVEnergy = (std(stats.Energy) /
mean(stats.Energy));
    measurements(e).MitoVarEnergy = var(stats.Energy);
    measurements(e).MitoHomogeneity = stats.Homogeneity;
    measurements(e).MitoMeanHomogeneity = mean(stats.Homogeneity);
    measurements(e).MitoMinHomogeneity = min(stats.Homogeneity);
    measurements(e).MitoMaxHomogeneity = max(stats.Homogeneity);
    measurements(e).MitoCVHomogeneity = (std(stats.Homogeneity) /
mean(stats.Homogeneity));
    measurements(e).MitoVarHomogeneity = var(stats.Homogeneity);
end

for f = 1:length(measurements)
    NucCentroid = measurements(f).NucCentroid;
    [J, I] = ind2sub(size(measurements(f).CellImage),
measurements(f).MitoPixels); %J is rows, I is columns (from top left)
    D = pdist2(NucCentroid, [I J], 'euclidean'); %Euclidean
    distances between nuclear centroid and all mitochondria pixels
    maxD = max(D); %maximum
    distance between nuclear centroid and any mitochondrial object
    [Y, X] = ind2sub(size(measurements(f).CellImage),
transpose(1:numel(measurements(f).CellImage)));
    Dall = pdist2(NucCentroid, [X Y], 'euclidean'); %distances
    between nuclear centroid and ALL pixels in image rectangle
    Disc1Pos = find(Dall < maxD/4);
    disc1 = [];
    mitoimage = measurements(f).MitoImageNoBG;
    mitoimage(measurements(f).MitoMask == 0) = 0;
    total = sum(sum(mitoimage)); %sum of all intensities within the
nucleus (background set to 0)
    for d = 1:length(Disc1Pos)
        disc1 = [disc1 mitoimage(Disc1Pos(d))];
    end
    measurements(f).MitoFracTotalDisc1 = sum(disc1)/total;
    measurements(f).MitoCVDisc1 = std(double(disc1)) / mean(disc1);
    measurements(f).MitoVarDisc1 = var(double(disc1));
    Disc2Pos = find(Dall < maxD/2);
    disc2 = [];
    for d = 1:length(Disc2Pos)
        disc2 = [disc2 mitoimage(Disc2Pos(d))];
    end
    measurements(f).MitoFracTotalDisc2 = sum(disc2)/total;
    measurements(f).MitoCVDisc2 = std(double(disc2)) / mean(disc2);
    measurements(f).MitoVarDisc2 = var(double(disc2));
end

```

```

Disc3Pos = find(Dall < maxD*3/4);
disc3 = [];
for d = 1:length(Disc3Pos)
    disc3 = [disc3 mitoimage(Disc3Pos(d))];
end
measurements(f).MitoFracTotalDisc3 = sum(disc3)/total;
measurements(f).MitoCVDisc3 = std(double(disc3)) / mean(disc3);
measurements(f).MitoVarDisc3 = var(double(disc3));
Disc4Pos = find(Dall < maxD);
disc4 = [];
for d = 1:length(Disc4Pos)
    disc4 = [disc4 mitoimage(Disc4Pos(d))];
end
measurements(f).MitoFracTotalDisc4 = sum(disc4)/total;
measurements(f).MitoCVDisc4 = std(double(disc4)) / mean(disc4);
measurements(f).MitoVarDisc4 = var(double(disc4));
end

filename = measurements(f).SegmentedFilename
filesave = strcat('WT_', filename(8:13), '_ALLMEASUREMENTS.mat')
save(filesave, 'measurements')

```

```

function level=isodata(I)
% ISODATA Compute global image threshold using iterative isodata
method.
% LEVEL = ISODATA(I) computes a global threshold (LEVEL) that can be
% used to convert an intensity image to a binary image with IM2BW.
LEVEL
% is a normalized intensity value that lies in the range [0, 1].
% This iterative technique for choosing a threshold was developed by
Ridler and Calvard .
% The histogram is initially segmented into two parts using a
starting threshold value such as  $0 = 2B-1$ ,
% half the maximum dynamic range.
% The sample mean (mf,0) of the gray values associated with the
foreground pixels and the sample mean (mb,0)
% of the gray values associated with the background pixels are
computed. A new threshold value 1 is now computed
% as the average of these two sample means. The process is repeated,
based upon the new threshold,
% until the threshold value does not change any more.

%
% Class Support
% -----
% The input image I can be of class uint8, uint16, or double and it
% must be nonsparse. LEVEL is a double scalar.
%
% Example
% -----
%     I = imread('blood1.tif');
%     level = graythresh(I);
%     BW = im2bw(I,level);
%     imshow(BW)
%
% See also IM2BW.
%
% Reference :T.W. Ridler, S. Calvard, Picture thresholding using an
iterative selection method,
%     IEEE Trans. System, Man and Cybernetics, SMC-8 (1978) 630-
632.

% Convert all N-D arrays into a single column. Convert to uint8 for
% fastest histogram computation.
I = im2uint8(I(:));

% STEP 1: Compute mean intensity of image from histogram, set T=mean(I)
[counts,N]=imhist(I);
i=1;
mu=cumsum(counts);
T(i)=(sum(N.*counts))/mu(end);
T(i)=round(T(i));

% STEP 2: compute Mean above T (MAT) and Mean below T (MBT) using T
from
% step 1
mu2=cumsum(counts(1:T(i)));
MBT=sum(N(1:T(i)).*counts(1:T(i)))/mu2(end);

```

```

mu3=cumsum(counts(T(i):end));
MAT=sum(N(T(i):end).*counts(T(i):end))/mu3(end);
i=i+1;
% new T = (MAT+MBT)/2
T(i)=round((MAT+MBT)/2);

% STEP 3 to n: repeat step 2 if T(i)~=T(i-1)
while abs(T(i)-T(i-1))>=1
    mu2=cumsum(counts(1:T(i)));
    MBT=sum(N(1:T(i)).*counts(1:T(i)))/mu2(end);

    mu3=cumsum(counts(T(i):end));
    MAT=sum(N(T(i):end).*counts(T(i):end))/mu3(end);

    i=i+1;
    T(i)=round((MAT+MBT)/2);
    Threshold=T(i);
end

% Normalize the threshold to the range [i, 1].
level = (Threshold - 1) / (N(end) - 1);

```

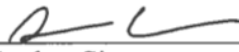
Figure A7. Mitochondria morphometric and textural feature extraction algorithm. Script written in MATLAB 2014b to extract morphometric and textural features from mitochondria-based fluorescence.

Publishing Agreement

It is the policy of the University to encourage the distribution of all theses, dissertations, and manuscripts. Copies of all UCSF theses, dissertations, and manuscripts will be routed to the library via the Graduate Division. The library will make all theses, dissertations, and manuscripts accessible to the public and will preserve these to the best of their abilities, in perpetuity.

Please sign the following statement:

I hereby grant permission to the Graduate Division of the University of California, San Francisco to release copies of my thesis, dissertation, or manuscript to the Campus Library to provide access and preservation, in whole or in part, in perpetuity.



Author Signature

12/27/2017
Date